LONDON'S GLOBAL UNIVERSITY

Bimolecular recombination in Non-Langevin ZZ115 based blend systems for Organic Photovoltaics

By Thibaut Charles Wohrer

Supervised by Dr. Tracey Clarke, Dr. Giorgio Volpe, Dr. Michael Sullivan and Dr Ye Jun

University of College London
Department of Chemistry

This thesis is submitted to University College London for the degree of Doctor of Philosophy

August 2022

Declaration

I, Thibaut Wohrer confirm that the work presented in this thesis is my own. Where information has been derived from other sources, I confirm that this has been indicated in the thesis

Abstract

Organic solar cells are currently positioned as a renewable energy source, potentially solving issues with current solar cells in application, cost and production. However, organic solar cells suffer from low efficiencies compared to their traditional counterparts. Bimolecular recombination of charge carriers before collection serves as a major loss process in organic solar cells and is a significant contributor to these low efficiencies. In this work, potential factors influencing this bimolecular recombination process in a conjugated polymer (ZZ115) blended with fullerenes were studied, where these ZZ115/fullerene blends show a suppressed, non-Langevin behaviour. This study was done via the combination of an experimental section using UV-VIS spectroscopy, photoluminescence spectroscopy and Transient Absorption Spectroscopy, and a computational section using Density Functional Theory and the VOTCA software for large system modelling. Overall results found a polaron feature in ZZ115 pristine and two polaron features in ZZ115 blends. These features were identified as a ZZ115 polaron in a ZZ115 crystalline medium in both pristine and blend, and a ZZ115 polaron in a mixed amorphous region unique to the blend. Blend ratio variation shows no influence of fullerene concentration on the mixed amorphous polaron feature past 10% concentration while a gradual decrease in the recombination kinetics is observed for the crystalline polaron feature. The latter is attributed to the addition of fullerene disrupting the crystalline ordered phase leading to deeper trap states slowing down charge recombination. Computational calculations have highlighted the lack of unusual molecular properties for ZZ115, but large-scale computational studies are still a work in progress to corroborate experimental findings. Nevertheless, important insights into the morphological and electronic impact on bimolecular recombination in ZZ115 were achieved in this study, providing both device optimisation guidelines and a better understanding of the bimolecular recombination process.

Impact Statement

The advent of climate change has highlighted the limitations of relying on fossil fuel technologies as the primary means of generating electricity. Solar energy is a promising energy source with the capacity to fulfil the energy needs of the entire world, using an area the size of Spain. Organic solar cells stand out as an alternative to the current traditional silicon based solar cells thanks to their flexibility and ease of processing. These advantages would allow, large-scale low-cost production, solving one of the major issues with current inorganic solar cells. Unfortunately, organic solar cells lag behind their inorganic counterparts in terms of device efficiency and stability, hampering their competitivity as a renewable energy source.

A critical component to the reduced device efficiency of organic solar cells lies in the loss processes occurring due to the use of organic materials such as bimolecular recombination, the recombination of charges generated from different molecules in the material. Bimolecular recombination has been a major source of losses but certain material systems such ZZ115:$PC_{60}BM$ have shown a reduced bimolecular recombination compared to established models. A combination of transient absorption spectroscopy and density functional theory was used to provide insight into the possible origin of this reduced bimolecular recombination behaviour.

The results of this thesis provide additional insight into the inner working of an usual polymer in ZZ115, possible guidelines for device morphology optimisation, and methodological outlines for a comprehensive study relating experimental observations with computational simulations. Thus, these findings should provide groundwork for future studies be it experimental or computation with the overall aim to further understanding onto the bimolecular process and therefore OPV device efficiencies.

Table of Contents

List of Figures

List of Tables

Glossary of acronyms

Molecules

ZZ115: short name for poly((4,4 - bis(2 - ethylhexyl) dithieno (3,2 - b:2′ ,3′ - d) silole) - 2,6 - diyl - alt - (2,5 - bis 3 - tetradecylthiophen - 2 - yl thiazolo 5,4 - d thiazole) - 2,5diyl), also known as PDTSiTTz and KP115

P3HT: short name for poly(3-hexylthiophene-2,5-diyl)

$PC_{60}BM$: short name for [6,6]-Phenyl-C61-butyric acid methyl ester

$PC_{70}BM$: short name for [6,6]-Phenyl-C71-butyric acid methyl ester

Si-PCPDTBT: short name for Poly[(4,4 - bis(2 - ethylhexyl) - dithieno[3,2 - b:2′ ,3′ - d]silole) - 2,6 - diyl - alt - (2,1,3 - benzothiadiazole) - 4,7 - diyl], also known as PSBTBT

PCPDTTTz: short name for poly[2,6-(4,4-bis-(2-ethylhexyl)-4H-cyclopenta[2,1-b;3,4-b′]-dithiophene)-alt-4,7-(2,1,3-benzothiadiazole)], the carbon analogue to ZZ115

P(NDI2OD-T2): short name for Poly{[N,N'-bis(2-octyldodecyl)naphthalene-1,4,5,8-bis(dicarboximide)-2,6-diyl]-alt-5,5'-(2,2'-bithiophene)}

MEH-PPV: short name for poly(2-methoxy,5-(20-ethyl-hexyloxy)-p-phenylene vinylene)

MDMO-PPV: short name for poly(2-methoxy-5-(30,70-dimethyloctyloxy)-1,4-phenylene vinylene)

ICMA: short name for 1',4'-Dihydro-naphtho[2',3':1,2][5,6]fullerene-C60

ICBA: short name for 1',1'',4',4''-tetrahydro di[1,4] methanonaphthaleno [5,6] fullerene-C60

ICTA: short name for the indene-C60 trisadduct

PPDT2FBT: short name for Poly[(2,5-bis(2-hexyldecyloxy)phenylene)-alt-(5,6-difluoro-4,7-di(thiophen-2-yl)benzo[c]-[1,2,5]thiadiazole)]

e-PPMF:

D18: short name for Poly[(2,6-(4,8-bis(5-(2-ethylhexyl-3-fluoro)thiophen-2-yl)-benzo[1,2-b:4,5-b']dithiophene))-alt-5,5'-(5,8-bis(4-(2-butyloctyl)thiophen-2-yl)dithieno[3',2':3,4;2'',3'':5,6]benzo[1,2-c][1,2,5]thiadiazole)]

Y6: ITIC based non fullerene acceptor, also known as BTP-4F

PBQx-TCI:

DTz-R1: Non fullerene acceptor

Acknowledgements

This thesis was written in part thanks to the help of the Institute of High-Performance Computing at A*STAR and would not have been possible without their resources and support.

This thesis is dedicated,

To Dr Tracey Clarke, guiding me through indecision and pushing me forever forward towards new heights. You have made me the Doctor I am today and I shall be forever grateful. To Dr Jose Marin-Beloqui for showing the ropes and guiding me throughout my time in London. To Jun Jun, Hristo and Caroline for sharing in the woes of experimental failures.

To Dr Michael Sullivan for always smiling while providing invaluable help and support. To Dr Ye Jun for always being there for whatever question or problem I had.

To Hughes, Joe and Nick for simulating table tops in addition to molecules.

To Joe and Kee for being wonderful roommates and friends while arriving in a new land.

To all my friends and family in France who supported me when needed and whom I sorely missed during COVID.

And most of all to Elyza, without whom I would never have been able to do this crazy endeavour.

List of Publications

Published

J. Marin-Beloqui, G. Zhang, J. Guo, J. Shaikh, **T. Wohrer**, S. M. Hosseini, B. Sun, J. Shipp, A. J. Auty, D. Chekulaev, J. Ye, Y.-C. Chin, M. B. Sullivan, A. J. Mozer, J.-S. Kim, S. Shoaee and T. M. Clarke (2021). "Insight into the Origin of Trapping in Polymer/Fullerene Blends with a Systematic Alteration of the Fullerene to Higher Adducts." The Journal of Physical Chemistry C **126**(5): 2708–2719.

UCL Research Paper Declaration Form: referencing the doctoral candidate's own published work(s)

1. For a research manuscript that has already been published (if not yet published, please skip to section 2)**:**	
a) Where was the work published? (e.g. journal name)	The Journal of Physical Chemistry C
b) Who published the work? (e.g. Elsevier/Oxford University Press):	ACS Publications
c) When was the work published?	31/01/2022
d) Was the work subject to academic peer review?	Yes
e) Have you retained the copyright for the work?	No
[If no, please seek permission from the relevant publisher and check the box next to the below statement]: ☒ *I acknowledge permission of the publisher named under 1b to include in this thesis portions of the publication named as included in 1a.*	
2. For multi-authored work, please give a statement of contribution covering all authors (if single-author, please skip to section 4**):**	
Provided insight into the HOMO of PDTSiTTz and Si-PCPDTBT through DFT calculations	
3. In which chapter(s) of your thesis can this material be found?	
Chapter 4	
4. e-Signatures confirming that the information above is accurate (this form should be co-signed by the supervisor/ senior author unless this is not appropriate, e.g. if the paper was a single-author work):	

Candidate:	Thibaut Wohrer	**Date:**	20/08/2022
Supervisor/ Senior Author (where appropriate)**:**	Tracey Clarke	**Date:**	21/08/2022

Chapter 1:
General Introduction

1.1. General Energy Overview

The world's energy market is facing a complicated conundrum that has only become more pressing in recent years: how to meet a rapidly increasing demand in energy while reducing carbon dioxide emissions. After several years of relative stagnation, the year 2018 was notable for a new rise in CO_2 emissions correlated with a resurgence of the global economy [1]. While the Covid pandemic in 2020 has somewhat afforded a reprieve[2], the recovery of the global economy[3] has put climate change once again as a pressing global matter. CO_2 emissions are problematic due to being a greenhouse gas, partially responsible for global warming. With climate change an ever-increasing concern, a change in the current status quo is needed, entailing a shift to renewable energy sources.

At present fossil fuel technologies are used in the majority of energy generation activities. These technologies have several issues. Firstly, they are inherently thermodynamically limited in efficiency by the Carnot cycle limit of 37%, insuring there is limited progress that can be made to improve these technologies. Secondly they represent one of the largest sources of total CO_2 emissions[4]. While much progress has been made to improve current fossil fuel technologies, both in efficiency and CO_2 emissions, there is a need to replace them with alternative sources. While nuclear energy is an alternative that has helped reduce emissions, it still is restricted by the same technological design principles as fossil fuel technologies and relies on finite resources. Renewable energy sources however could prove to be the viable alternative required to tackle climate change and solar energy is one such renewable energy source.

Solar power is an easy to implement technology that is able, in its current form, to supply the entire world with electricity by installing solar panels in an area of less than 500,000 square kilometres[5]. This is equivalent to an area slightly smaller than the size of Spain. It suffers from being not as cost-efficient, as well as requiring sunlight thus making it not fully reliable. Due to its potential solar power has been the focus of many studies and much research. This present thesis falls in line with the

overall aim of increasing the efficiency of solar cells thus making them a more attractive option compared to other technologies.

1.2 Solar Cells Overview

A conventional solar cell operates by converting incoming sunlight into electricity. Such a cell generally has a design as shown by ***Figure 1-1***, classified as a single-junction solar cell. When photons emitted from sunlight hit the absorber layer or active layer of the device, electrons present can become excited as per the photovoltaic effect[6]. This causes the electrons to ascend to a higher energy state, leaving a hole or positive charge behind. From there two events can occur. The excited electrons can then either return to their original state, dissipating the excess heat, or drift throughout the material until they reach a positive electrode. This electron movement creates a current throughout the device which can be harnessed to generate electricity. Key to this process is the band gap, the difference between the valence band (band of highest occupied electron energy levels) and conduction band (band of lowest vacant electron energy levels) of the material, which dictates what light can be absorbed by the device, leading to the excited electrons. This process is illustrated in ***Figure 1-2*** with the different steps for charge generation outlined in a typical p-n semiconductor. The choice of using two different materials in a negatively and positively doped semiconductor lies in the creation of an energy offset. When light is shown on this type of structure the electrons will move towards the negatively charged side and the holes towards the positive. This effect greatly improves charge movement and therefore current generated as otherwise the generated current would be too small to be of use.

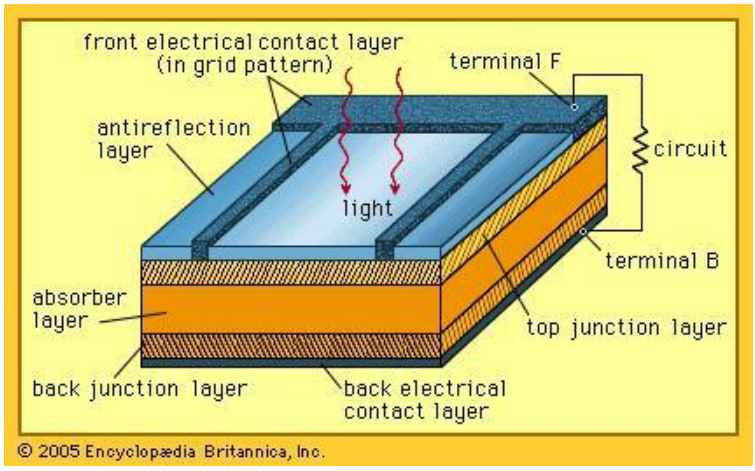

Figure 1-1: *Simplified diagram of a conventional solar cell design, taken from [7].*

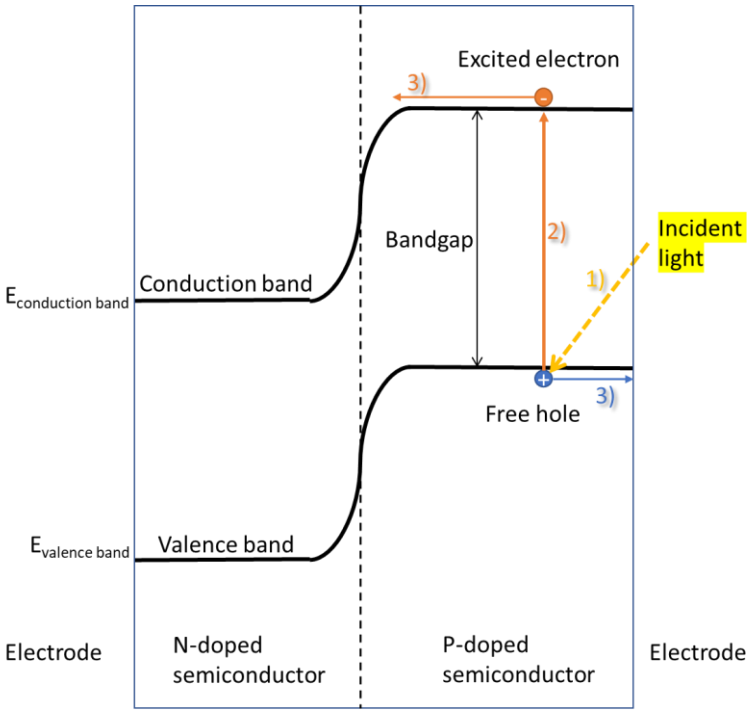

Figure 1-2: *Simplified diagram of the band diagram of a conventional solar cell design with the charge generation steps outlined as (1) light shown on the device, (2) absorption of light and (3) diffusion of charges towards respective electrodes.*

To evaluate different solar cells several parameters are measured. The key figure to gauge the performance of a solar cell is the voltage-current curve of the solar cell, with a typical curve shown in ***Figure 1-3***. This curve aims to describe the basic operation of the device by measuring the current under a varying voltage stimulus.

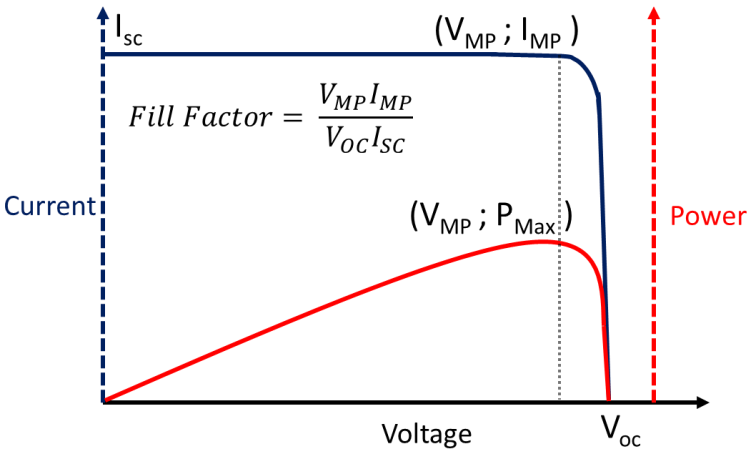

Figure 1-3:*Typical I-V curve for a conventional solar cell. I_{sc}: short circuit current, current in the device when there is no voltage across the device; V_{oc}: open circuit voltage, the voltage across the device when off; P_{max}: maximum power output; V_{MP}: voltage at maximum power output; I_{MP}: current at maximum power output.*

Using I_{sc} the short circuit current and V_{oc} the open circuit voltage defined in ***Figure 1-3*** the overall solar cell efficiency η can be defined by **Equation (1- 1)**

$$\eta = \frac{V_{OC} I_{sc} FF}{P_I} \tag{1-1}$$

with P_I the incident power and FF the Fill Factor. The equation translates to the ratio of the maximum power output of the device to the incident power of light. This equation thus gives direction for improving the efficiency of solar cells, focusing on improving specific device characteristics. Unfortunately the existence of the Shockley–Queisser limit[8] stipulates that η has a theoretical maximum value of 33.7%[9] for a single-junction conventional solar cell. This limit stems from a combination of heat dissipation through black body radiation, recombination of charges, the spectrum of sunlight not equating to pure white light and the band gap of the solar cell limiting the efficiency of absorbed photons. As this maximum value is below the target efficiency values to be able to rival other renewable and non-renewable technologies, a great deal of research has been done to circumvent this inherent limitation via various solar cell designs (such as multi-layered solar cells), material selection (materials or material combinations with a more optimised band gap) and even different types of solar cells using different technologies.

While the general principle of a solar cell, using a movement of charges to generate a potential, stays the same, different types of solar cells have emerged, differing in materials used, overall solar cell architecture and the actual charge generation process itself. Research in these different technologies has led to great advancements in efficiencies, summarised partially in ***Figure 1-4***. The highest efficiency available cells have been able to obtain efficiencies significantly higher than the Shockley–Queisser limit thanks to architectural designs such as multi-junction cells. Doing so comes at a significant cost and limited applicability. The most common silicon base solar cells using single junction architectures remain expensive to produce due to a complex supply chain fabrication, and are very limited in application, relegated to large flat surfaces[10].

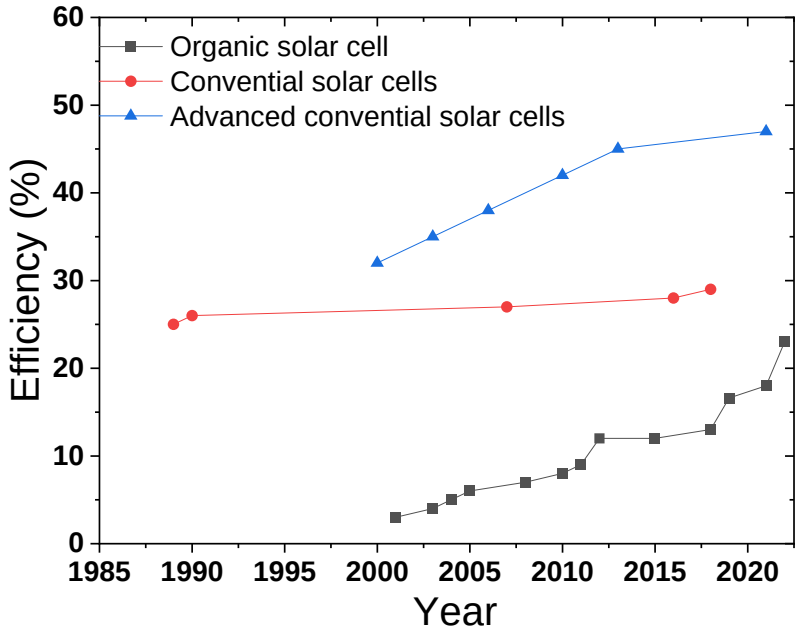

Figure 1-4: *Simplified graph of the evolution of solar cell efficiencies over time. Adapted from [11] showing the conventional commercially available solar cells using single-junction technologies (red circle) such as traditional silicon-based solar panels, the most advanced experimental solar cells based on conventional designs such as multi-junction silicon cells (blue triangle), and organic solar cells (black square) such as bulk heterojunction cells.*

Conventional single junction solar cells have stagnated in efficiency over recent years (red in ***Figure 1-4***) while the most efficient and advanced technologies have managed to reach fairly high efficiencies (blue in ***Figure 1-4***), even competitive efficiencies in comparison to fossil fuel-based technologies but do so at a significant cost. In conventional solar cells, silicon is the most widely used material in the absorber layer

thanks to its band-gap allowing it to absorb sunlight well, its availability and its processability[12]. One alternative solar cell technology that has shown increasing promise is Organic Photovoltaic cells (OPV) due to their potential as a low-cost alternative with a wide range of potential applications, notably in thin film cells. The low-cost stems from a much cheaper production while the design is not constrained to large panels such as silicon-based solar cells. Unfortunately current solar cells using this technology are lagging behind in terms of efficiency compared to conventional cells, with the highest efficiency obtained at time of writing being just over 23%[13]. It is this particular technology that is the focus of this study in an effort to continue closing the gap with traditional silicon-based technologies.

1.3. Organic photovoltaics

Organic solar cells fundamentally differ from conventional solar cells by the charge generation process used due to the materials employed. OPVs are, as the name implies, comprised of organic materials, usually conjugated polymers. These materials have a low processing cost compared to silicon, are flexible, versatile and easy to process[14]. More importantly their electronic structure, comprised of molecular orbitals, can be seen as forming an energy level structure akin to that observed in conventional inorganic materials, with the valence band and conduction band roles being filled by the Highest Occupied Molecular Orbital (HOMO) and Lowest Unoccupied Molecular Orbital (LUMO) respectively.

A very critical difference when comparing OPVs to conventional silicon-based solar cells lies with the dielectric constant. OPV materials have a significantly lower dielectric constant (3.6 for the typical OPV donor P3HT[15]) compared to 11.7 for silicon). Consequently excited electrons are more likely to interact with other charges in OPVs and not move freely to the electrodes[16] when compared to silicon. As a result, for OPVs, light absorption leads to the formation of an exciton, defined here as an electron-hole pair, instead of free-flowing charges. This exciton must first dissociate before charges may travel to the electrodes. The key force preventing this is the Coulombic attraction between the charges that creates a binding energy that

must be overcome for complete dissociation. Onsager[17] initially proposed the concept of the Coulombic capture radius defined in **Equation (1- 2)** .

$$r_c = \frac{e^2}{4\pi\varepsilon_o\varepsilon_r k_B T}$$

(1- 2)

With e the fundamental charge, ε_r the permittivity of vacuum, ε_r the dielectric constant of the material, k_B the Boltzmann constant and T the temperature. When the distance between the charges is greater than this capture radius then the charges are considered fully separated. As OPV materials have lower dielectric constants their radius is greater and therefore charges separate with greater difficulty. While this theory has since been expanded upon and refined[18], the core concept of the individual charges needing to escape this coulombic capture radius remains vital in understanding charge recombination as well as exciton dynamics, as this separation of charges is a requirement to generate current.

To tackle the challenges posed by exciton dynamics and inherent complications due to the nature of charge generation, organic solar cells have undergone several design iterations over time. The first generation of organic solar cells employed a single active layer as the medium for generating charges[19]. The issue with these designs was that the number of charges generated was severely limited as exciton dissociation was difficult. As a result, these solar cells obtained efficiencies of around 0.01%. The second generation replaced the simple active layer with a bilayer comprised of an electron donating layer and an electron accepting layer[20]. Excitons would dissociate more easily thanks to an energy offset created by these two layers and this design base led to the new band diagram described in ***Figure 1-5***. The acceptor and donor materials would act analogously to the n-doped and p-doped semiconductors in traditional silicon-based solar cells as seen in ***Figure 1-2*** However, this effect was limited to the interface between the two different regions due to the necessity of the HOMO and LUMO offsets. As such initial attempts achieved efficiencies around 1%.

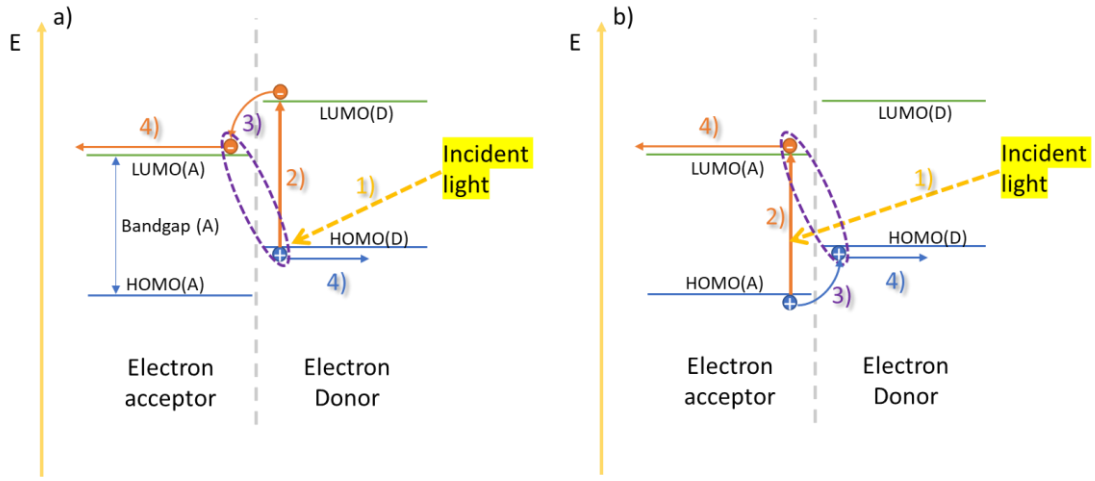

Figure 1-5: *Simplified diagram of the band diagram of an OPV solar cell design with the general charge generation steps outlined as (1) light absorption, (2) electron excitation, and formation of exciton, (3) diffusion of exciton across the acceptor-donor interface, and (4) exciton dissociation across interface and diffusion of separate charges.* ***a)*** *shows excitation in the electron donor material leading to electron hopping leading to hole hopping across interface and* ***b)*** *shows excitation in the electron acceptor material leading to hole hopping across interface*

The third generation and now most common technology uses a layer where instead of two separate regions, a blend of both with each region intertwined in the other is used, called a Bulk Heterojunction (BHJ). This blend can be a completely intermixed phase or have some homogenous phases. This technology has increased efficiency due to the increased surface area between the two donor and acceptor, leading to a larger donor/acceptor interfacial area, thus a greater area with an energy offset and thus an increase in the number of charges generated. Unfortunately, as a result of this disordered structure new limitations have arisen, notably the exciton once it dissociates can now recombine more easily before charge collection due to an increased chance of encountering opposite charges. This recombination process in particular is referred to as non-geminate or bimolecular recombination. The evolution of these first OPV designs is summarised by ***Figure 1-6*** [21].

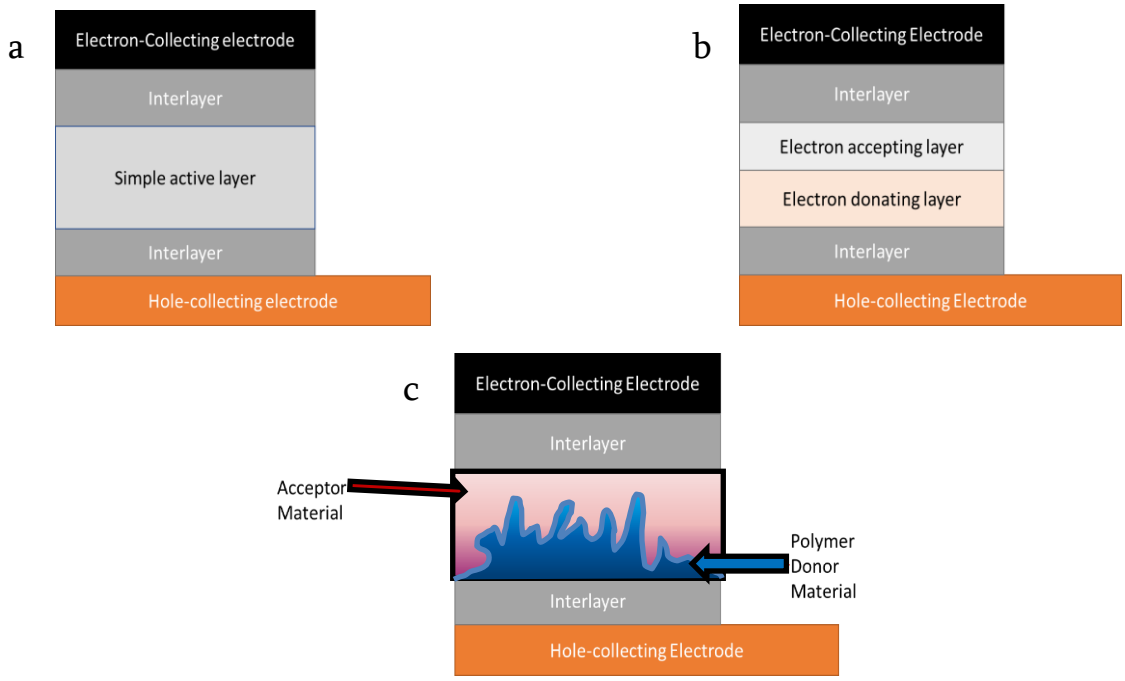

Figure 1-6: *Simplified structure of an organic photovoltaic cell with* ***a)*** *a single layer made from single material structure,* ***b)*** *bilayer structure and* ***c)*** *bulk heterojunction structure. The interlayers[22] are used to increase efficiency by facilitating charge extraction thanks to their high conductivity.*

The main evolution of the OPV designs has resided in changes to the donor/acceptor interface and the interplay between the donor and acceptor phases. Refining and improving on design choices has relied on donor and acceptor material selection, interface morphology and the dynamics between HOMO-LUMO offset and cell efficiency characteristics.[23-28]. As the next generations improved on this interface, understanding its intricacies became a priority to further understand the charge generation process and as a result continue improving OPVs.

1.4. The charge photogeneration process

The complete process, starting with the photoexcitation by incoming light and finishing with the charge separated state, is summarised in ***Figure 1-7***[29]. When photoexcitation of the donor occurs as seen in ***Figure 1-7a***, an electron is promoted to an excited state, denoted here as S_1. This photoexcitation can form an exciton from the combination of the promoted electron and the hole created during this process. Subsequently, partial dissociation of the exciton, due to in this case electron transfer from the donor to the acceptor, can lead to the formation of an exciton charge transfer state (CT state) where the electron and hole are kept bound at a thermalization length.

This CT state crucially can exist as one of two different electronic spin states, ^{1}CT and ^{3}CT. The S_1 to CT transition can only lead to ^{1}CT due to the spins of electron and hole however intersystem crossing can lead to the formation of the ^{3}CT state. This CT state can then fully decay to the ground state (geminate recombination), form a triplet state depending on the spin state or re-dissociate to eventually diffuse to the electrodes. Of note, the other pathways such as ^{3}CT to ground state are forbidden due to the spins of the exciton. Another option is for the CT state to fully dissociate into the charge-separated (CS) state as the electron and the hole become physically separated. These separated charges are often called polarons as opposed to free charges due to their interactions with the solid medium resulting in a polarized region that follows the charge as it travels through the medium. The third potential process is non-geminate or bimolecular recombination as described in ***Figure 1-7b***, where a charge generated from a molecule recombines with specifically a charge from a different molecule. The charges recombine into the ^{1}CT and ^{3}CT states at a 1:3 ratio according to spin statistics, with further recombination pathways obeying the same principles as shown in ***Figure 1-7a.*** Charges that do not recombine or re-dissociate across their journey can travel towards their respective electrodes to be collected, creating the desired current.

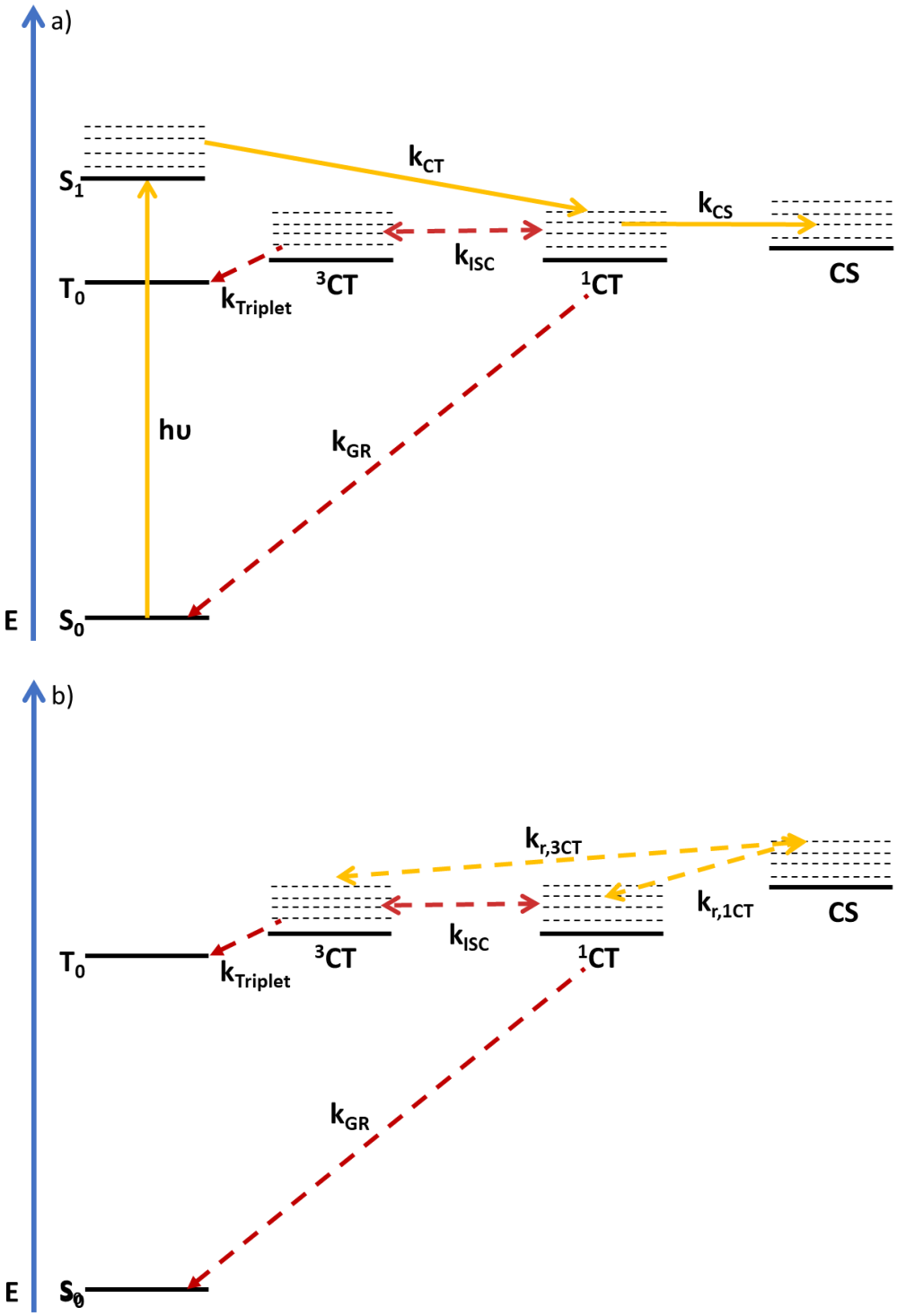

***Figure** 1-7: Energy level diagram of the main processes found in charge photogeneration in a bulk heterojunction with **a)** the energy level diagram upon photoexcitation and **b)** the bimolecular recombination energy level diagram. $h\nu$: photoexcitation; S_0: ground state; S_1: singlet exciton excited state; T_1: triplet exciton state; CT: Charge Transfer state with either spin 3 or 1; $k_{triplet}$: relaxation from ^{3}CT state to triplet state; CS: fully separated migrated charge-separated state; k_{CT}: Exciton disassociation to CT state; k_{ISC}: Intersystem crossing; k_{CS}: Full disassociation (and reverse association) from CT state to CS state; $k_{triplet}$: Geminate recombination to triplet state; k_R: bimolecular recombination of CS state to CT state; k_{GR}: recombination to ground state. Figure adapted with permission from [29].*

Highlighted in red arrows in ***Figure 1-7*** are the different loss processes of charge photo generation. These are a major source of lost efficiency in OPVs. The two different types of recombination, geminate and non-geminate, have significantly different kinetics and contributions. In most OPV cells, however, it has generally been found that bimolecular recombination is the more significant factor of the two[30]. It stands then that bimolecular recombination is the main focus of this study and will be explored in more detail.

1.5. Bimolecular recombination

The importance of understanding the bimolecular recombination loss process in the broader scope of optimizing OPVs has been highlighted by several studies. Firstly a direct link [31]has been theorised by D. Credgington and J. R. Durrant between the open circuit voltage and bimolecular recombination with **Equation (1- 3)** based on the original formulism by Shockley and Queisser[8].

$$V_{oc} = A - B * \ln\left(\frac{I_{BR}}{I_{sc}}\right)$$

(1- 3)

with I_{BR} the bimolecular recombination current, I_{SC} the short circuit current and A and B are device constants. **Equation (1- 3)** describes the open circuit voltage and is dependant on the ratio of the charge recombining in a non-geminate way over the charges being generated.

A more indirect connection has been theorised and experimentally observed for the short-circuit current density by L. J. A. Koster *et al.*[32]. The basis of this connection comes from the description of the current density as a power law against light intensity I as denoted in **Equation (1- 4)**

$$I_{sc} \propto I^{\varphi}$$

(1- 4)

The key observation that has been made relates the coefficient φ to the bimolecular recombination efficiency η_{BR} as described by **Equation (1- 5)**. This was found by modelling experimental data of an OPV device made from P3HT:$PC_{60}BM$ and observing its device characteristics as well as bimolecular recombination.

$$\eta_{BR} = \varphi^{-1} - 1$$

(1- 5)

Finally, a figure of merit was established by Neher *et al.*[33] relating the fill factor FF to the bimolecular recombination coefficient β.

$$FF = \frac{u_{OC} - \ln(0.79 + 0.66u_{OC})}{u_{OC} + 1}$$

(1- 6)

with the normalised open circuit voltage defined by

$$u_{OC} = \frac{qV_{OC}}{(1+\kappa)k_B T}$$

(1- 7)

and the figure of merit κ

$$\kappa^2 = \frac{q^2 \beta G d^4}{4\mu_e \mu_h (k_B T)^2}$$

(1- 8)

With G the generation rate and d the active layer thickness and μ the charge carrier mobility of the electron e or hole h. As such bimolecular recombination has a quantitative impact on the efficiency of OPVs and understanding this phenomenon is important to improve said efficiencies.

The dynamics of bimolecular recombination have been studied extensively ever since the prevalence of bulk-heterojunction architectures. The phenomenon itself of bimolecular recombination has been characterised in certain material systems by I. Montanari, J. R. Durrant, C. Shuttle, J. Nelson and many others [24, 34-39] as an observable kinetic power law, shown in **Equation (1- 9)**.

$$\Delta OD \propto t^{-\alpha}$$

(1- 9)

With α an exponent and t the time. This power law has been observed by multiple material systems and has successfully been modelled as bimolecular recombination limited by the presence of localised energy trap states. The gradient of the power law translates to the energetic depth of the trapping, with an α=1 alluding to a trap-free recombination process whereas a low value of α suggests energetically deep trap states. The recombination dynamics have been modelled as second-order kinetics as the

process involves two mobile independent charge carriers. This theory has been initially corroborated by several experimental results [40, 41] done on single cell OPVs. The resulting kinetics for the charge carrier density can be expressed by **Equation (1- 10)** as a second-order reaction.

$$\frac{dn(t)}{dt} = -\boldsymbol{\beta} n(t)^2$$

(1- 10)

with n(t) is the charge carrier density and β the rate constant also known as the bimolecular recombination coefficient. Initial experiments and speculations on various OPV devices such as previously mentioned studies used Langevin theory to identify β_L as, according to **Equation (1- 11)** [42],

$$\beta_L = \frac{e(\mu_e + \mu_h)}{\varepsilon\varepsilon_0}$$

(1- 11)

with ε the dielectric constant. The basis of this theory comes from examining the probability that a separated electron encounters a hole while diffusing towards the electrode and modelling Brownian motion. While this theory has proven to be correct in many cases, some differences were found for certain material systems such as P3HT. The first difference with Langevin theory was found in the order of the recombination kinetics. Experimental observations have found β to depend on charge carrier density and/or time in P3HT and PDTSiTTz combined with $PC_{60}BM$ devices[39, 43-45]. As a result, the charge carrier density can exhibit a close to third or higher order dependence instead of the expected order of two for Langevin mechanics. A prevalent hypothesis explaining this postulates that bimolecular recombination is limited by the polarons interacting with energy sinks, becoming slowed and even trapped [29, 34, 46]. Recombination would thus involve having the charges trapped in energy wells before overcoming that energy barrier and only then recombine from encountering the opposite polaron. Within this paradigm however individual factors have been found to impact the reaction order such as the spatial distribution of charges[46]. The second difference was found in the experimentally measured value of the rate constant β. Some experiments have found the rate constant $\beta_{experiment}$ to be significantly

lower than predicted by Langevin dynamics. This difference can be characterised by a ratio described by **Equation (1- 12)**, with reported discrepancy values given.

$$\gamma = \frac{\beta_{experiment}}{\beta_L} \tag{1-12}$$

$$\gamma \in [10^{-4}, 10^{-2}]$$

These discrepancies in bimolecular recombination coefficient have been extensively studied using a variety of spectroscopy and modelling methods, but no definitive explanation has been found yet. A first class of studies focused on the effects of morphology on the recombination rate. Firstly, the formation of a lamellar structure in the polymer donor region [47, 48] was reported to lead to the delocalisation of charges, and subsequent measurements of reduced bimolecular recombination, in a study by R. Osterbacka et al on a typical OPV material system P3HT:$PC_{60}BM$. G. Juska *et al.* reported for the same OPV material system that the formation of this lamella structure led to 2D-Langevin recombination within the lamella but an overall reduction in bimolecular recombination rate. This effect is corroborated by previous findings summarised by A. Pivrikas in a comprehensive review [49-51] showing that the lack of this ordered structure in certain material systems such as MDMO-PPV could lead to the return of Langevin dynamics. Morphological effects are not sufficient however to fully induce non-Langevin behaviour[52] according to a study by P. Keivanidis using various spectroscopy techniques on the familiar P3HT:$PC_{60}BM$ material system.

Looking on a broader level, various factors have been found to lead to a reduction in the bimolecular recombination rate, with some of them summarised here. In a study by C. Deibel *et al.* [53] a charge concentration and temperature gradient across the device of P3HT:$PC_{60}BM$ was found to reduce bimolecular recombination, based on an extrapolation of a model to best fit known experimental results. Similarly another model was conceived by J. Szmytkowski [54] on the very same material system, this time finding a change in the dielectric constant across the device to be a major factor. Additionally a later modelling study by B. P. Lyons[55] and subsequently corroborated by an experimental study by S. Roland *et al.*[56] on a polymer-polymer

material system P3HT:P(NDI2OD-T2) found the purity of the domains present in the device to be of paramount importance to reduce the bimolecular recombination rate. However, a key series of more recent discoveries have shed light on the bimolecular recombination process and suggest it is more complex than initially suggested. While the overall charge photogeneration process has remained consistent, several experimental studies [57, 58] by D. H. K. Murthy and A. Rao on non-P3HT material systems have alluded to bimolecular recombination being a possible multiple-step process described fully by ***Figure 1-7b***. This hypothetical framework has been studied extensively in an attempt to confirm it.

As a result of the model outline in ***Figure 1-7*** it has been suggested in a study by T. M. Burke on P3HT:$PC_{60}BM$ [59] following an initial study by L. J. A. Koster[60] on PPV: $PC_{60}BM$ that the disassociation of the CT state back to the CS state is the key process to the reduction in bimolecular recombination. Parallel to this it has been hypothesized[58] that instead it is the back electron transfer from the ^{3}CT state to the triplet and more specifically the suppression of this step that is the key factor. A third and slightly more recent study by A. Armin [61]expanded on this through a theoretical overview of multiple different models by showing that it is the simultaneous combination of CT dissociation and suppression of the back electron transfer from the ^{3}CT state to the triplet state effects that results in reduced recombination. Finally, the extent of charge delocalization in this CT state [57] has also been reported to reduce bimolecular recombination.

At the current time the overall picture has been clarified somewhat but there remain many questions left unanswered. A recent study by S. Wilken[62] went back to P3HT:$PC_{60}BM$ after this material system left the spotlight of OPV studies. Even with a system very well characterised as shown in the previously presented studies, new findings were discovered with the study showing the formation of P3HT aggregates drastically reducing the bimolecular recombination rate similar to the previously mentioned formation of lamella. Most notable was the hypothesis: aggregation, possibly from a lamella structure, can cause charge delocalisation, helping CT state dissociation and therefore reducing bimolecular recombination.

An overview of the bimolecular recombination process and the current know factors affecting it has been established. In many of the presented studies it is the P3HT:$PC_{60}BM$ material system that is used. The next section aims to provide an overview of the material selection in OPVs and explain why the combination of P3HT and $PC_{60}BM$ was used so often.

1.6 Material selection overview

Material selection for organic photovoltaics is an ongoing topic of research in a continuous quest for higher efficiencies. Many material polymers have been studied, with the first main material combination used in solution-based OPVs being a combination of the poly(2-methoxy,5-(20-ethyl-hexyloxy)-p-phenylene vinylene) or MEH-PPV donor polymer, and C_{60}[63], first reported in an inaugural paper by G. Yu *et al.*. The material combination was then subsequently substituted for poly(2-methoxy-5-(30,70-dimethyloctyloxy)-1,4-phenylene vinylene) (MDMO-PPV) and (6,6)-phenylC61-butyric acid methyl ester ($PC_{60}BM$) due to better processability. These material combinations were among those showcasing the potential of OPVs and have laid the foundations for all works to come. Unfortunately they fell to the wayside due to the limitations of the PPV-based polymers having large bandgaps and low efficiencies of around 3%[64]. The focus then shifted to one of the most widely studied and previously prevalent material choices in the combination of poly(3-nhexylthiophene) (P3HT) for the donor material and $PC_{60}BM$ for the acceptor material.

P3HT's success stemmed from its cost effectiveness[65], processability[66], stability, band gap and environment friendliness[67]. This has given the donor polymer the spotlight for many years as the chosen top material of choice and allowed the elucidation of many critical factors governing OPVs recombination mechanisms and general device optimisation, as detailed in studies previously mentioned. Unfortunately P3HT only absorbs [68] around 25% of the incident sunlight, limiting its potential for higher energy outputs and the main reason for its decline in interest in state-of-the-art OPV devices. $PC_{60}BM$ on the other hand was chosen for its ability

to limit charge recombination[69] in addition to its processability and, more importantly, its femtosecond-timescale electron transfer[70]. This combination has managed to produce solar cells of up to around 5% efficiency. P3HT and $PC_{60}BM$ are still used in studies today however, due to how well characterised they are overall, serving as a great comparison tool.

From this notable material combination several optimisation routes emerged. A first category focused on improving actual device design with the development of ternary blend bulk heterojunctions[71] as well as tandem cell designs in order to offset the limitations of P3HT. Another route instead focused on optimisation of the acceptor molecules, first looking at improving the ability of the fullerene molecules to harvest light due to their poor visible light absorption by the synthesis of fullerene variants such as ICMA, ICBA and ICTA[72]. These have allowed OPVs with an efficiency of up to 8.11% when using the isomer-free fullerene derivative e-PPMF combined with the low bandgap polymer PPDT2FBT. In parallel to this however non-fullerene acceptors were developed and quickly proved their worth with a 6.8% efficiency found with the ITIC molecule[73] thanks to a much larger visible light absorption capability. These non-fullerene acceptor quickly overtook their traditional fullerene counterparts with the high efficiencies of 18% found with a device combining the copolymer D18 and the low bandgap acceptor Y6[74] and the highest efficiency of 23%[13] found with a device combining the low charge disorder PBQx-TCI donor polymer with the crystalline and low energetic disorder DTz-R1 acceptor.

Even with these advances in efficiency, fullerene acceptors have remained at the forefront of many studies, with even P3HT:$PC_{60}BM$ still a relevant material combination today[62, 75-77]. Part of this paradigm lies in the donor molecules being specifically synthesized to compliment the acceptor molecules of interest. This in turn makes these non-fullerene acceptors more limited in applicability when compared to fullerenes, with $PC_{60}BM$ finding compatibility with many different donor polymers[78]. Moreover, while non-fullerene acceptors have been found to have higher light absorption, spectroscopy is made significantly more difficult for examination of the donor molecule as spectral features such as absorption peaks

overlapping may make characterisation difficult. In addition, while non-fullerene acceptors have received substantial attention recently, they lag behind the sheer prevalence of fullerenes in the literature and thus the ease of comparison and understanding fullerenes provide. Thus, fullerenes remain the most well-suited class of acceptor for a better understanding of the underlying mechanisms governing OPVs through the study of donor polymers. It is therefore for the ubiquity of fullerenes in the literature, the easier spectroscopy characterisation and greater compatibility that fullerenes were chosen in this study. The donor material chosen as the centre of this study was the more obscure ZZ115 donor polymer as shown in ***Figure 1-8***

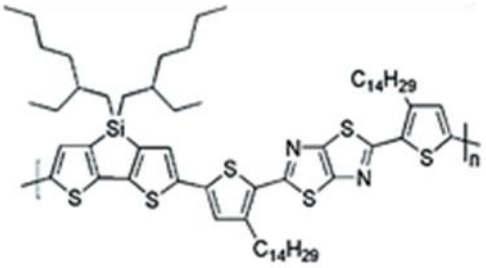

Figure 1-8: *Molecular structure of ZZ115.*

The donor-acceptor copolymer PDTSiTTz, also known as KP115 or ZZ115, short name for poly((4,4′-bis(2-ethylhexyl) dithieno (3,2-b:2′,3′-d) silole)-2,6-diyl-alt-(2,5-bis 3-tetradecylthiophen-2-yl thiazolo 5,4-d thiazole)-2,5diyl), was first synthesized in a 2011 paper by Jeff Peet *et al.* [79]. ZZ115 was reported to have high hole mobility and HOMO and LUMO energy level values similar to other OPV donor materials, making it a good choice as a donor material for OPVs. In addition, an excellent thermal stability at ideal OPV operating temperatures was found for this polymer. Additional studies have provided supplementary information on the stability of ZZ115-based OPVs, finding improved photochemical stability compared to P3HT[80]. Device performances using this material were found to be around 5%[81]. More importantly a non-Langevin behaviour was reported when combined with certain acceptors[82], a behaviour not shared by many material sets and an attractive avenue for device optimization. While ZZ115 is at present not a suitable candidate for optimal OPV devices from a pure device performance standpoint, its ease of experimental characterisation and measurement makes it an ideal candidate for a better understanding of the still unexplained behaviour in non-Langevin bimolecular

recombination. As bimolecular recombination is still one of the major loss mechanisms of OPVs, it is for this ease of characterisation that this material was chosen to be studied in this thesis.

1.7 Aim of study and research question

OPVs offer a unique solution to the ever-looming global crisis that is climate change. Great advances have been made in improving this technology to be commercially viable, but many obstacles remain before OPVs become competitive with established technologies. One avenue that remains unsolved lies in the bimolecular recombination process, a non-trivial loss process, and the factors that govern it. More specifically the complete mechanism is not fully understood and the causes of the non-Langevin behaviour remain unclear. It is thus the aim of this study to provide additional insight on the bimolecular recombination process, specifically on the possible morphological and electronic factors that may influence the process as well as possible factors giving rise to the non-Langevin behaviour, by the way of a combined experimental and computational study on a material known to exhibit highly unusual photo electric properties, ZZ115.

1.8 References

1. C. Figueres, C. Le Quéré, G. P. Peters, G. Whiteman, A. Mahindra, D. Guan, and e. al., *Emissions are still rising: ramp up the cuts.* Nature, 2018. **564**: p. 27-30.
2. C. Le Quéré, et al., *Temporary reduction in daily global CO2 emissions during the COVID-19 forced confinement.* Nature Climate Change, 2020. **10**.
3. M. Romanello and Et Al., *The 2021 report of the Lancet Countdown on health and climate change: code red for a healthy future.* The Lancet, 2021. **398**(10311).
4. Eurostat. *Greenhouse gas emission statistics - emission inventories*. 2018 cited 219; Available from: (http://ec.europa.eu/eurostat/statisticsexplained).

5. Initiative, L.A.G. *Total Surface Area Required to Fuel the World With Solar*. 2009 2015 [cited 2019.
6. Y. N. Sudhakar, M. Selvakumar, and D. KrishnaBhat, *Chapter 4 - Biopolymer Electrolytes for Solar Cells and Electrochemical Cells*, in *Biopolymer Electrolytes*. 2018. p. 117-149.
7. S. Ashok, R. T. Fonash, and S.J. Fonash, *Solar Cell*, in *ENCYCLOPÆDIA BRITANNICA*. 2018.
8. W. Shockley and H. J. Queisser, *Detailed Balance Limit of Efficiency of p-n Junction Solar Cells.* Journal of Applied Physics, 1961. **32**: p. 510-519.
9. Rühle, S., *Tabulated values of the Shockley–Queisser limit for single junction solar cells.* Solar Energy 2016. **130**.
10. A. C. Goodrich, D. M. Powell, T. L. James, M. Woodhousea, and T. Buonassisi, *Assessing the drivers of regional trends in solar photovoltaic manufacturing.* Energy and Environmental science, 2013. **6**(10): p. 2811-2821.
11. NREL, *Best Research-Cell Efficiencies.* 2018.
12. L. A. Dobrzanski, L. Wosinska, B. Dolzanska, and A. Drygala, *Comparison of electrical characteristics of silicon solar cells.* Journal of Achievments in Materials and Manufacturing Engineering, 2006. **18**(1).
13. Y. Cui, et al., *100 cm2 Organic Photovoltaic Cells with 23% Efficiency under Indoor Illumination.* Chinese Jounral of Polymer Science, 2022. **40**.
14. A. Gambhir, P. Sandwell, and J. Nelson, *The future costs of OPV – A bottom-up model of material and manufacturing costs with uncertainty analysis.* Solar Energy Materials & Solar Cells, 2016. **156**.
15. M. P. Hughes, K. D. Rosenthal, N. A. Ran, M. Seifrid, G. C. Bazan, and T-Q Nguyen, *Determining the Dielectric Constants of Organic Photovoltaic Materials Using Impedance Spectroscopy.* Advanced Functional Materials, 2018.
16. J.-L. Bredas, J. Cornil, and A.J. Heeger, *The exciton binding energy in luminescent conjugated polymers.* Adv. Mater., 1996. **8**.

17. L. Onsager, *Electric Moments of Molecules in Liquids.* J. Am. Chem. Soc., 1936. **58**(8): p. 1486–1493.
18. C. L. Braun, *Electric field assisted dissociation of charge transfer states as a mechanism of photocarrier production* J. Chem. Phys., 1984. **80**.
19. T-S. Li, C.-H. Tsai, S.-H. Kao, I-W. Wu, J.-Z. Chen, C.-I Wu, C.-F. Lin, and I-C. Cheng, *Single-layer organic–inorganic-hybrid thin-film encapsulation for organic solar cells.* Journal of Physics D: Applied Physics, 2013. **46**.
20. Tang, C.W., *Two-layer organic photovoltaic cell* Appl. Phys. Lett. , 1986. **48**(183).
21. P. P. Kumavat, P. Sonar, and D.S. Dalal, *An overview on basics of organic and dye sensitized solar cells, their mechanism and recent improvements.* Renewable and Sustainable Energy Reviews, 2017. **78**: p. 1262-1287.
22. T.-H Lai, S.-W. Tsang, J. R. Manders, S. Chen, and F. So, *Properties of interlayer for organic photovoltaics.* Materials Today, 2013. **16**(11).
23. M. C. Scharber, D. Muhlbacher, M. Koppe, P. Denk, C. Waldauf, A. J. Heeger, and C.J. Brabec, *Design Rules for Donors in Bulk-Heterojunction Solar Cells—Towards 10 % Energy-Conversion Efficiency.* Advanced Materials, 2006. **18**(6).
24. H. Ohkita, et al., *Charge Carrier Formation in Polythiophene/Fullerene Blend Films Studied by Transient Absorption Spectroscopy.* Journal of the American Chemical Society, 2008. **130**(10).
25. T. Unger, S. Wedler, F.-J. Kahle, U. Scherf, H. Bassler, and A. Kohler, *The Impact of Driving Force and Temperature on the Electron Transfer in Donor–Acceptor Blend Systems.* The journal of Physical Chemistry C, 2017. **121**.
26. Y. L. Lin, M. A. Fusella, and B. P. Rand, *The Impact of Local Morphology on Organic Donor/Acceptor Charge Transfer States.* Advanced energy Materials, 2018. **8**.
27. J. Zhang, W. Li, G. Zhou, Y. Yi, S. Xu, F. Liu, H. Zhu, and X. Zhu, *Accurate Determination of the Minimum HOMO Offset for Efficient Charge*

Generation using Organic Semiconducting Alloys. Advanced energy Materials, 2019. **10**(5).

28. M. P. Aplan, et al., *Revealing the Importance of Energetic and Entropic Contributions to the Driving Force for Charge Photogeneration.* ACS Applied Materials and Interfaces, 2018. **10**(46).
29. T. M. Clarke and J.R. Durrant, *Charge Photogeneration in Organic Solar Cells.* American Chemical Society, 2010.
30. D.Credgington, R. Hamilton, P. Atienzar, J. Nelson, and J.R. Durrant, *Non-Geminate Recombination as the Primary Determinant of Open-Circuit Voltage in Polythiophene:Fullerene Blend Solar Cells: an Analysis of the Influence of Device Processing Conditions.* Advanced Functional Materials, 2011. **21**(14).
31. D. Credgington and J. R. Durrant, *Insights from Transient Optoelectronic Analyses on the Open-Circuit Voltage of Organic Solar Cells.* J. Phys. Chem. Lett., 2012. **3**(11): p. 1465–1478.
32. L. J. A. Koster, M. Kemerink, M. M. Wienk, K. Maturova, and R. A. J. Janssen, *Quantifying Bimolecular Recombination Losses in Organic Bulk Heterojunction Solar Cells.* Advanced Materials, 2011. **23**(14).
33. D. Neher, J. Kniepert, A. Elimelech, and L.J.A. Koster, *A New Figure of Merit for Organic Solar Cells with Transport-limited Photocurrents.* Scientific Reports, 2016. **6**.
34. J. Nelson, *Diffusion recombination in polymer-fullerene blends and its influence on photocurrent collection.* Physical Review B, 2003. **67**(15).
35. I. Montanari, A. F. Nogueira, J. Nelson, J. R. Durrant, C. Winder, M. A. Loi, N. S. Sariciftci, and C. Brabec, *Transient optical studies of charge recombination dynamics in a polymer/fullerene composite at room temperature.* Applied Physics Letters, 2002. **81**(16).
36. A. F. Nogueira, I. Montanari, J. Nelson, J. R. Durrant, C. Winder, N. S. Sariciftci, and C. Brabec, *Charge Recombination in Conjugated Polymer/Fullerene Blended Films Studied by Transient Absorption Spectroscopy.* J. Phys. Chem. B, 2003. **107**.

37. C. G. Shuttle, B. O'Regan, A. M. Ballantyne, J. Nelson, D. D. C. Bradley, and J.R. Durrant, *Bimolecular recombination losses in polythiophene: Fullerene solar cells.* Physical Review B, 2008.

38. T. M. Clarke, F. C. Jamieson, and J.R. Durrant, *Transient Absorption Studies of Bimolecular Recombination Dynamics in Polythiophene/Fullerene Blend Films.* J. Phys. Chem. C., 2009. **113**(49): p. 20934–20941.

39. T. M. Clarke, C. Lungenschmied, J. Peet, N. Drolet, and A. .J. Mozer, *A Comparison of Five Experimental Techniques to Measure Charge Carrier Lifetime in Polymer/Fullerene Solar Cells.* Advanced Energy Materials, 2014. **5**(4).

40. S. R. Cowan, N. Banerji, W. L. Leong, and A.J. Heeger, *Charge Formation, Recombination, and Sweep-Out Dynamics in Organic Solar Cells.* Advanced Functional Materials, 2012. **22**(6).

41. N. Karl and G. Sommer, *Field Dependent Losses of Electrons and Holes by Bimolecular Volume Recombination in the Excitation Layer of Anthracene Single Crystals Studied by Drift Current Pulses.* physica status solidi, 1971. **6**(1).

42. D. S. Lmons and A. Gythiel, *Paul Langevin's 1908 paper "On the Theory of Brownian Motion" ["Sur la théorie du mouvement brownien," C. R. Acad. Sci. (Paris) 146, 530–533 (1908)].* American Journal of Physics 1997. **65**.

43. T. M. Clarke, J. Peet, P. Denk, G. Dennler, C. Lungenschmied, and A. .J. Mozer, *Non-Langevin bimolecular recombination in a silole-based polymer:PCBM solar cell measured by time-resolved charge extraction and resistance-dependent time-of-flight techniques* Energy and Environmental Science, 2012(1).

44. C. Göhler, A. Wagenpfahl, and C. Deibel, *Nongeminate Recombination in Organic Solar Cells.* Advanced Electronic Materials, 2018. **4**(10).

45. J. Gorenflot, M. C. Heiber, A. Baumann, J. Lorrmann, M. Gunz, A. Kampgen, V. Dyakonov, and C. Deibel, *Nongeminate recombination in neat P3HT and P3HT:PCBM blend films* Journal of Applied Physics, 2014. **115**.

46. T. Kirchartz and J. Nelson, *Meaning of reaction orders in polymer:fullerene solar cells.* Physical Review B, 2012.

47. R. Osterbacka, A. Pivrikas, G. Juska, A. Poskus, H. Aarnio, G. Sliauzys, K. Genevicius, K. Arlauskas, and N. S. Sariciftci, *Effect of 2-D Delocalization on Charge Transport and Recombination in Bulk-Heterojunction Solar Cells.* IEEE Journal of Selected Topics in Quantum Electronics, 2010. **16**(6): p. 1738 - 1745.

48. G. Juška, K. Genevičius, N. Nekrašas, G. Sliaužys, and R. Österbacka, *Two dimensional Langevin recombination in regioregular poly(3-hexylthiophene).* Appl. Phys. Lett., 2009. **95**.

49. A. Pivrikas, N.S.S., G. Juška, and R. Österbacka, *A review of charge transport and recombination in polymer/fullerene organic solar cells.* Prog. Photovolt. , 2007. **15**: p. 677–696.

50. F. Padinger, R. S. Ritterger, and N. S. Sariciftci, *Effects of Postproduction Treatment on Plastic Solar Cells.* Advanced Functional Materials, 2003. **13**(1).

51. M. Obarowska and J. Godlewski, *Electric Field dependence of the bimolecular recombination rate of the charge carriers.* Synthetic Metals, 2000. **109**(1-3).

52. P. E. Keivanidis, T. M. Clarke, S. Lilliu, T. Agostinelli, J. E. Macdonald, J. R. Durrant, D. D. C. Bradley, and J. Nelson, *Dependence of Charge Separation Efficiency on Film Microstructure in Poly(3-hexylthiophene-2,5-diyl):[6,6]-Phenyl-C61 Butyric Acid Methyl Ester Blend Films.* The Journal of Chemical Physics Letters, 2010. **1**(4).

53. C. Deibel and A. Wagenpfahl, *Origin of reduced polaron recombination in organic semiconductor devices.* PHYSICAL REVIEW B, 2009. **80**.

54. J.Szmytkowski, *Analysis of the image force effects on the recombination at the donor–acceptor interface in organic bulk heterojunction solar cells.* Chemical Physics Letters, 2009. **470**(1-3): p. 123-125.

55. B. P. Lyons, N. Clarke, and C. Groves, *The relative importance of domain size, domain purity and domain interfaces to the performance of bulk-*

heterojunction organic photovoltaics. Energy and Environmental Science, 2012(6).

56. S. Roland, M. Schubert, B. A. Collins, J. Kurpiers, Z. Chen, A. Facchetti, H. Ade, and D. Neher, *Fullerene-Free Polymer Solar Cells with Highly Reduced Bimolecular Recombination and Field-Independent Charge Carrier Generation.* American Chemical Society, 2014.
57. D. H. K. Murthy, A. Melianas, Z. Tang, G. Juška, K. Arlauskas, F. Zhang, L. D. A. Siebbeles, O. Inganäs, and T.J. Savenije, *Origin of Reduced Bimolecular Recombination in Blends of Conjugated Polymers and Fullerenes.* Advanced Functional Materials, 2013. **23**(34).
58. A. Rao, P. C. Y. Chow, S. Gelinas, C. W. Schlenker, C-Z. Li, H-L. Yip, A. K.-Y. Jen, D. S. Ginger, and R. H. Friend, *The role of spin in the kinetic control ofrecombination in organic photovoltaics.* Nature, 2013. **500**: p. 435–439.
59. T. M. Burke, S. Sweetnam, K. Vandewal, and M.D. McGehee, *Beyond Langevin Recombination: How Equilibrium Between Free Carriers and Charge Transfer States Determines the Open-Circuit Voltage of Organic Solar Cells.* Advanced Energy Materials, 2015. **5**(11).
60. L. J. A. Koster, E. C. P. Smits, V. D. Mihailetchi, and P. W. M. Blom, *Device model for the operation of polymer/fullerene bulk heterojunction solar cells.* Physcial Review B, 2005.
61. A. Armin, J.R. Durrant, and S. Shoaee, *Interplay between triplet, singlet-charge transfer states and free charge carriers defining Bimolecular Recombination Rate Constant of Organic Solar Cells.* Physical Chemistry C, 2017. **121**(25): p. 13969–13976.
62. S. Wilken, D. Scheunemann, S. Dahlström, M. Nyman, J. Parisi, and R. Österbacka, *How to Reduce Charge Recombination in Organic Solar Cells: There are Still Lessons to Learn from P3HT:PCBM.* Advanced Electronic Materials, 2021. **7**(5).
63. G. Yu, J. Gao, J. C. Hummelen, F. Wudl, and A.J. Heeger, *Polymer Photovoltaic Cells: Enhanced Efficiencies via a Network of Internal Donor-Acceptor Heterojunctions.* Science 1995. **270**(5243).

64. C. J. Brabec, S. E. Shaheen, C. Winder, and N.S. Sariciftci, *Effect of LiF/metal electrodes on the performance of plastic solar cells.* Applied Physics Letters, 2002. **80**(7).

65. M. Trung Dang, L. Hirsch, and G. Wantz, *P3HT:PCBM, Best Seller in Polymer Photovoltaic Research.* Advanced Materials, 2011. **23**(31): p. 3597-3602.

66. G. Weihao, *An overview on P3HT:PCBM, the most efficient organic solar cell material so far. .* Solid State Physics II, 2009.

67. S. Rafique, S. M. Abdullah, K. Sulaiman, and M. Iwamoto., *Fundamentals of bulk heterojunction organic solar cells: An overview of stability/degradation issues and strategies for improvement.* Renewable and Sustainable Energy Reviews, 2018. **84**: p. 43-53.

68. G. V. Bulavko and A.A. Ishchenko, *Organic bulk heterojunction photovoltaic structures: design, morphology and properties.* Russian Chemical Reviews, 2014.

69. R. Mauer, M. Kastler, and F. Laquai, *The Impact of Polymer Regioregularity on Charge Transport and Efficiency of P3HT:PCBM Photovoltaic Devices.* Advanced Functional Materials, 2010. **20**(13).

70. R. A. Marsh, J. M. Hodgkiss, S. Albert-Seifried, and R. H. Friend, *Effect of Annealing on P3HT:PCBM Charge Transfer and Nanoscale Morphology Probed by Ultrafast Spectroscopy.* Nano Letters, 2010. **10**(3).

71. M. G. Murali, A. D. Rao, S. Yadav, and P.C. Ramamurthy, *Narrow band gap conjugated polymer for improving the photovoltaic performance of P3HT:PCBM ternary blend bulk heterojunction solar cells.* Polymer Chemistry, 2014. **6**.

72. Y. He and Y. Li, *Fullerene derivative acceptors for high performance polymer solar cells* Phys. Chem. Chem. Phys., , 2011. **13**: p. 1970-1983

73. Y. Lin, J. Wang, Z-G. Zhang, H. Bai, Y. Li, D. Zhu, and X. Zhan, *An Electron Acceptor Challenging Fullerenes for Efficient Polymer Solar Cells.* Advanced Materials, 2015. **27**(7).

74. Q. Liu, Y.J., K. Jin, J. Qin, J. Xu, W. Li, J. Xiong, J. Liu, Z. Xiao, K. Sun, S. Yang, X. Zhang, L. Ding,, *18% Efficiency organic solar cells.* Science Bulletin, 2020. **65**(4).

75. D. Han, Y. Han, Y. Kim, J.-W. Lee, D. Jeong, H. Park, G.-U. Kim, F. S. Kim, and B. J. Kim, *Efficient, thermally stable poly(3-hexylthiophene)-based organic solar cells achieved by non-covalently fused-ring small molecule acceptors.* Journal of Materials Chemistry A, 2022(2).

76. K. Xian, et al., *Delicate crystallinity control enables high-efficiency P3HT organic photovoltaic cells.* Journal of Materials Chemistry A, 2022(7).

77. Y. Liu, et al., *A Mixed-Ligand Strategy to Modulate P3HT Regioregularity for High-Efficiency Solar Cells.* Macromolecules, 2022. **55**(8).

78. F. Hakim and K. Alam, *Optimization and performance analysis of PCBM acceptor-based bulk heterojunction organic solar cells using different donor materials*, in *International Conference on Electrical and Computer Engineering*. 2016, IEEE: Dhaka, Bangladesh.

79. J. Peet, et al., *Bulk heterojunction solar cells with thick active layers and high fill factors enabled by a bithiophene-co-thiazolothiazole push-pull copolymer.* Applied Physics Letters, 2011. **98**(4).

80. J. E. Carlé, M. Helgesen, M.V. Madsen, E. Bundgaard, and F.C. Krebs, *Upscaling from single cells to modules—fabrication of vacuum- and ito-free polymer solar cells on flexible substrates with long lifetime.* J. Mater. Chem. C. , 2014. **2**: p. 1290–1297.

81. Heumüller, T., *Impact of Microstructure on the Photostability of Organic Bulk Heterojunction Solar Cells*. 2016.

82. T. M. Clarke, C. Lungenschmied, J. Peet, N. Drolet, K. Sunahara, A. Furube, and A.J. Mozer, *Photodegradation in Encapsulated Silole-Based Polymer: PCBM Solar Cells Investigated using Transient Absorption Spectroscopy and Charge Extraction Measurements* Advanced Energy Materials, 2013. **3**: p. 1473-1483.

Chapter 2: General Methodology

2.1 Introduction

The main objective of the thesis lies in gaining insight in the bimolecular recombination process within the ZZ115 donor polymer described in Chapter **1** Section **1.6**. To that end the characterisation and study were done using a combination of experimental ground state and transient techniques, and computational modelling of the ground state and excited state of ZZ115 as well as charge carrier dynamics. In order to explain in more detail, the reasoning behind the chosen techniques, a brief explanation of each technique is given.

2.2 Experimental methodology

2.2.1 UV-VIS spectroscopy

One of the most important techniques used to characterise polymer-based samples involves determining the ground state absorption of the material. When an electromagnetic wave passes through a material, this leads to the excitation of the electrons from an initial ground state to a higher energy state as summarised by ***Figure 2-1***. This excitation from absorption of the light can be followed by a vibrational or non-radiative relaxation and then further relaxation to the ground state via fluorescence emission.

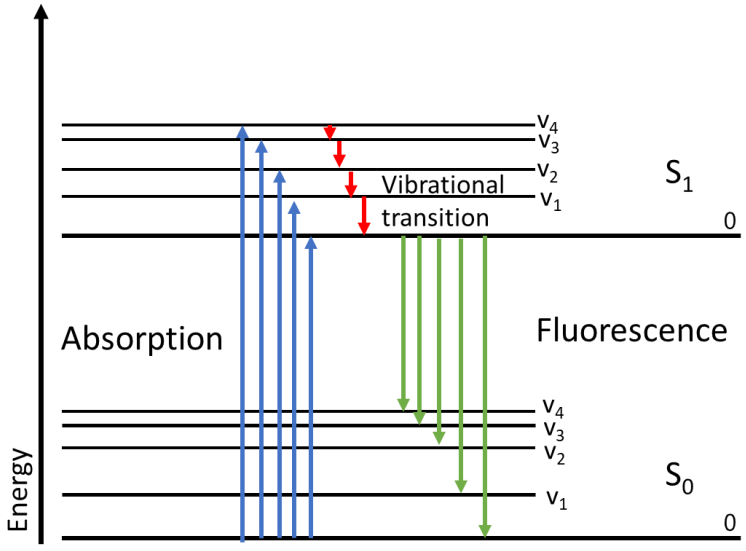

Figure 2-1: *Simplified Jablonski diagram describing the absorption (blue) and fluorescence (green) processes. S_0 and S_1 denote electronic energy states while the numbers v_x denote the individual vibrational states.*

The visible transitions for molecules are identified in UV-VIS as the first the 0-0 transition, corresponding to the S_0 v_0 to S_1 v_0, then the 0-1 transition, corresponding to the S_0 v_0 to S_1 v_1 etc… As outlined in Chapter **1** Section **1.3** the organic molecules used in OPVs are defined by conjugated backbones of carbon double bonds which form the HOMO-LUMO. The result of this conjugation is a red shift in carbon-carbon double bond transition caused by the energy gap of the HOMO and LUMO decreasing from the increased number of orbitals (butadiene for example has a transition at 217 nm, hexatriene has one at 258 nm etc…). Most importantly this transition is visible using UV-VIS spectroscopy and as such this technique can measure the level of conjugation of a polymer. Conversely other types of bonds and transitions have been characterised in the literature, allowing the optically active groups to be identified from a UV-VIS spectrum.

The aim of UV-VIS spectroscopy in the context of this thesis is the following. Firstly, it serves as a tool to check if the samples to be measured are of the correct material and of sufficient quality and thickness, while also assisting with sample reproducibility and assessing sample crystallinity. Secondly, it is used to determine the best wavelengths for photoexcitation of the sample, a parameter important in other spectroscopy techniques used in this thesis. Finally, UV-VIS measurements give a quantitative view of the vibrational structure of the material system of interest. It is important to note that UV-VIS spectroscopy does not measure the absorption of the material directly but instead the absorbance of the material. Absorption corresponds to the ability of a material to absorb light while absorbance measures the attenuation of the incident light as it passes through the material and includes other light phenomena such as reflection and scattering. While the exact absorption is more difficult to determine, the absorbance still provides the desired information regarding the key transitions and features of a material.

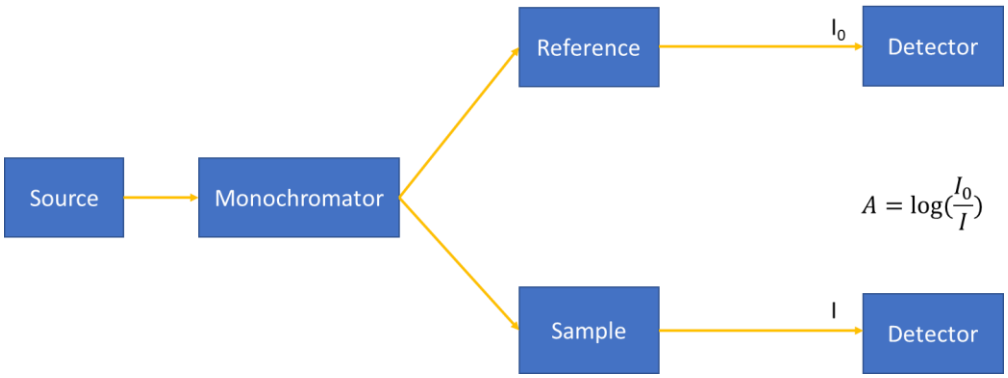

Figure 2-2: *Simplified diagram of UV-VIS spectroscopy. The equation defines Absorbance A as the log of the ratio of the reference intensity I_0 over the measured intensity I.*

The UV-VIS spectrometer used operates in the following way as summarised by ***Figure 2-2***. A beam of light is generated from a light source and passes through a monochromator to produce a beam of light of a specific probe wavelength. This beam then passes through the sample and the intensity of this beam I is measured. This intensity is compared to a reference intensity I_0, the intensity of a beam of light passing through a blank, in order to take into account the effects of the substrate or solvent. The sample is then probed at varying wavelengths and the absorbance A is calculated with **Equation (2-1)** at different wavelengths to obtain a spectrum.

$$A = \log\left(\frac{I_0}{I}\right) \tag{2-1}$$

The absorbance of a material is significant due to the Bouguer-Beer-Lambert law described by **Equation (2-2)**

$$A = \varepsilon c l \tag{2-2}$$

With ε the molar attenuation coefficient, c the concentration of the species and l the optical path length of the sample. The molar attenuation coefficient represents how well the material can absorb an incident light passing through it and is a characteristic of the material. The Bouguer-Beer-Lambert law does however have limitations in that it is only suited to describe low concentration liquid mediums[1]. The law remains useful however for an approximated view of the species concentration and to assess sample homogeneity, crystallinity, and quality due to the associated deviations with

the Bouguer-Beer-Lambert law. For this thesis the measurements were done using a commercial setup comprised of a Lambda 365 (PerkinElmer) machine.

2.2.2 Photoluminescence spectroscopy (PL)

Another useful technique to study the photo optical properties of a material is photoluminescence spectroscopy. When a photon is absorbed by a material, this can lead to a singlet excited state as described previously in ***Figure 2-1***. This singlet can then relax back to the ground state, emitting a photon through the process of fluorescence. This specific emission notably is at a longer wavelength than the excitation wavelength that led to it due to a phenomenon called the Stokes Shift[2]. The Stokes Shift can therefore describe the vibrational relaxation process. Within the context of this study, this fluorescence is important as it can provide additional information on the vibrational structure of the material but can also hamper measurements made with other spectroscopy techniques if the fluorescence overlaps with transient features in wavelength. Fluorescence is also important when considering the quenching of fluorescing species, most notably excitons[3]. The quenching of a fluorescing species results from the replacement of the excited state fluorescence relaxation by another transition. An exciton quenching can be caused by many factors and transitions. The most notable transition for exciton quenching is exciton dissociation into free charges. Introduction of fullerenes[4] for example leads to a significant quenching due to exciton dissociation. However many other factors such as inhomogeneous regions in amorphous domains[5] can also lead to this quenching, making PL spectroscopy a powerful tool to assess various effects on the exciton in OPVs. Within the context of this study, PL is used to assess the effects of fullerene introduction in ZZ115 and the possible resulting exciton quenching in addition to identifying spectral regions where the fluorescence of species in ZZ115 material systems will cause other transient features to possibly appear masked.

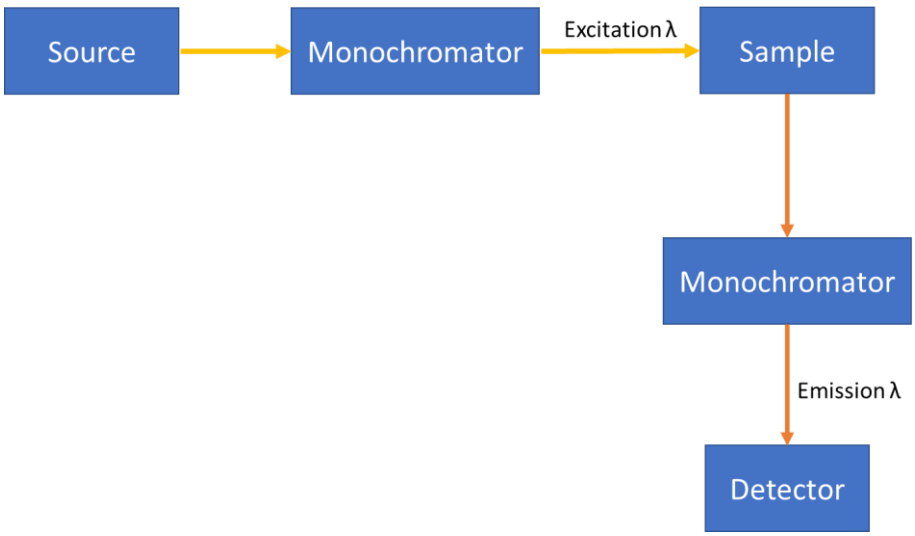

Figure 2-3: *Simplified diagram of PL spectroscopy.*

The PL spectrometer operates as shown by ***Figure 2-3*** [6]. A beam of light, separated to a single wavelength by a monochromator, is shone on a sample. The luminescence emitted by the sample is separated by another different monochromator and then measured by a detector to be plotted as a spectrum. The excitation wavelength is determined depending on the ground state absorbance of the sample. For this thesis the measurements were done using a commercial setup comprised of a Fluorolog 3 (Horiba) commercial instrument.

2.2.3 Transient Absorption Spectroscopy (TAS)

While the above techniques are well suited to identify steady-state features, a different technique is needed to characterise species with short lifetimes. Transient absorption spectroscopy allows the measurement of transient photo excited species with short lifetimes. Depending on the exact lifetime of the species that one wants to observe, different experimental setups are necessary. This chapter focuses on microsecond-TAS due to the timescales of the main species of interest for both Chapters **3** and **4**.

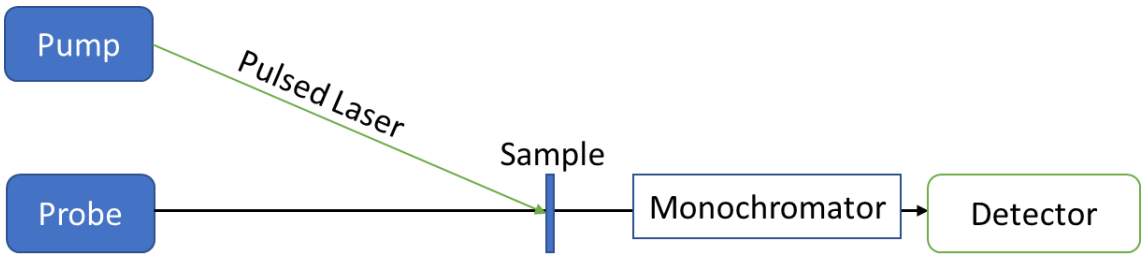

Figure 2-4: *Simplified diagram of an ns-ms transient absorption spectroscopy set-up.*

The sample, in an air-quartz cuvette surrounded by a chosen gaseous environment in the case of a solid sample, is excited by a pump laser pulse at a given frequency and pulse width. The time resolution, which governs the types of transient species that can be observed, is limited in this set-up by the resolution of the detector segment, specifically the voltage resolution of the oscilloscope. The gaseous environment can influence which transient species will be visible. While the sample is excited intermittingly a probe lamp is guided through the sample. This probe light passing through the sample is then directed through a monochromator, separating the wavelengths of the incoming signal. Finally, this separated signal is recorded by a detector.

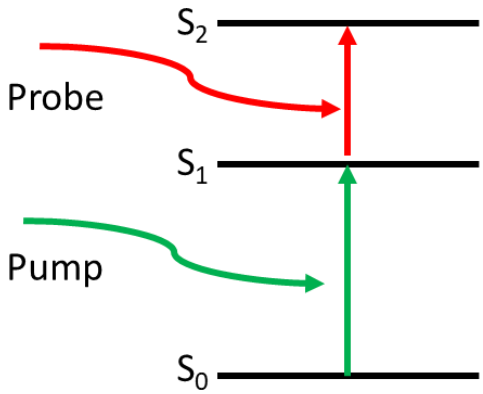

Figure 2-5: *Simplified energy diagram illustrating the influence of the pump and the probe on energy states.*

A typical measurement is done in two steps. The first measurement is done with the probe light on and records the impact of the pulsed laser on the sample. The second measurement is done with the probe light off to measure the base excited state at S_1, giving a final measured signal given in **Equation (2-3).**

$$\Delta OD(t) = Absorbance(With\ pump\ pulse) - Absorbance(Without\ pump\ pulse) \quad (2\text{-}3)$$

Due to the possibility of multiple transient species of different types of observables at the same wavelengths, multiple TAS measurements of different types are necessary to distinguish potential overlapping features. While a great variety of measurements are possible, the following were done in this study.

The first measurement relies on creating a spectrum of ΔOD against wavelength, constructed by taking multiple TAS measurements at different probe wavelengths and selecting a timescale to plot the spectrum. The spectrum is measured to identify the presence of possible transient features and how broad they are. This type of measurement can be done on multiple timescales to ascertain spectral evolution, further characterising observable features.

A second important set of measurements involves an excitation density dependent study of the decay dynamics. This is done to observe how the kinetics change with an increase in charge carrier density as well as an initial indication of the type of species present. For bimolecular recombination, according to the trapping model introduced in Chapter 1 Section 1.5, this measurement is often characterised by an energy density dependent fast phase followed by an energy density independent slow phase following the power law described by **Equation (2-5).** The fast phase would be assigned to the bimolecular recombination of charges generated when the charge carrier density exceeds the number of trap states available and thus a direct increase in energy density results in more charges observed up to a saturation point (limited by the total amount of available charges in the material). This fast phase is followed by a slow phase and represents the charge carriers escaping their traps. By this timescale the only charges present within the material are trapped and as the number of traps present in the material is independent of the energy density the amplitude in this phase is independent of the energy density. It is in this phase that the bimolecular recombination kinetics follow the power law previously described in Chapter 1 Section 1.5 and mentioned again below. This dual phase and energy density behaviour is a clear marker for bimolecular recombination and the reason for this second set of kinetic measurements.

A third set of measurements examines if the kinetics change when the sample is exposed to different gaseous environments. Kinetic measurements are first done in an inert gas, in the set-up used in this study the gas chosen was pure nitrogen. Following this, further measurements are done in an oxygen environment. Finally new measurements are done in the same inert gas used previously. The main objective of this set is to detect the presence of species such as polymer donor triplets that can

react with oxygen ground state triplet species, as well as observe if the material becomes degraded by the oxygen environment. A triplet-triplet reaction would result in a triplet species population depletion and thus a significant observable change in the kinetic trace. If all three traces (the before oxygen exposure, exposure to oxygen and post oxygen exposure measurements) are at a similar amplitude and trace behaviour then very few species reacting with oxygen triplets should be present in the material. Regarding this present study this is the desired outcome as the polarons of the materials of interest should not react with oxygen.

From the change in optical density from TAS measurements a variety of transient species can be observed. For the materials used in the studies in this thesis, the main transient species that can be observed with microsecond TAS are charge carriers and triplet states formed from excitation. Of note is that germinate recombination is generally a sub-microsecond process and thus will not appear significantly at the chosen timescales[7]. Key to TAS is the ability to measure charge carrier density from the change in optical density via **Equation (2-4)**.

$$n_{charge\ carrier} = \frac{N_A * \Delta OD}{1000 * \varepsilon_r * d}$$

(2-4)

with d the film thickness, N_A Avogadro's number, and ε_r the molar attenuation coefficient of the charges observed. In regards specifically to bimolecular recombination, the phenomenon has been characterised in certain material systems by I. Montanari, J. R. Durrant, C. Shuttle, J. Nelson and many others [7-13] as an observable kinetic power law, shown in **Equation (2-5)** and explained in more detail in Chapter **1** section **1.5**.

$$\Delta OD \propto t^{-\alpha}$$

(2-5)

with α an exponent and t the time. Beyond this initial characterisation of polaron trapping, the bimolecular recombination can be further characterised just from the charge carrier density thanks to **Equation (2-6)** and **(2-7)**[13, 14] based on modelling of pseudo first order electron recombination by P. R. F Barnes *et al.*

$$\frac{dn}{dt} = -\beta n^2$$

(2-6)

$$\tau = \frac{1}{\beta n} = n * (\frac{dn}{dt})^{-1}$$

(2-7)

with β the bimolecular recombination coefficient and τ the bimolecular recombination lifetime. As the charge carrier density can be found from equation **2.4,** both can be directly measured from TAS and allow characterisation of bimolecular recombination. Importantly the bimolecular recombination coefficient itself can be dependent on the charge carrier density of the form $\beta = \beta_0 n^{\eta}$. Most importantly the charge carrier density lifetime τas well as the alpha coefficient can be used to estimate the bimolecular recombination reaction order φ [15, 16] as described by **Equations (2-8)**-**(2-10)**.

$$\tau = \tau_0 n^{-\lambda}$$

(2-8)

$$\varphi_\tau = \lambda + 1$$

(2-9)

$$\varphi_\beta = \eta + 2$$

(2-10)

TAS therefore appears as a well-suited technique to characterise the bimolecular recombination process. Microsecond transient absorption spectroscopy measurements were done using a setup comprised of a 10 Hz (Quanta Ray) Nd:YAG Laser with 532 nm, 6 ns pulses. The output of this laser was directed towards an optical parametric amplifier to generate the tuneable pump pulse and excite the sample. The probe light was generated using an IL1 350-4000nm Halogen source (Bentham) tuned using bandpass filters, optical density filters, and longpass filters depending on the measurement. The transient data were collected using a Cornerstone 130 (Newport) monochromator to filter the signal, an optical transient pre-amplifier combined with an optical transient amplifier type PVOT0022 (Costronics) to amplify the filtered signal, and a MSO/DPO2000B oscilloscope (Tektronix) to record the measurements.

2.3 Computational methodology

To complement the above experimental methods several computational methods are used.

2.3.1 Density Functional Theory (DFT)

Density Functional Theory is a modelling technique that aims to describe the electronic structure of a molecule by solving an approximation of the Schrodinger equation. It allows very accurate calculations of fundamental physical properties on the molecular level. The theory was first established by Pierre Hohenberg and Walter Kohn in 1964 and is still widely used today[17]. In this study the general principles governing DFT are presented as a bird's eye view, serving as an overview of the governing principles behind DFT. A complete derivation of the theory can be found in a complete guide by Robert Parr and Weitao Yang [18].

The essential starting point is the time independent Schrodinger equation. This equation is under normal circumstances very time consuming to solve for systems beyond single atom systems due to the complex and even sometimes unknown nature of the potential energy term.

A first step to allow easier solving of this equation lies in the Born-Oppenheimer approximation[19] giving a simplified form to the Schrodinger equation given in **Equation (2-11)** for a many body coulombic system.

$$\left(\hat{U} + \hat{T} + \hat{V}\right)\psi(\vec{\boldsymbol{r}}) = E\psi(\vec{\boldsymbol{r}})$$

(2-11)

with $\hat{U}$ the coulombic interaction of the system, $\hat{T}$ the kinetics energy term, $\hat{V}$ the potential energy term, ψ the wavefunction of the system, E the total energy and $\vec{\boldsymbol{r}}$ the three-dimensional position vector for the particles in the system. A consequence of this simplification allows $\hat{V}$ to be described as seen in **Equation (2-12)**

$$\hat{V} = \sum_i v(\boldsymbol{r_i})$$

(2-12)

with $v(\boldsymbol{r})$ the potential energy at position $\boldsymbol{r}$. The basis of this simplification lies on the assumption that the energy of the system can be seen as a sum of different terms such as the electronic, vibrational, rotational and nuclear spin terms for a molecular system. Very importantly under this paradigm the particle density $n(\mathbf{r})$ can be found and defined as the probability of finding an Nth electron at a position $\boldsymbol{r}$ as described by **Equation (2-13).**

$$n(\mathbf{r}) = N \int d^3 r_2 \int d^3 r_3 \dots \int d^3 r_N \, \psi^*(\boldsymbol{r_1}, \boldsymbol{r_1}, \dots, \boldsymbol{r_N}) \psi(\boldsymbol{r_1}, \boldsymbol{r_1}, \dots, \boldsymbol{r_N})$$

(2-13)

The principal methodology on which DFT operates is to guess the particle density $n(\mathbf{r})$, find an approximate wavefunction $\psi(\boldsymbol{r_1}, \boldsymbol{r_1}, \dots, \boldsymbol{r_N})$ corresponding to this particle density, and calculate the potential $v(\mathbf{r})$ by solving the approximated Schrodinger equation. Key to this is the Hohenberg-Kohn theorem which postulates that it is possible to calculate the ground state wavefunction $\psi_0(\boldsymbol{r_1}, \boldsymbol{r_1}, \dots, \boldsymbol{r_N})$ given a ground state density $n_0(\mathbf{r})$. This stems from writing the wavefunction ψ as a functional of $n(\mathbf{r})$ and considering the ground state wavefunction as described by **Equation (2-14).**

$$\psi_0(\boldsymbol{r_1}, \boldsymbol{r_1}, \dots, \boldsymbol{r_N}) = \psi[n_0(\mathbf{r})]$$

(2-14)

Consequently, the energy of the ground state is also a functional of $n_0(\mathbf{r})$ and due to the variation principle follows that the energy follows

$$E(n_0) \leq E(n')$$

(2-15)

with n' a non-ground state density. Thus, by minimising the energy one can compute or at least find a reasonable approximation of, the ground state energy and therefore other properties of the system.

When directly applying this methodology of minimising the energy functional several complications arise[20, 21] due to an oversimplification of potentials, and not considering the spin in the overall energy terms. To palliate these complications Kohn and Sham developed[22] an indirect minimisation method based on the use of particle

orbitals as well as an energy term named energy exchange-correlation term or E_{xc} ,and as a result the energy functional defined by **Equation (2-16)**.

$$E(n) = T(n) + U(n) + V(n) = T_s(n) + U_H(n) + E_{xc}(n) + V(n)$$

(2-16)

with $T_s(n)$ the kinetic energy of noninteracting particles, $U_H(n)$ the Hartree energy and $E_{xc}(n)$ the exchange-correlation energy, which groups the most difficult terms to calculate or define into one single term. The main reason for such a simplification comes from the observation that $E_{xc}(n)$ is typically much smaller than the other terms and thus can be approximated without major consequences. From this simplification one can define an external potential $v_s(\boldsymbol{r})$

$$v_s(\boldsymbol{r}) = v(\boldsymbol{r}) + v_H(\boldsymbol{r}) + v_{xc}(\boldsymbol{r})$$

(2-17)

with $v_H(\boldsymbol{r})$ the Hartree potential, $v_{xc}(\boldsymbol{r})$ the exchange-correlation potential. Thus a many-body system with potential $v(\boldsymbol{r})$ and following **Equation (2-11)** can be calculated by solving the equations pertaining to a single-body system that follows **Equation (2-18).**

$$\left[-\frac{\hbar^2\nabla^2}{2m} + v_s(\boldsymbol{r})\right]\Phi_i(\boldsymbol{r}) = \epsilon_i\Phi_i(\boldsymbol{r})$$

(2-18)

with $\Phi_i(\boldsymbol{r})$ single-particles orbitals of this non interacting system. The solution to this Schrödinger equation yields orbitals that reproduce the density $n(\mathbf{r})$ of the greater system based on **Equation (2-19)**

$$n(\boldsymbol{r}) \equiv n_s(\boldsymbol{r}) = \sum_i^N f_i|\Phi_i(\boldsymbol{r})|^2$$

(2-19)

where $f_i$is the occupation of the ith orbital. Thus, the energy minimisation of $E(n)$ can be replaced with solving **Equation (2-18)**. Equations **(2-16)** to **(2-19)** are referred to as the Kohn-Sham equations and lead to the final and actual workflow of DFT as summarised by ***Figure 2-6*** .

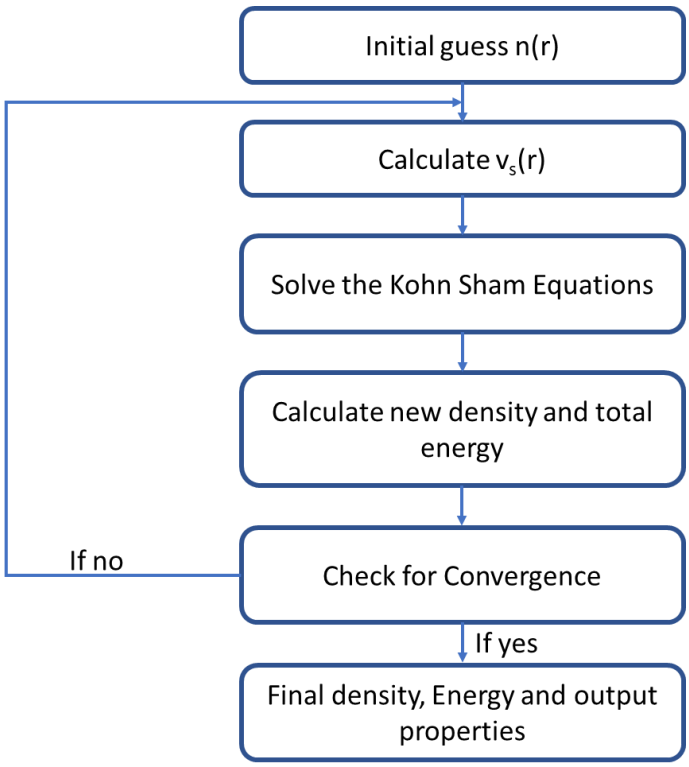

Figure 2-6: *Diagram summarising the workflow of a typical DFT calculation*

One of the main considerations in DFT simulations lies in the approximations of the exchange correlation potential term $v_{xc}(\boldsymbol{r})$, of which many were conceived and found applicable to different systems[23-25]. While going through the different approximations is beyond the scope of this study, it remains an ongoing topic of research. It is important to note that DFT as described can only be used to calculate the ground state of the molecular system. In order to accurately model the excited state of the molecular system DFT has to be extended to the time dependant version (TDDFT), detailed in Chapter **5** section **5.1.2.** Within this study the ORCA software was primarily used for calculations as seen in Chapter **5** and Chapter **6.**

2.3.2 Molecular Dynamics (MD)

In comparison with DFT, molecular dynamics aim to characterise larger systems using classical mechanics. This technique was conceptualised as early as the 18th century but was only able to be implemented on large scale complex systems in the 1950s, with the first fluid MD simulation done by Berni Alder and Tom Wainwright[26]. The key principle lies in the use of Newton's equations of motion to evaluate forces acting on the system and adjusting the coordinates and trajectory of the system accordingly. This principle allows the calculation of physical properties such as velocity and

position at a given time, which can then be used for additional calculation steps, further updating the system, with a possible end goal being the convergence of the energy of the system to its relaxed state. The standard workflow of a MD simulation is given in ***Figure 2-7***.

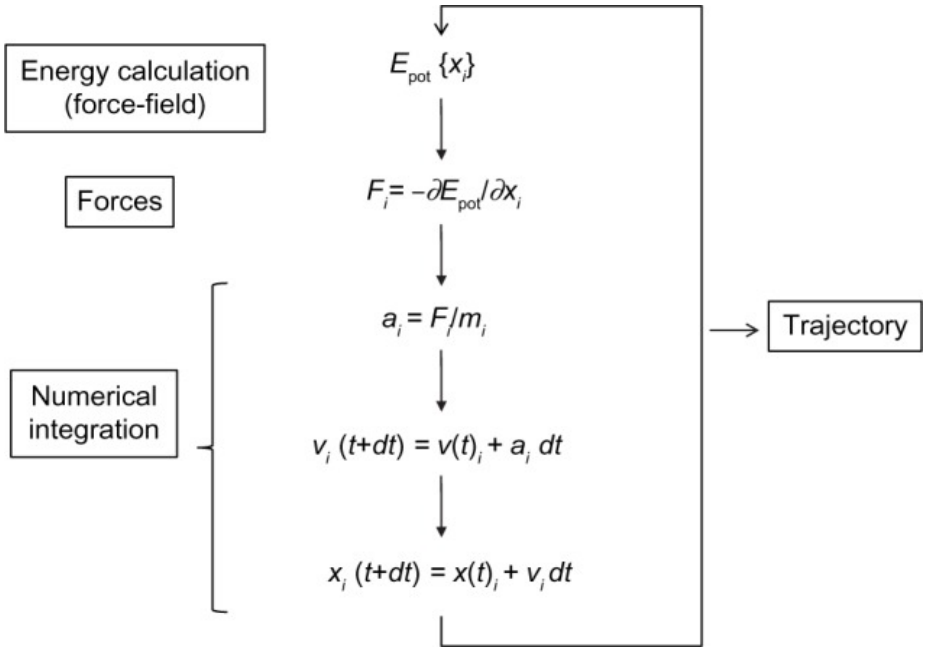

Figure 2-7*: Diagram summarising the workflow of a typical molecular dynamics simulation in a system comprised of i atoms at positions X_i with acceleration a, velocity v and at time t. Figure taken from [27]*

The underlying difficulty of MD and what has led to many challenges from its initial theoretical underpinning lies in the choice of potential forcefield which will define how the energy is calculated. The development of force fields to accurately describe systems and molecules has been the subject of much study since their inception in the 1960s [28-31], the complexity of which is not the subject of the study. The main use of molecular dynamics and its use within this study lies in its ability to find the relaxed state of a large complex system which would be impractical to calculate using DFT. Within this study the GROMACS software is used.

2.3.3 Kinetic Monte Carlo (KMC)

The final core computational method relevant to this study lies in Kinetic Monte Carlo. This methodology relies on modelling how a system with different configurations evolves over time using probability calculations[32]. The central

equation to be solved is described in **Equation (2-20).** which describes the change in the probability $P_\alpha(t)$ of the system to be in the state α at time **t**.

$$\frac{dP_\alpha}{dt} = \sum_{\alpha \neq \beta} k_{\beta\alpha} P_\beta(\boldsymbol{t}) - \sum_{\alpha \neq \beta} k_{\alpha\beta} P_\alpha(\boldsymbol{t})$$

(2-20)

With β any system configuration other than α, $k_{\beta\alpha}$ and $k_{\alpha\beta}$ the rate constants for the transition from configuration β to configuration α and vice versa. This equation is time consuming to solve for even simple systems and unfeasible for larger more complex systems. Most notably the main difficulty lies in finding the rate constants for the entire system. While several KMC methods to solve this equation exist for different types of simulations, the most widely used algorithm follows the Bortz-Kalos-Lebowitz (BLK) method developed by A. B. Bortz, M. H. Kalos and J. L Lebowitz[33], as summarised by ***Figure 2-8***. which aims to solve the equation by advancing the internal clock of the system by a random number ρ_2 and executing a selection of possible process based on a random number ρ_1.

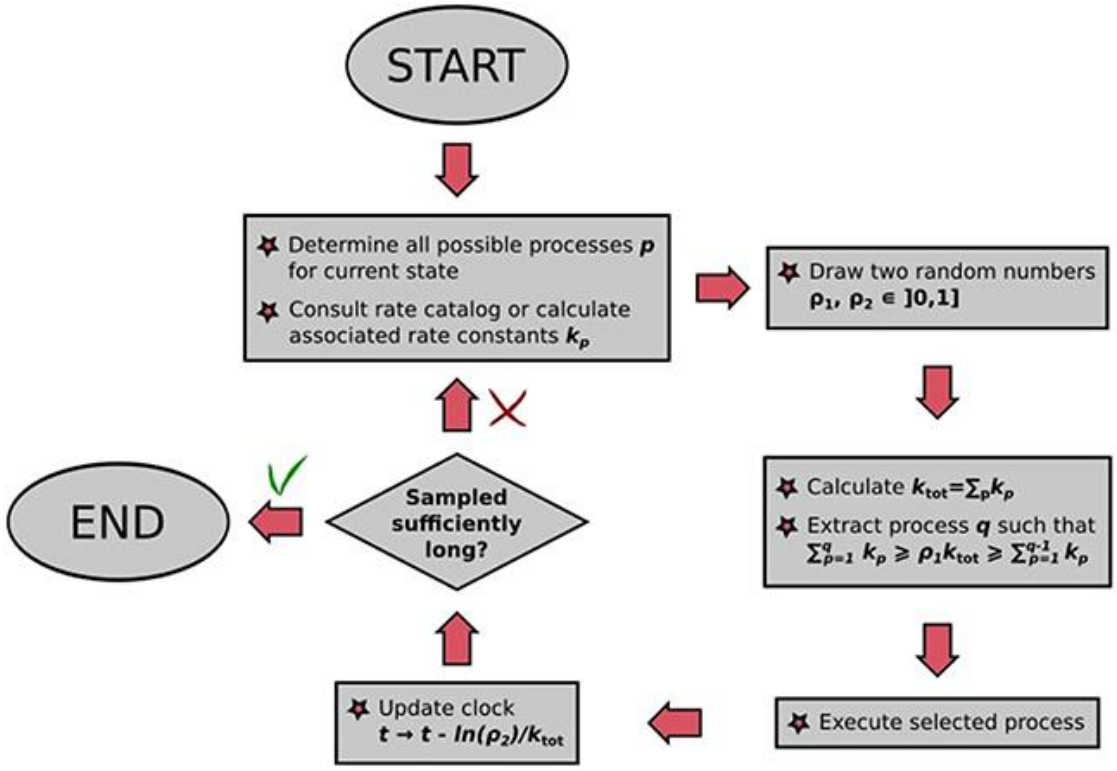

***Figure 2-8**: Diagram summarising the workflow of a BLK algorithm taken from [32]*

This methodology with universal application is often used in OPV simulation to model the movement of charges within a system based on the transition rates of a

charge carrier going from a ground state to excited state. Within the context of this study an individual dedicated KMC software was not used but instead implemented as part of the VOTCA software, the central focus of Chapter **5**.

2.4 Thesis plan

2.4.1 Objectives

The main objective of this study lies in providing insight into the bimolecular recombination process by studying a donor polymer exhibiting unusual properties in ZZ115. More specifically this study is divided into two separate sections. The first section used experimental techniques to study factors that could influence bimolecular recombination in the non-Langevin polymer ZZ115. A second section used computational methods to, in a first step, provide insight into the intrinsic properties of ZZ115 which could lead to the reported unusual properties of this polymer and, in a second step, provide insight into the reported observations of the experimental section.

2.4.2 Workflow

Having established the objectives of this study and the tools available, the following plan was chosen to accomplish said objective. First and foremost a thin film of the OPV material of interest is characterised at the ground state using UV-VIS. This allowed a better understanding of the system, provided a basis of comparison for other studies done on the same material, and an important step for transient techniques. Once this baseline has been established, transient techniques were used to characterise the bimolecular recombination process directly or indirectly within the confines of the chosen material. These measurements were first done on the pristine material and then in typical device-optimised blends. Then measurements were done on blend films with a varying acceptor concentration. Additional measurements were done by collaborators when additional insight was required or for characterisation techniques not available.

Following this experimental section, a computational analysis was performed in order to complement experimental results. This analysis was done by first modelling the

previously chosen material system at a fundamental molecular level. Then a larger system more relevant to the studied film was modelled until finally a comprehensive model allowed a direct comparison with experimental findings. Thus, a more complete picture could be established in order to fulfil the desired objectives. A summary of this workflow is seen in ***Figure 2-9***.

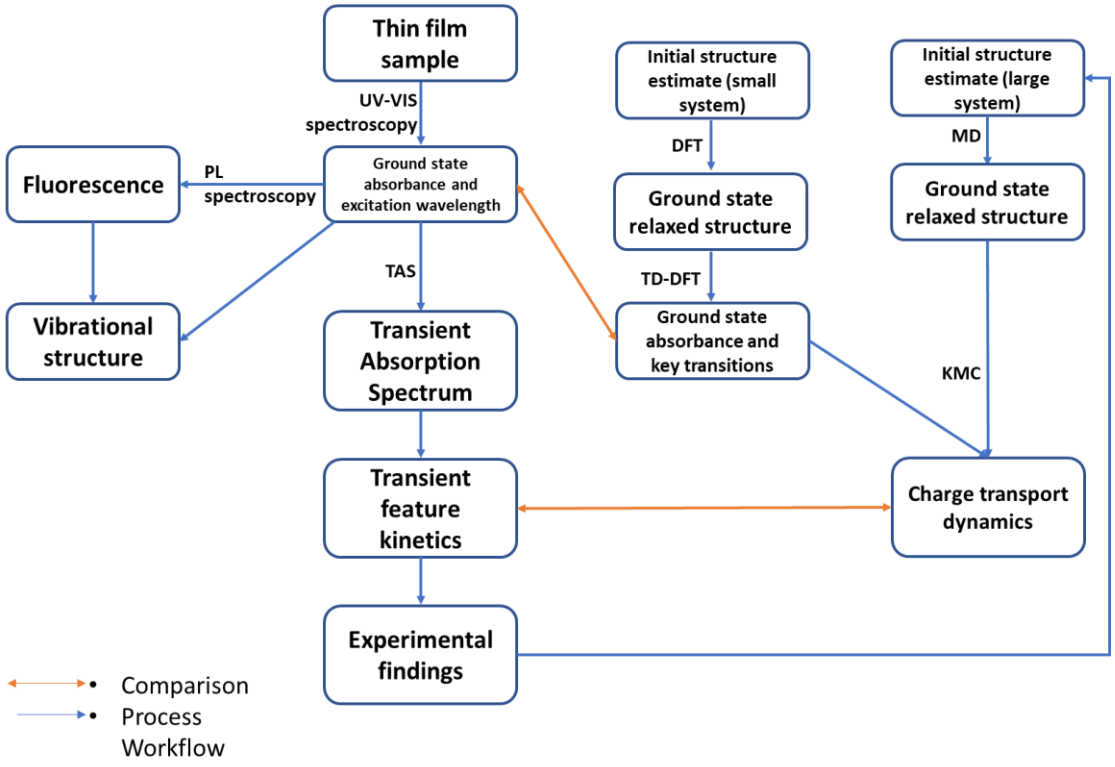

Figure 2-9*:Diagram summarising the overall workflow of this thesis*

2.5 References

1. T. G. Mayerhofer, S. Pahlow, and J. Popp, *The Bouguer-Beer-Lambert Law: Shining Light on the Obscure.* ChemPhysChem, 2020. **21**(18).
2. Stokes, G., *On the change in Refrangibility of Light.* Philosophical Transactions of the Royal Society of London, 1852. **142**.
3. O. V. Mikhnenko, P. W. M. Blom, and T.-Q. Nguyen, *Exciton diffusion in organic semiconductors.* Energy and Environmental Science, 2015(7).
4. C. J. Brabec, G. Zerza, G. Cerullo, S. De Silvestri, S. Luzzati, J. C. Hummelen, and N. S. Sariciftci, *Tracing photoinduced electron transfer process in conjugated polymer/fullerene bulkheterojunctions in real time.* Chemical Physics Letters, 2001.

5. O. V. Mikhenko, F. Cordella, A. B. Sieval, J. C. Hummelen, P. W. M. Blom, and M. A. Loi, *Exciton Quenching Close to Polymer–Vacuum Interface of Spin-Coated Films of Poly(p-phenylenevinylene) Derivative.* The Journal of Physical Chemistry B, 2009. **113**(27).
6. A. Erbe, S. Nayak, Y.-H. Chen, F. Niu, M. Pander, S. Tecklenburg, and C. Toparli, *How to Probe Structure, Kinetics, and Dynamics at Complex Interfaces In Situ and Operando by Optical Spectroscopy,*, in *Encyclopedia of Interfacial Chemistry*. 2018, Elsevier. p. 199-2019.
7. H. Ohkita, S. Cook, Y. Astuti, W. Duffy, S. Tierney, W. Zhang, . . . J.R. Durrant, *Charge Carrier Formation in Polythiophene/Fullerene Blend Films Studied by Transient Absorption Spectroscopy.* Journal of the American Chemical Society, 2008. **130**(10).
8. J. Nelson, *Diffusion recombination in polymer-fullerene blends and its influence on photocurrent collection.* Physical Review B, 2003. **67**(15).
9. I. Montanari, A. F. Nogueira, J. Nelson, J. R. Durrant, C. Winder, M. A. Loi, . . . C. Brabec, *Transient optical studies of charge recombination dynamics in a polymer/fullerene composite at room temperature.* Applied Physics Letters, 2002. **81**(16).
10. A. F. Nogueira, I. Montanari, J. Nelson, J. R. Durrant, C. Winder, N. S. Sariciftci, and C. Brabec, *Charge Recombination in Conjugated Polymer/Fullerene Blended Films Studied by Transient Absorption Spectroscopy.* J. Phys. Chem. B, 2003. **107**.
11. C. G. Shuttle, B. O'Regan, A. M. Ballantyne, J. Nelson, D. D. C. Bradley, and J.R. Durrant, *Bimolecular recombination losses in polythiophene: Fullerene solar cells.* Physical Review B, 2008.
12. T. M. Clarke, F. C. Jamieson, and J.R. Durrant, *Transient Absorption Studies of Bimolecular Recombination Dynamics in Polythiophene/Fullerene Blend Films.* J. Phys. Chem. C., 2009. **113**(49): p. 20934–20941.
13. T. M. Clarke, C. Lungenschmied, J. Peet, N. Drolet, and A. .J. Mozer, *A Comparison of Five Experimental Techniques to Measure Charge Carrier*

Lifetime in Polymer/Fullerene Solar Cells. Advanced Energy Materials, 2014. **5**(4).

14. P. R. F. Barnes, K. Miettunen, X. Li, A. Y. Anderson, T. Bessho, M. Gratzel, and B.C. O'Regan, *Interpretation of Optoelectronic Transient and Charge Extraction Measurements in Dye-Sensitized Solar Cells.* Advanced Materials, 2013. **25**(13).
15. A. Maurano, R. Hamilton, C. G. Shuttle, A. M. Ballantyne, J. Nelson, B. O'Regan, . . . J. R. Durrant, *Recombination Dynamics as a Key Determinant of Open Circuit Voltage in Organic Bulk Heterojunction Solar Cells: A Comparison of Four Different Donor Polymers.* Advanced Materials, 2010. **22**(44).
16. C. G. Shuttle, B. O'Regan, A. M. Ballantyne, J. Nelson, D. D. C. Bradley, J. de Mello, and J. R. Durrant, *Experimental determination of the rate law for charge carrier decay in a polythiophene: Fullerene solar cell.* Applied Physics Letters, 2008. **92**(9).
17. P. Hohenberg and W. Kohn, *Inhomogeneous Electron Gas.* American Physics society, 1964.
18. R. G. Parr and Y. Weitao, *Density-Functional Theory of Atoms and Molecules*. 1995, Oxford: Oxford Science Publications.
19. M. Born and R. Oppenheimer, *Zur Quantentheorie der Molekeln.* Annalen der Physik, 1927. **389**(20).
20. J. P. Perdew and M. Levy, *Extrema of the density functional for the energy: Excited states from the ground-state theory.* Physical Review B, 1985. **31**(10).
21. K. Capelle and G. Vignale, *Nonuniqueness of the Potentials of Spin-Density-Functional Theory.* Physical Review Letters, 2001. **86**(24).
22. W. Kohn and L. J. Sham, *Self-Consistent Equations Including Exchange and Correlation Effects.* Physical Review Journals, 1965. **140**(4A).
23. J. P. Perdew and W. Yue, *Accurate and simple density functional for the electronic exchange energy: Generalized gradient approximation.* Physical Review B, 1986. **33**(12).

24. Y.-H. Kim, I.-H. Lee, S. Nagaraja, R. J.-P, R. Q. Hood, and R.M. MArtin, *Two-dimensional limit of exchange-correlation energy functional approximations.* Physical Review B, 2000. **61**(8).

25. S. H. Vosko, L. Wilk, and M. Nusair, *Accurate spin-dependent electron liquid correlation energies for local spin density calculations: a critical analysis.* Canadian Journal of Physics, 1980. **58**(8).

26. B. J. Alder and T. E. Wainwright, *Phase Transition for a Hard Sphere System.* Journal of Chemical Physics, 1957. **27**(5).

27. A. Hospital, J. R. Goñi, M. Orozco, and J.L. Gelpí, *Molecular dynamics simulations: advances and applications.* Adv Appl Bioinform Chem, 2015. **8**: p. 37–47.

28. A. Gavezzotti, *Molecular Aggregation: Structure analysis and molecular simulation of crystals and liquids*. Monographs on crystallography. 2006: Oxford Univeristy Press.

29. N. L. Allinger, Y. H. Yuh, and H. J., Lii, *Molecular mechanics. The MM3 force field for hydrocarbons.* Journal of the American Chemical Society, 1989. **111**(23).

30. A. K. Rappe, C. J. Casewit, K. S. Colwell, W. A. Goddard III, and W.M. Skiff, *UFF, a full periodic table force field for molecular mechanics and molecular dynamics simulations.* Journal of the American Chemical Society, 1992. **114**.

31. W. L. Jorgensen, D. S. Maxwell, and J. Tirado-Rives, *Development and Testing of the OPLS All-Atom Force Field on Conformational Energetics and Properties of Organic Liquids.* Journal of the American Chemical Society, 1996. **118**.

32. M. Andersen, C. Panosetti, and K. Reuter, *A Practical Guide to Surface Kinetic Monte Carlo Simulations.* Frontiers in Chemistry, 2019.

33. A. B. Bortz, M.H.Kalos, and J.L. Lebowitz, *A new algorithm for Monte Carlo simulation of Ising spin systems.* Journal of Computational Physics, 1975. **17**(1).

Chapter 3: Transient Features in ZZ115-fullerene based films

3.1 Introduction and Methodology

This chapter aims to provide an initial characterisation of the ZZ115 polymer. A very first study focused on specific characterisation of the donor molecule ZZ115 that has shown very unusual properties, even beyond a non-Langevin behaviour as described in Chapter **1** Section **1.5.** To do so blend films were prepared with typical fullerene acceptors in $PC_{60}BM$ and $PC_{70}BM$.

3.1.1 $PC_{60}BM$ and $PC_{70}BM$

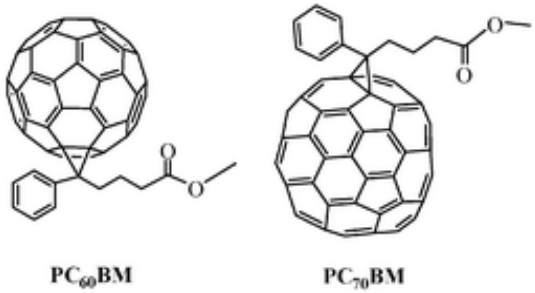

Figure 3-1: *Molecular structure of $PC_{60}BM$ and $PC_{70}BM$.*

The acceptor molecule $PC_{60}BM$ was first synthesised as a variant of C_{60} derivatives[1]. C_{60} derivatives are and have been used in organic photovoltaics since the 1990s for their HOMO and LUMO level and high electron mobility[2] allowing better device performances. The main draw of $PC_{60}BM$ compared to some of its fullerene peers is its solubility in chlorobenzene and other important solvents. This allows an easier and cheaper synthesis of BHJ cells in addition to better device performances. The acceptor molecule $PC_{70}BM$ is very similar except based on C_{70} instead of C_{60}. The reduced symmetry in C70 was found to lead to higher absorption cross-sections across the entire spectrum[3], thus in turn often leading to higher efficiencies. It however has a lower electron mobility compared to $PC_{60}BM$ due to its larger size[4]. Both fullerene acceptors are still widely used today even if not as ubiquitous as previously due to their stability[5] issues. In recent years fullerenes have been in decline compared to non-fullerene acceptors as efficiencies have risen[6]. Even so fullerenes are part of this chapter's study due to how well and comprehensively studied they are. In addition, fullerenes are easy to experimentally characterise and hence are very suitable candidates to obtain a better understanding of the bimolecular recombination process.

3.1.2 Measurement methodology

ZZ115 base samples were measured in the following way. Firstly, samples were prepared as described below. These samples were measured using UV-VIS in order to obtain the ideal excitation wavelength necessary for the other experimental techniques. This excitation wavelength is then used for PL measurements conducted as described in Chapter **2** Section **2.2.2** and for TAS measurements conducted as described in Chapter **2** Section **2.2.3.**

3.1.3 Sample preparation

Samples were prepared the following way. Solutions of ZZ115, wherever pristine or with the desired acceptor ($PC_{60}BM$ or $PC_{70}BM$) at the 1:2 ratio were diluted in a chlorobenzene (PhCl) solution for an initial solution at 20 mg/ml. The solutions were stored overnight in a nitrogen glovebox on a hot plate heated at 65 °C with a stirrer rotating at 500 RPM. 30 µL of these solutions were then deposited on a 1 cm x1 cm glass substrate to be spin coated. The glass substrates, all single use, are cleaned beforehand with chloroform and the back of the samples are cleaned after spin coating similarly. The spin coating conditions for all the different samples as well as the exact sample preparation details are summarized in the appendix under **Table A-1**. The aim of these sample preparation parameters is to produce samples with a peak absorbance of around 0.4 to 0.5. This allows a large enough signal for proper TAS measurements without overloading the detector.

3.2. Results

3.2.1 Study of pristine ZZ115

To start this experimental study, experiments were carried out on a pristine ZZ115 sample to serve as a control case as well as providing a proper comparison with previous studies. As outlined in the general methodology, UV-VIS spectroscopy is a commonly used technique to measure the ground state absorbance and when combined with PL spectroscopy, allows a good general characterisation of the ground

state of the material. Thus, ZZ115 was characterised using UV-VIS and PL measurements as shown by ***Figure 3-2***.

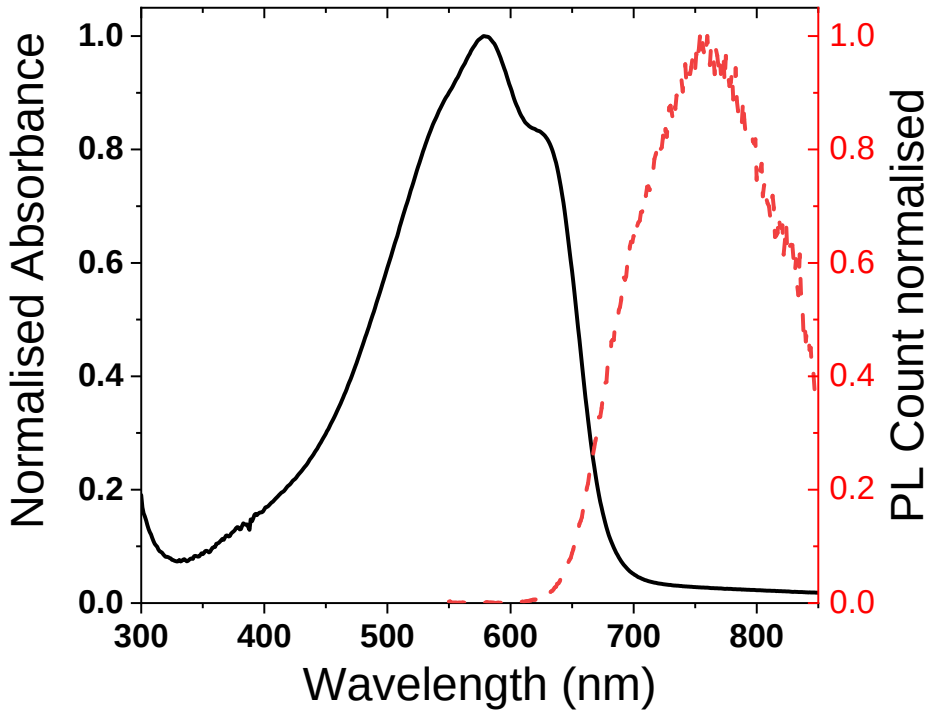

Figure 3-2: *Ground state absorbance spectrum of pristine ZZ115 (black solid line) and PL spectrum of pristine ZZ115 (dashed line). Pl measurements were done with a 500 nm excitation wavelength*

From the absorbance spectrum presented in ***Figure 3-2***, ZZ115 shows a double feature present at the 580 nm and 630 nm wavelengths in addition to a small shoulder present at 520 nm, all features in the visible region. The highest wavelength feature lies at 630 nm, therefore is the lowest energy, and can be assigned to the 0-0 peak of ZZ115. Conversely the 580 nm peak can be assigned to the 0-1 peak and the 520 nm shoulder the 0-2 peak. The spectrum in ***Figure 3-2*** is slightly different from other publications, which show clear distinct double features of the 0-0 and 0-1 peak[7], while the present material only shows a diminished 0-0 peak (but otherwise almost an identical spectrum). This may be due to a lower molecular weight compared to the aforementioned study, resulting in a shifted or reduced peak[8] as a result of increased disorder within the film[9]. This difference should not be significant however as excitation wavelengths used in past studies and this present study were below 550 nm and therefore it is the 0-2 and 0-1 peaks that are primarily excited.

The ZZ115 PL spectrum on the other hand shows a major peak at 750 nm with two faint shoulders at the 690 nm wavelength and 830 nm wavelength, which can be assigned as the 0-0 peak at 690nm, 0-1 peak at 750nm and 0-2 peak at 830 nm. The Stokes Shift would be placed at 0.17 eV, noticeably larger than the stokes shift of P3HT[10] of 0.07 eV. ZZ115 therefore appears to have a more complicated vibrational relaxation pathway than P3HT even with both reporting non-Langevin behaviour. Therefore, as described in Chapter **2** Section **2.2.3**, TAS measurements should find a negative signal from 400 nm to close to 700 nm, corresponding to the ground state bleach, as well as a dampened signal in the 700 to 800 nm region due to fluorescence. From these measurements the excitation wavelength used for TAS measurements was chosen at 500 nm wavelength. This value was used due to the 500 nm wavelength being part of the central 580 nm peak while not being at the peak maximum allowing better control during sample preparation to obtain an absorbance of 0.4-0.5 for subsequent measurements. While this is different from the other studies that used instead a 532 nm excitation wavelength[11], the difference was not deemed significant enough that the results would be affected (see ***Figure A-1*** in the appendix). Thicker samples, identifiable by larger absorbance values could lead to increased inhomogeneity and thus increased results variation, hence the aim to synthesize samples with an absorbance of 0.5 at the 500 nm wavelength. With this excitation wavelength of 500 nm, a transient absorption spectrum was measured.

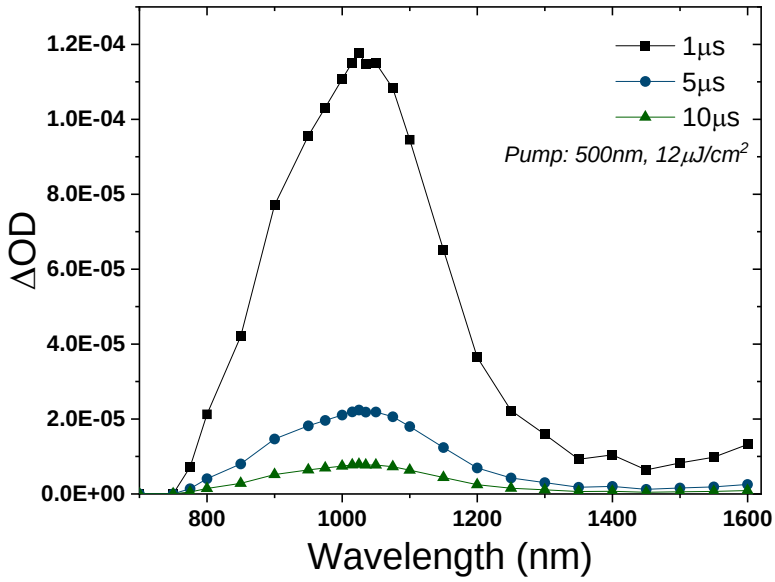

Figure 3-3*:Transient absorption spectrum of pristine ZZ115 at 1 μs, 5 μs and 10 μs timescale. Measurements were taken at 500nm excitation wavelength and with a 12 uJ/cm² excitation energy density.*

As shown in ***Figure 3-3***, the transient absorption spectrum of ZZ115 film is characterised by a broad absorption peak centred on the 1030 nm wavelength, with possibly a small shoulder around the 950 nm wavelength. Notably the spectrum reaches $\Delta OD = 0$ at the 750 nm wavelength before ZZ115 starts absorbing in the ground state as seen in ***Figure 3-2***. These above observations are maintained at longer timescales. A possibility exists of the fluorescence masking the TAS signal in the 700 nm - 800 nm region. However previous studies have shown a 97% PL quenching with the addition of fullerene and no new features in this wavelength region[7, 12], so it is unlikely (though not impossible) that a major feature is present in the 700 nm-800 nm wavelength in the pristine. To correctly identify the species, present at the 1000 nm - 1100 nm wavelength, the 1100 nm probe wavelength was measured kinetically. Firstly, measurements with a variation excitation energy density were carried out.

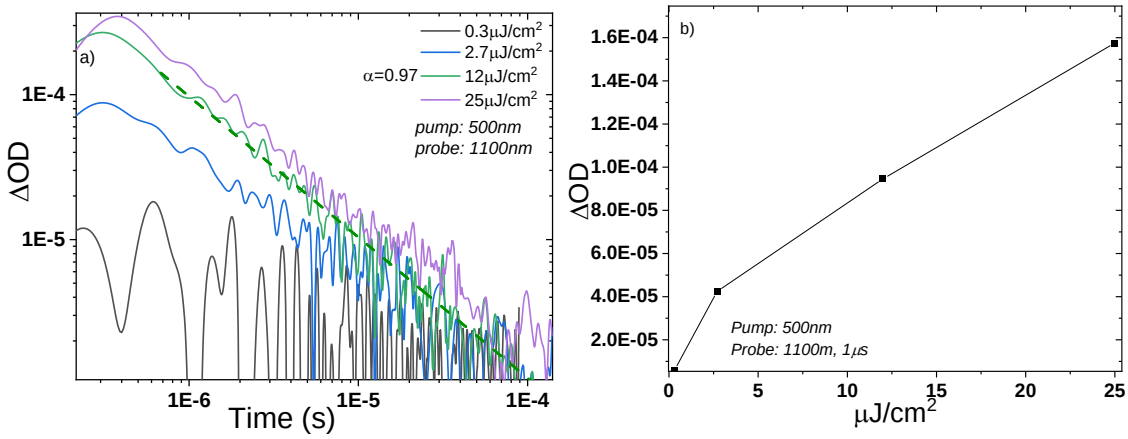

Figure 3-4: a) *Transient absorption kinetics for pristine ZZ115 film measured at different energy densities with a pump wavelength of 500nm and a probe wavelength of 1100nm.* ***b)*** *Energy saturation plot of the measured signal at 1μs against excitation energy density.*

As described in the model of bimolecular recombination in Chapter **1** section **1.5** and the description of TAS in Chapter **2** section **2.2.3**, the kinetics in ***Figure 3-4a*** show a power law characteristic of trap-based recombination. While the 0.3 uJ/cm^2 curve, seen as the black line**,** appears to show a close to flat line for a significant portion, at least until around 3 μs, the signal is small enough that this could be simply due to experimental error. The other curves starting with the 2.7 μJ/cm^2 curve in blue show a power law with an α coefficient of around 1. The fitted α value of close to 1 reflects a close to pure bimolecular recombination process occurring in pristine ZZ115. Therefore, the band at 1100 nm should correspond to the ZZ115 polaron undergoing unimpeded bimolecular recombination. The lack of mono exponential section in the curve suggests a lack of triplet species. This is confirmed by a study showing the ZZ115 triplet at 950 nm [13] and the later oxygen independence measured best illustrated in ***Figure 3-7***. Additionally, an examination of energy density evolution shows saturation would occur by 20 μJ/cm^2, where further excitation would not lead to more charges recombining.

Bimolecular recombination found on the pristine ZZ115 is not an unusual result even with no acceptor. Other materials have been found to be able to bimolecularly recombine with no acceptor[14, 15] but the amount of charges recombining as evidenced by the high measured signal is highly unusual. It is expected for a lone donor-based sample to produce some charges, potentially just triplets, upon excitation

which would then undergo geminate recombination due to a lack of energetic drive to separate into free carriers. Instead, it appears ZZ115 generates a great number of charges which do not all undergo geminate recombination and instead bimolecularly recombine. It is also possible that geminate recombination occurs at earlier timescales. Thus further investigation is necessary.

These results represent the base donor system, a system which will serve as a comparison for the blend ratio systems, systems more appropriate for OPV usage. Firstly, a very commonly acceptor used was added in $PC_{60}BM$, and the properties were studied.

3.2.2 Study of ZZ115 mixed with $PC_{60}BM$

The 1:2 blend ratio was chosen for ZZ115:$PC_{60}BM$ measurements as it is found to be the ideal ratio for device performance[12]. The 1:2 blend was measured first using UVVIS and PL to ascertain the ground state absorbance of the different samples.

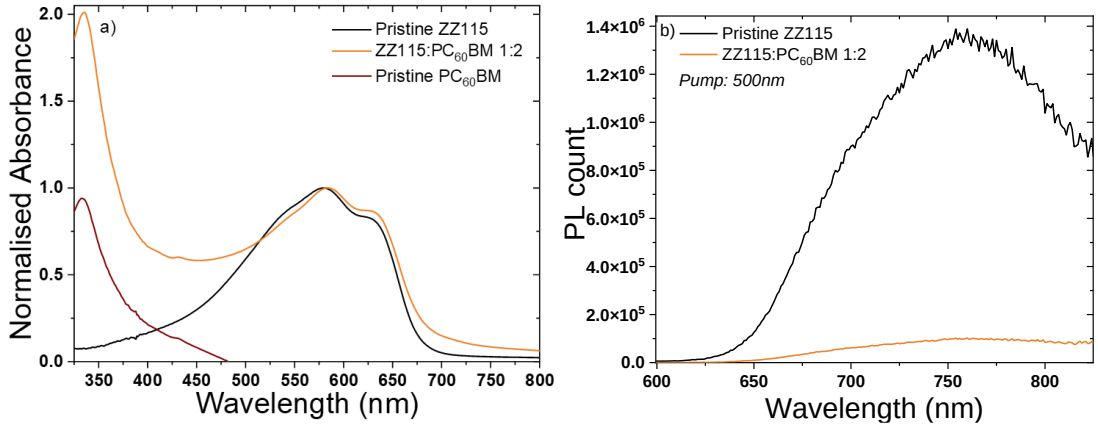

Figure 3-5: a) *Normalised ground state absorbance spectra of ZZ115:$PC_{60}BM$ samples at the 1:2 blend ratio, pristine $PC_{60}BM$ and pristine ZZ115. The spectrum is normalised to the 580nm peak.* ***b)*** *photoluminescence spectrum of ZZ115:$PC_{60}BM$ at the 1:2 blend ratio and pristine ZZ115. The excitation wavelength used was 500nm.*

In comparison with the pristine ZZ115, the addition of fullerene to ZZ115 leads to the formation of a peak at 350 nm as seen in ***Figure 3-5a***. This is consistent with previous findings showing $PC_{60}BM$ having a ground state absorption feature mainly in the 300-350 nm region[3]. The rest of the spectrum is well maintained following the addition of the fullerene with the blend system having the same two features at 580 nm and 630 nm wavelengths in addition to the small shoulder present at 520 nm. The pristine $PC_{60}BM$ confirms the 350 nm feature in the blend to be $PC_{60}BM$ based,

most likely the 0-0 peak. The lack of major change in the ZZ115 features does show $PC_{60}BM$ having no effect on the ZZ115 transitions and therefore no major morphological changes in the ZZ115 regions. In contrast the PL spectrum sees a 95% exciton quenching upon addition of $PC_{60}BM$, though each of the pristine ZZ115 PL features remain through exciton quenching. This quenching highlights a change in the electronic relaxation mechanism, most likely due to the speed of exciton relaxation greatly increasing. From ***Figure 3-5***, just like the pristine sample, an excitation wavelength of 500 nm was used for consistency between the pristine and the blend samples. The different excitation wavelengths were still compared to ascertain potential deviations observed in the results.

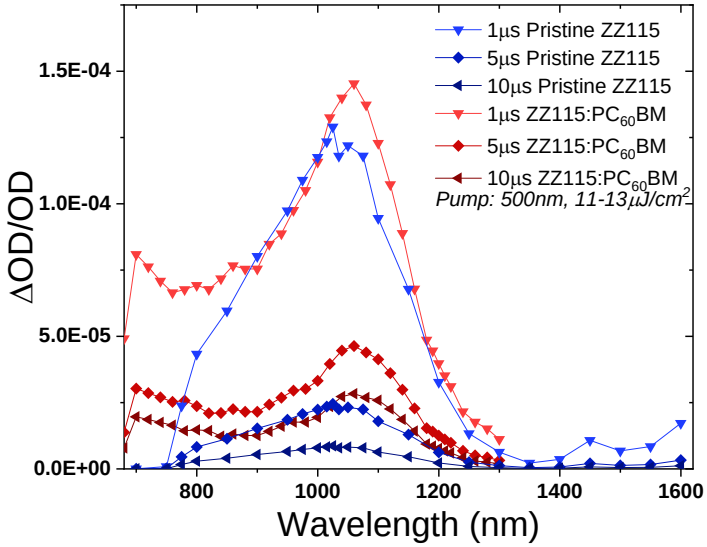

Figure 3-6*: Transient absorption spectra of ZZ115 pristine and ZZ115:$PC_{60}BM$ samples at a (1:2) blend ratio at 1 µs, 5 µs and 10 µs timescale. Measurements were taken at 500nm excitation wavelengths and with an 11-13uJ/cm2 excitation energy density. The spectrum is adjusted for photons absorbed.*

Adding an acceptor for ZZ115 leads to significant changes in the TA spectrum. As seen in ***Figure 3-6***, addition of the fullerene acceptor maintains the ZZ115 polaron peak from the pristine ZZ115 sample however, a noticeable shift from a 1025 nm maximum to a 1050 nm peak maximum occurs while the width of the peak decreases with the addition of the fullerene. This shift is accentuated at longer timescales as evidenced by the traces at the 5 µs timescale. Conversely the decay in signal is reduced for the blend when compared to the pristine showing a significant change in recombination kinetics upon introduction of fullerene. The higher signal observed in the blend is consistent with the blend naturally promoting charge generation though

the pristine is still notable for having a very high signal. As such the feature present in pristine ZZ115 hypothesised as the ZZ115 polaron, remains the ZZ115 polaron recombining in ZZ115:$PC_{60}BM$, but the nature of the feature has been altered as both the recombination kinetics and maximum peak position are changed in the blend.

More importantly the addition of fullerene acceptor leads to a noticeable peak around 700 nm before the ground state bleach obscures the signal. While a very initial hypothesis would place the 700 nm feature as the $PC_{60}BM$ polaron, it has already been measured at a different wavelength of 1070 nm[12] for the anion and 900 nm for the cation. Another hypothesis could identify it as the $PC_{60}BM$ triplet and this triplet was measured previously at the 710 nm wavelength[16]. Previous studies on the other hand have suggested this also be another ZZ115 polaron[11, 12] based on P3HT and other donor molecules showing dual polaron features, hence additional measurements are required to properly ascertain the nature of the second feature at 700 nm, starting with oxygen environment measurements in order to test the presence of triplet species.

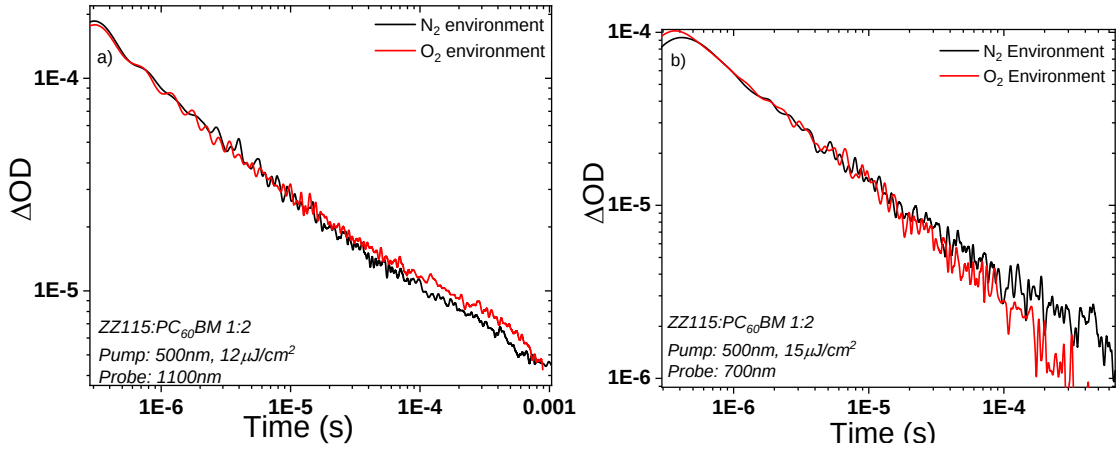

***Figure 3-7**: Transient absorption kinetics for ZZ115:$PC_{60}BM$ at a (1:2) blend ratio. Measurements were done with a pump wavelength of 500 nm, an excitation energy density of 12 uj/cm² and a probe wavelength of 1100 nm **(a)** or a probe wavelength of 700 nm **(b)**. The measurements were first done in a Nitrogen environment (Black line), followed by a measurement in an Oxygen environment (red line)*

Another series of measurements looked at the influence of an oxygen environment in an attempt to identify the presence of triplets and provide further insight in the two identified features of the blend. The change in ambient environment does have a significant impact on the kinetics as shown by ***Figure 3-7*** for both features studied. In

both features studied at the 700 nm and 1100 nm wavelength, the presence of oxygen has had no effect on the kinetics or amplitude. While it could be argued that ***Figure 3-7b*** shows a slight deviation in kinetics it does not appear significant enough to conclude that oxygen influences the kinetics. As such kinetic measurements should not be majorly influenced by triplets in the sample and polarons should be the only species visible at these wavelengths. Thus the 700 nm wavelength feature would be identified as a second ZZ115 polaron feature while the 1100 nm wavelength feature is indeed a ZZ115 polaron feature.

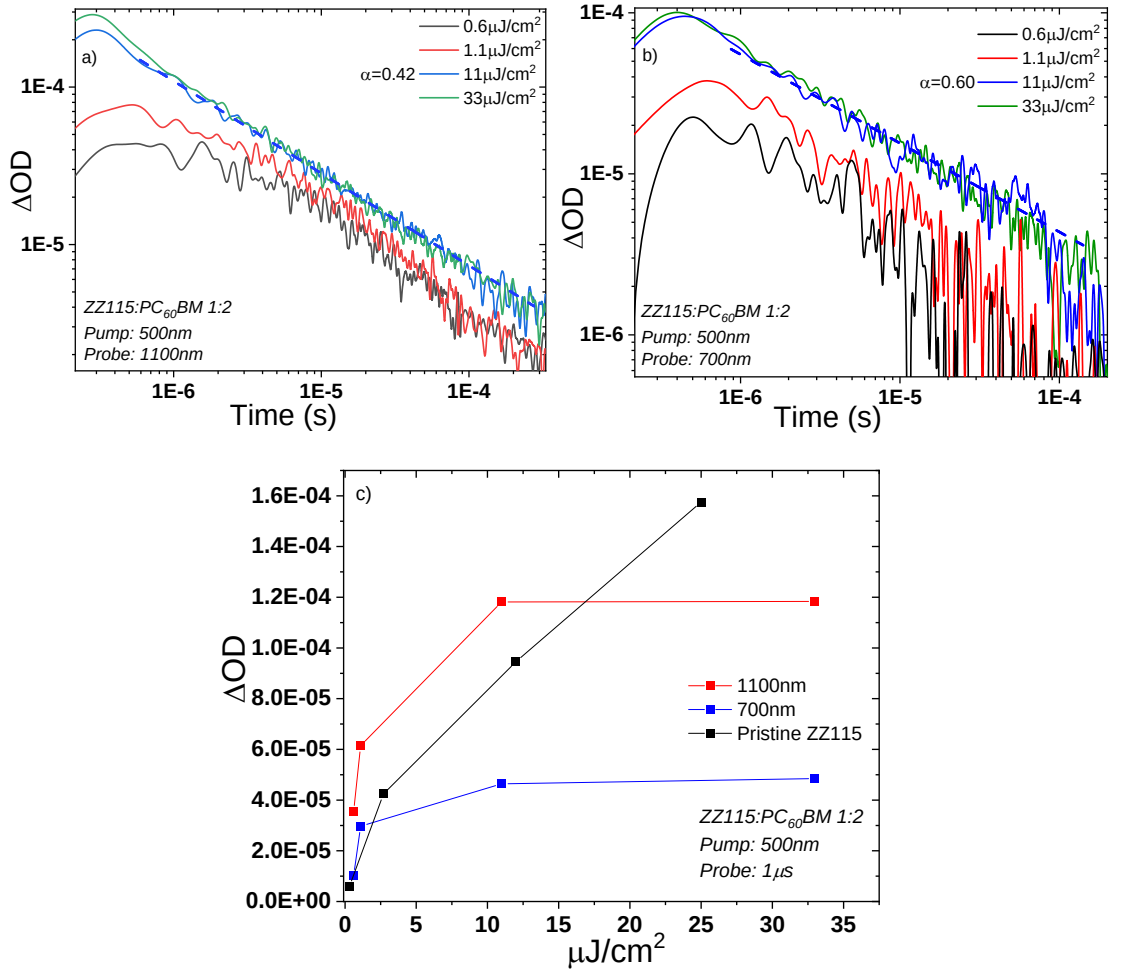

Figure 3-8: *Transient absorption kinetics for ZZ115:PC₆₀BM at the (1:2) blend ratio at different excitation energy densities. Kinetics were measured at 500 nm excitation wavelength and at different probe wavelengths.* ***(a)*** *shows the kinetics with a probe wavelength of 1100 nm.* ***(b)*** *shows the kinetics with a probe wavelength of 700 nm.* ***(c)*** *Energy saturation plot of the measured signal at 1 μs against excitation energy density*

As with the pristine material, the evolution of the kinetics with excitation density was characterised for the ZZ115:PC₆₀BM blend. And as with the pristine, ZZ115:PC₆₀BM

shows bimolecular recombination through a clear power law maintained at the different excitation energies. Moreover, the power law at 1100nm is noticeably slower than that of pristine ZZ115 as ***Figure 3-4*** shows an alpha value of 0.97 for pristine ZZ115 compared to 0.42. Additionally, the new feature found at the 700 nm wavelength in ZZ115:$PC_{60}BM$ shows an alpha of 0.6. The results presented in this section are relatively similar to those found in a previous work on ZZ115:$PC_{60}BM$[11] with a value for α of 0.43 at 1000 nm (close to the value presented here of 0.42 at 1100 nm for the same feature shown in ***Figure 3-8a***) and an α of 0.68 at 720 nm (compared to the value of 0.60 at 700 nm in this work in ***Figure 3-8b***). The first implication of this data is that ZZ115:$PC_{60}BM$ shows trap limited bimolecular recombination from the power laws observed. ***Figure 3-8c*** reinforces this by showing a saturation point much earlier than the pristine, hinting at the signal saturating due to the additional charges generated from increased excitation recombining earlier, while the ones measured at this timescale are charges escaping traps. This suggests that while bimolecular recombination occurs and several other recombination processes outlined previously are not present (such as triplet formation and geminate recombination), the addition of $PC_{60}BM$ leads to possibly deep trap states, which slows down the bimolecular recombination kinetics.

Both probed wavelengths do not show the same kinetics, however, which confirms two different features present in this material. The identity of these two features has been hypothesised in a previous work[11] as a delocalised ZZ115 polaron recombining at the 700 nm wavelength and a localised ZZ115 polaron recombining at the 1100 nm wavelength. This hypothesis stems from the similarity with P3HT:$PC_{60}BM$ which also displays a dual polaron feature[17] and a mix of amorphous-crystalline phase[18] as well as XIND [14] and PffBT4T-C9C13[19] also displaying dual polaron features. Time-of-flight investigations measuring the bimolecular recombination directly have suggested that a reduced bimolecular recombination is found in crystalline regions compared to mixed amorphous regions for ZZ115:$PC_{60}BM$ [20]. An updated hypothesis would thus identify ZZ115:$PC_{60}BM$ as having a ZZ115 polaron recombining in a ZZ115 crystalline medium at the 1100 nm wavelength and a ZZ115 polaron recombining in a mixed amorphous region at the 700 nm wavelength.

To complement the presented hypotheses as to the nature of the observed transient features, these measurements were compared to another fullerene acceptor in order to gain additional insight into the 700 nm and 1100 nm wavelength transient features.

3.2.3 Study of ZZ115 blended with $PC_{70}BM$ and comparison with $PC_{60}BM$

To gain a better understanding of the two polarons identified in the ZZ115:$PC_{60}BM$ TA spectrum, an identical study was performed with fullerene analogue $PC_{70}BM$. Efforts were made to replicate the conditions of the ZZ115 and ZZ115:$PC_{60}BM$ study.

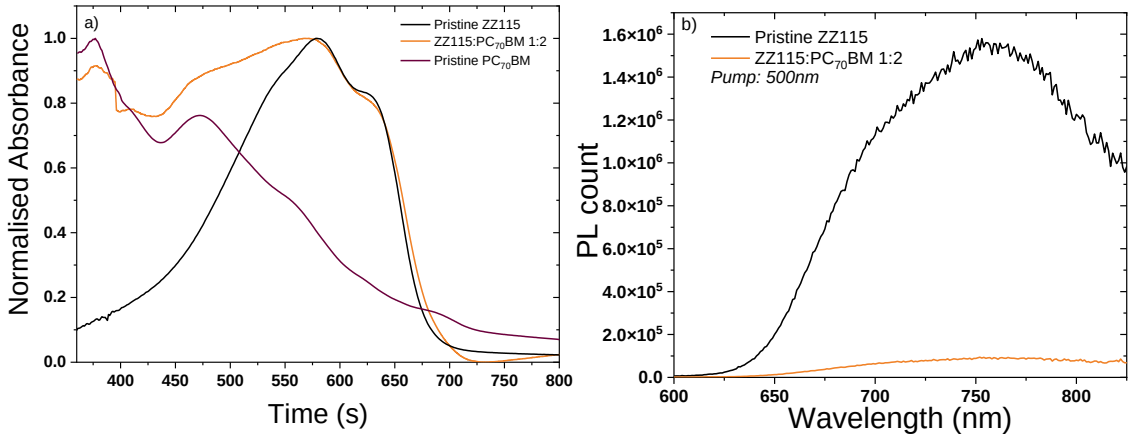

Figure 3-9: a) *Normalised ground state absorbance spectra of ZZ115:$PC_{70}BM$ samples at the 1:2 blend ratio, pristine $PC_{70}BM$ and pristine ZZ115. The spectrum is normalised to the 580 nm peak.* ***b)*** *Photoluminescence spectrum of ZZ115:$PC_{70}BM$ at the 1:2 blend ratio and pristine ZZ115. The excitation wavelength used was 500 nm.*

When comparing to the previous measurements, the addition of $PC_{70}BM$ to ZZ115 maintains the previously observed 520 nm shoulder, 580 nm primary peak and the secondary 640 nm peak while creating an elongated feature present from 500 nm to 350 nm, as seen by ***Figure 3-9***. Most notable in this elongated feature is the presence of two main peaks at 380 nm and 480 nm. This elongated 350 nm - 500 nm feature arises from the $PC_{70}BM$, which has a significantly stronger absorbance [3] in this region and more specifically has an absorbance spectrum that extends much further into the longer wavelengths than $PC_{60}BM$, illustrated by the pristine $PC_{70}BM$ absorbance in ***Figure 3-9a***. Conversely, the PL spectrum of the ZZ115:$PC_{70}BM$ blend follows the same as ZZ115:$PC_{60}BM$ with an exciton quenching of 94%. It stands thus that $PC_{70}BM$ has similar effects to $PC_{60}BM$ on both its morphology and excited states relaxation mechanism. This is an interesting observation given both fullerenes have

been reported to have different miscibility[21] in P3HT resulting in different morphologies. While not observed in ZZ115, it is possible that the two measured fullerenes would have different miscibility in ZZ115 and therefore result in different morphologies. Such an effect however is not observed in ***Figure 3-9a***, suggesting that the overall morphology of the two blends is similar. From ***Figure 3-9a***, just like the pristine sample, an excitation wavelength of 500 nm was used for consistency between the different fullerene systems.

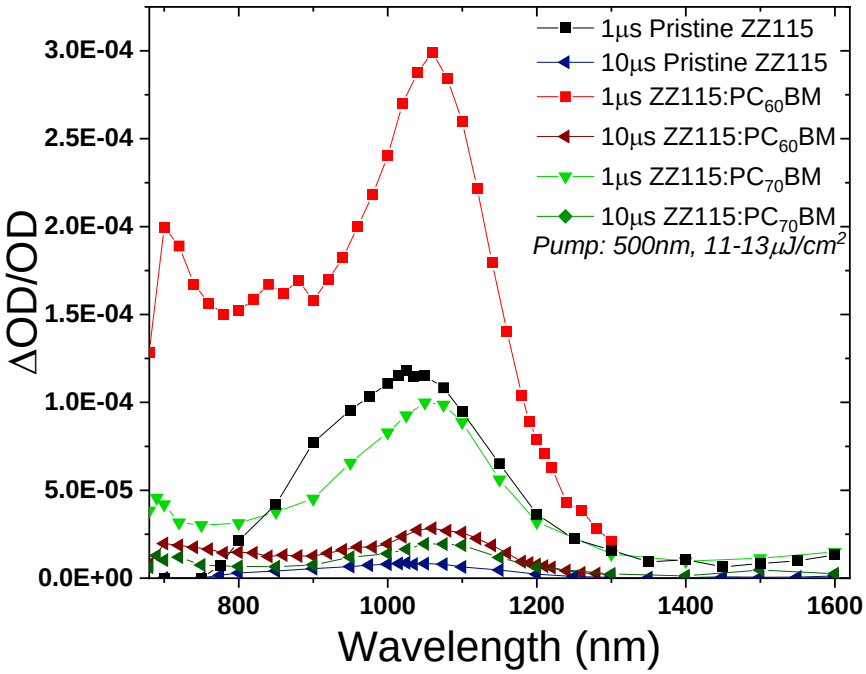

Figure 3-10: *Transient absorption spectra of ZZ115 pristine, ZZ115:PC60BM samples and ZZ115:PC70BM samples at a (1:2) blend ratio at 1 µs, and 10 µs timescale. Measurements were taken at 500 nm excitation wavelengths and with an 11-13 uJ/cm² excitation energy density. The spectrum is adjusted for photons absorbed.*

Switching the fullerene acceptor from PC60BM to PC70BM leads to a significant change in the 700 nm feature as the amplitude is diminished by close to 4 times in the PC70BM as seen in ***Figure 3-10***. Additionally, none of the features are PC70BM based as the PC70BM anion was identified at the 370 nm[22]. The central main ZZ115 feature in the 1050 nm peak appears unchanged however compared to the PC60BM with the same maximum peak shift seen in now both fullerenes in comparison to the pristine. The significant reduction in signal and thus charges generated is however quite noteworthy as the PC70BM based blend has up to three times fewer recombining charges compared to the PC60BM based blend. Even when compared to the pristine the ZZ115:PC70BM sees fewer recombining charges (around 20% less) though they

are longer lived just as with ZZ115:$PC_{60}BM$. It would thus seem that ZZ115:$PC_{70}BM$ generates much fewer charges than ZZ115:$PC_{60}BM$ though affirming ZZ115:$PC_{70}BM$ generates overall fewer charges than pristine ZZ115 will require an inspection of the kinetics. It does appear though that ZZ115:$PC_{70}BM$ has, as with ZZ115:$PC_{60}BM$, two ZZ115 polaron features at the 1100 nm wavelength and at the 700 nm wavelength.

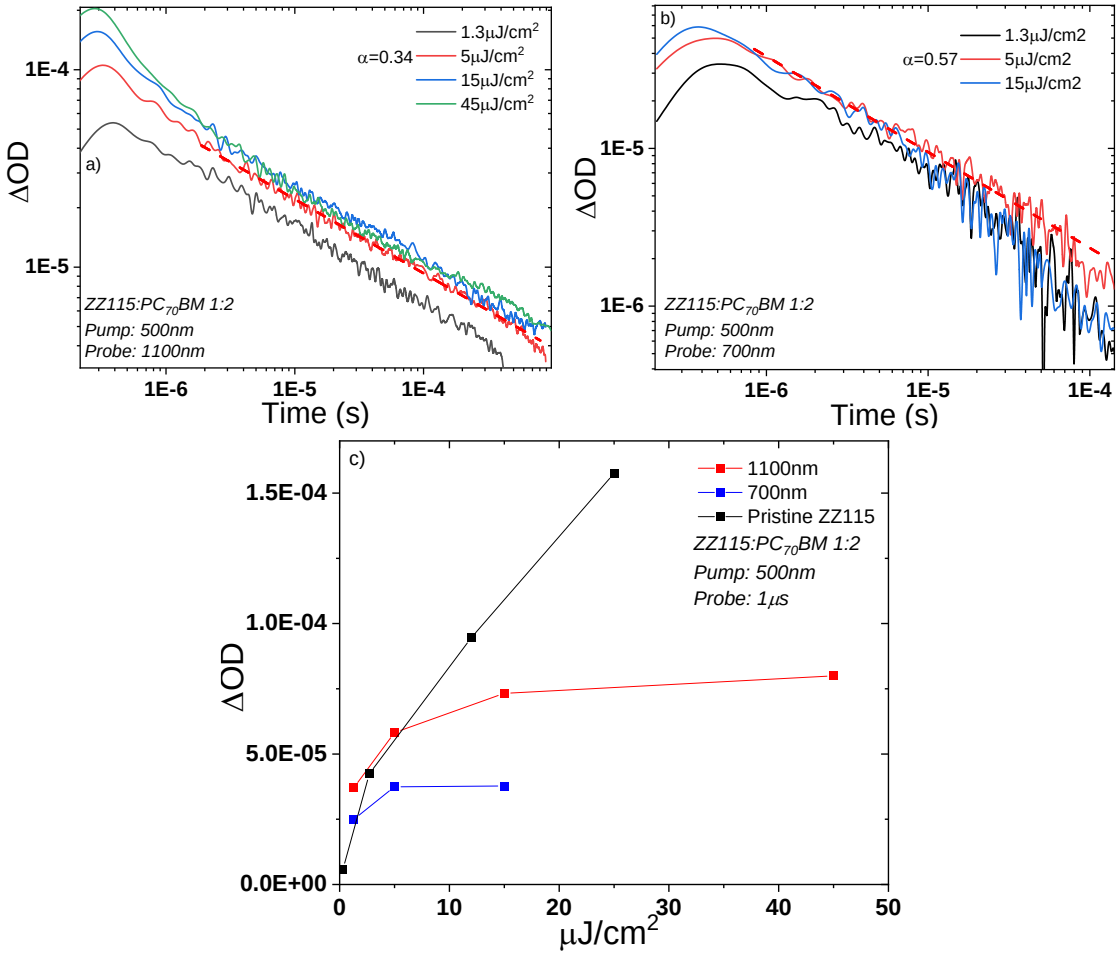

Figure 3-11: *Transient absorption kinetics for ZZ115:$PC_{70}BM$ at the (1:2) blend ratio at different excitation energy densities. Kinetics were measured at 500nm excitation wavelength and at different probe wavelengths.* ***(a)*** *shows the kinetics with a probe wavelength of 1100nm.* ***(b)*** *shows the kinetics with a probe wavelength of 700nm.*

Just as with ZZ115:$PC_{60}BM$, the evolution of kinetics in ZZ115:$PC_{70}BM$ samples was studied to confirm the kinetic mechanism. Thus ZZ115:$PC_{70}BM$ has a similar bimolecular recombination behaviour to ZZ115:$PC_{60}BM$, showing trap limited bimolecular recombination for the 1100 nm and 700 nm features. A similar saturation profile between the two systems can be also noticed as the signal saturates around the same excitation density of 10 μJ/cm². Due to the similarities between $PC_{60}BM$ and $PC_{70}BM$, it is also a reasonable hypothesis that the assigned features are similar.

Therefore ZZ115:$PC_{70}BM$ could be characterised as having a ZZ115 polaron feature in a ZZ115 crystalline region at the 1100 nm wavelength and a ZZ115 polaron in a mixed amorphous region at the 700 nm wavelength.

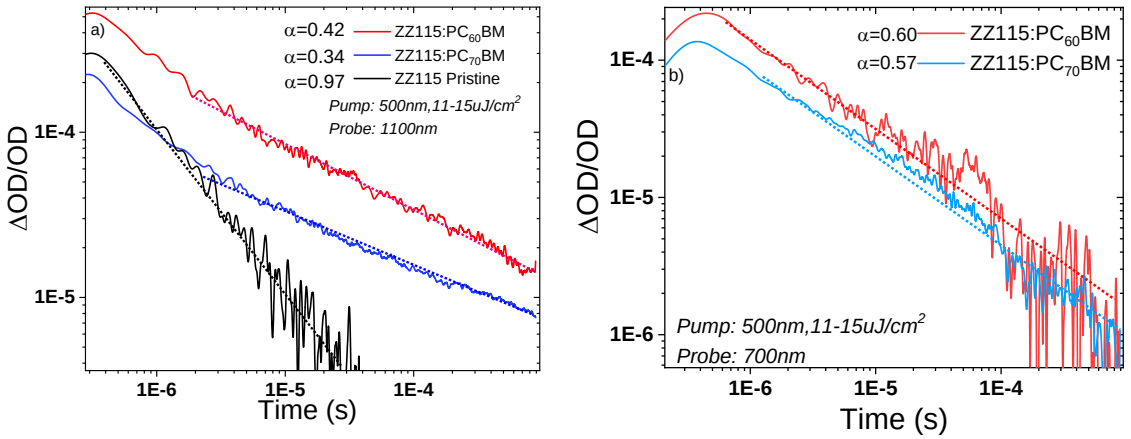

Figure 3-12: ***(a)*** *Transient absorption kinetics of ZZ115 pristine, ZZ115:$PC_{60}BM$ and ZZ115:$PC_{70}BM$ samples at a (1:2) ratio. Measurements were taken at 1100 nm probe wavelength, while* ***(b)*** *shows measurements taken at 700 nm probe wavelength. All measurements were with a 500 nm pump wavelength and an energy density of around 10 to 11-15 uJ/cm². The results are presented with the optical density normalised by photons absorbed for a more accurate comparison.*

A comparison of kinetics and amplitudes between the two fullerene blends shown in ***Figure 3-12*** highlights the important distinctions between the two fullerene blends. At the 1100 nm probe wavelength, $PC_{70}BM$ appears to have a consistently lower ΔOD (9.92×10^{-5} ΔOD compared to 2.9×10^{-4} ΔOD for ZZ115:$PC_{60}BM$ at 1μs) and slower kinetics with α values of 0.34 for $PC_{70}BM$ against 0.42 for $PC_{60}BM$. In contrast both fullerene blends have very similar kinetics of around α values of around 0.6 at the 700 nm wavelength but the $PC_{70}BM$ based blend has lower ΔOD (8.45×10^{-4} ΔOD compared to 1.37×10^{-5} at 1μs).

The higher signal found in ZZ115:$PC_{60}BM$ could be attributed to a larger number of charges in $PC_{60}BM$ based samples compared to $PC_{70}BM$ ones. This may be due to a worse miscibility of $PC_{70}BM$ in ZZ115 compared to $PC_{60}BM$ as has been reported to occur in the analogue P3HT[4]. As such ZZ115:$PC_{70}BM$ would have a reduced interfacial area between the two molecule regions, and this would limit charge generation and recombination as described in Sections **1.4** and **1.5** of Chapter **1**. No reports have been made as to confirm this in ZZ115 but the inherent similarities with P3HT lend credence to this hypothesis. The lack of major difference in PL quenching

behaviour, however, suggests that exciton kinetics are not affected by the change in fullerene. A change in interfacial area would be visible though PL spectroscopy.

The slower kinetics at the 1100 nm wavelength could be attributed to several possible factors. One possibility could be the increased size of the $PC_{70}BM$ molecule compared to $PC_{60}BM$. According to the initial TAS model of bimolecular recombination as described in the general introduction[23] localised polarons can become trapped by defects present in the material. In the case of a crystalline medium this would be traps caused by a disorder in the medium caused by the introduction of fullerene. As such the increased size of the acceptor molecule would lead to deeper traps due to more pronounced defects. The increased size however would have greater difficulty intercalating in the crystalline region[4], hence a reduced measured signal in ZZ115:$PC_{70}BM$ compared to ZZ115:$PC_{60}BM$.

In contrast the unchanging kinetics at the 700 nm wavelength cannot be attributed to the same phenomenon. It can however be surmised that the feature is the same: a ZZ115 polaron in a mixed amorphous region. The fact the kinetics appear identical reinforces this hypothesis as defects in an amorphous region would be significantly less impactful, even more so if the polaron is delocalised hence why changing the acceptor to a larger one does not affect the kinetics.

An initial picture has been established for all three systems of interest from a series of selective measurements. A more detailed analysis however is needed to properly ascertain these features and their implications.

3.3 Analysis and discussion

ZZ115 thin film samples were measured using UV-VIS, PL and TAS in order to identify the transient features of pristine films and films blended with $PC_{60}BM$ or $PC_{70}BM$. The results reveal the presence of one polaron transient feature at the microsecond timescale in the pristine ZZ115 and two polaron transient features at the microsecond timescale in ZZ115 fullerene blends. The traces themselves however can be further analysed from additional calculations.

3.3.1 Bimolecular recombination reaction order calculation

The kinetics traces measured can be further analysed by calculating the actual bimolecular recombination coefficient. The same methodology was applied as in [24] and is described in more detail in Chapter **2** under section **2.2.3.**

From the kinetic measurements summarised in ***Figure 3-12*** it is possible to glean additional insight by calculating the intrinsic properties of these systems. Firstly, the charge carrier density can be derived from the kinetics resulting in ***Figure 3-13*** using ε_{ZZ115} = 55000 L cm^2 mol^{-1} and d = 150 nm (values found in the previous studies of ZZ115 [25]).

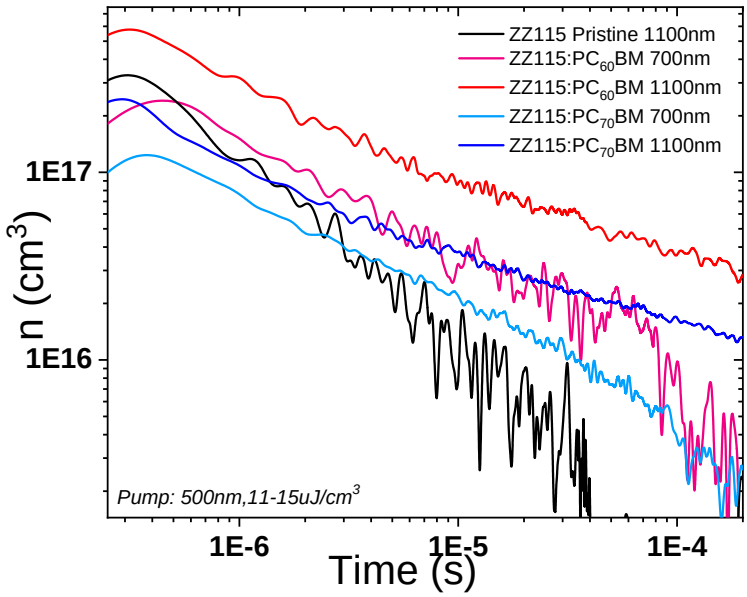

Figure 3-13: *Calculated charge carrier density from TAS kinetics over time for the pristine ZZ115 (black line), for the ZZ115:PC$_{60}$BM (1:2) blend (red line for the 700 nm feature, magenta for the 1100 nm feature) and for the ZZ115:PC$_{70}$BM (1:2) blend (cyan line for the 700 nm feature, blue for the 1100 nm feature)*

As can be expected the overall trends in charge carriers measured remain the same between the different features. As discussed previously the ZZ115:PC$_{60}$BM blend generates significantly more charges than the ZZ115:PC$_{70}$BM as well as more charges than the pristine (at 1100 nm, 3.19×10^{17} for ZZ115:PC$_{60}$BM vs 1.09×10^{17} for ZZ115:PC$_{70}$BM and 1.16×10^{17} for the pristine at 1 μs). It is once again notable that while less than the blend, the pristine still generates a significant number of charges for a non OPV optimal material choice and even more charges than the ZZ115:PC$_{70}$BM until around 1.5 μs.

The next sets of calculations revolve around estimating the reaction order of the recombination process using two different methods. The first was to plot the bimolecular recombination rate against the charge carrier density as shown in ***Figure 3-14***.

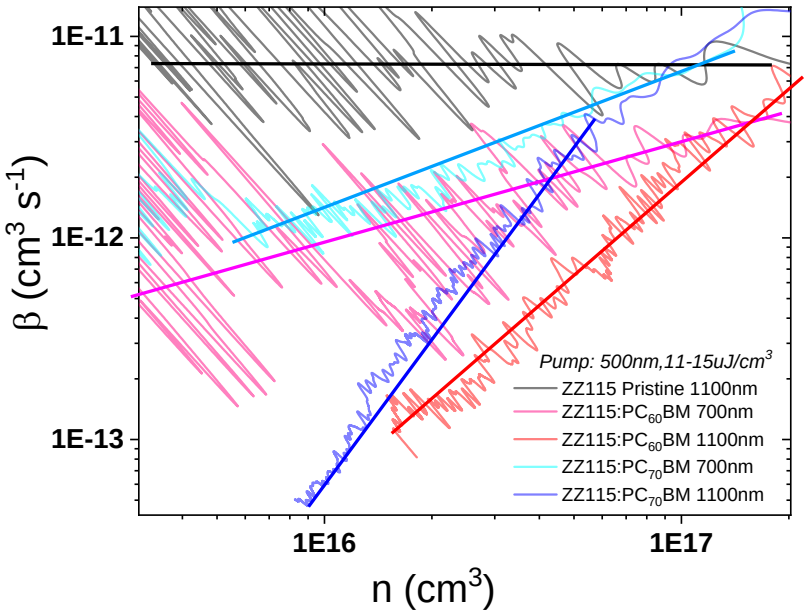

Figure 3-14:*Calculated bimolecular recombination coefficient from TAS kinetics against calculated charge carrier density for the pristine ZZ115 (black line), for the ZZ115+PC60BM (1:2) blend (red line for the 700nm feature, magenta for the 1100nm feature) and for the ZZ115+PC70BM (1:2) blend (cyan line for the 700nm feature, blue for the 1100nm feature)*

The bimolecular recombination coefficient for ZZ115 displays several unusual non-Langevin characteristics. Firstly, Pristine ZZ115 displays a β at around β=7.734 × 10^{-12} cm^3 s^{-1}, a value lower than the calculated Langevin bimolecular recombination coefficient of β_L=6 × 10^{-11} cm^3 s^{-1} by a factor of 10 (using a charge mobility of 1 × 10^{-4} cm^2 V^{-1} s^{-1} [26]). While this non-Langevin behaviour has been reported before, it is most peculiar that this behaviour is found in the pristine ZZ115, even if it is only a factor of 10. Unfortunately, no efficiency data exists for pristine ZZ115 devices to elucidate this unusual behaviour. With no acceptor to promote charge generation it would be expected that recombination of the few charges generated in pristine ZZ115 recombine easily as per Langevin mechanics. Instead, pristine ZZ115 generates a usually high number of charges that recombine slower than is expected. The blends on the other hand have an even lower coefficient that is charge carrier density dependant. This dependence can be characterised as the

bimolecular recombination reaction order by taking the slope of $\beta(n)$ (seen here with the straight lines in ***Figure 3-14***).

Using ***Figure 3-14***, the charge carrier lifetime can be calculated and plotted against charge carrier density.

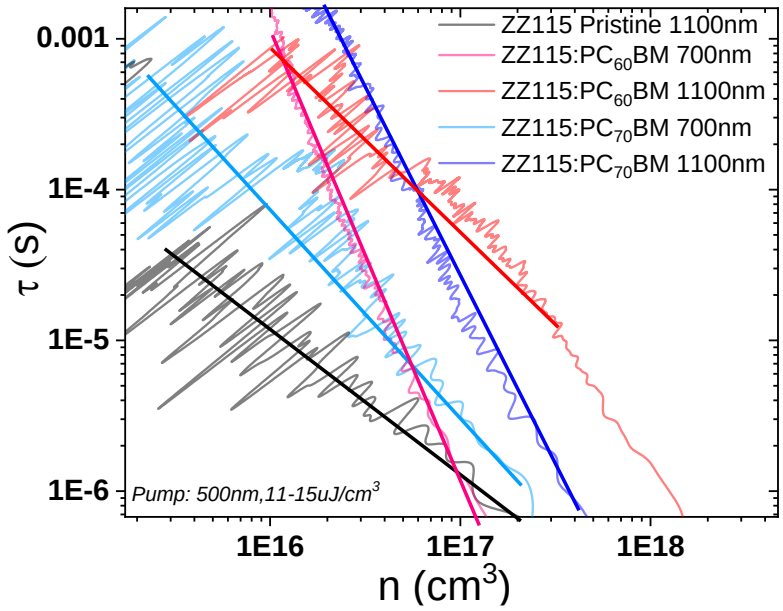

Figure 3-15: *Calculated charge carrier lifetime from TAS kinetics against calculated charge carrier density for the pristine ZZ115 (black line), for the ZZ115+PC60BM (1:2) blend (red line for the 700 nm feature, magenta for the for the 1100 nm feature) and for the ZZ115+PC70BM (1:2) blend (cyan line for the 700 nm feature, blue for the for the 1100 nm feature)*

As with β vs n (***Figure 3-14***), the reaction order can be calculated via the slope of each of the traces in ***Figure 3-15***. The calculated reaction order is shown in Table **3.16** and compared to the calculated reaction order using ***Figure 3-14***.

Table 3-1: *Table of the slopes from the curves from Figures 3-14 and 3-15 and calculated reaction orders based on said slopes*

System	***Figure 3-15*** power law fit coefficient (η)	***Figure 3-14*** power law fit coefficient (λ)	Reaction Order calculated ($\varphi_1=\eta+2$)	Reaction Order calculated ($\varphi_2=\lambda+1$)	Average of calculated reaction orders φ_a
ZZ115 Pristine	0	0.82	2	1.82	**1.91**
ZZ115+$PC_{60}BM$ 1100nm	1.36	2.89	3.36	3.89	**3.61**
ZZ115+$PC_{70}BM$ 1100nm	1.88	2.57	3.88	3.57	**3.72**
ZZ115+$PC_{60}BM$ 700nm	0.88	1.25	2.88	2.25	**2.57**
ZZ115+$PC_{70}BM$ 700nm	0.70	1.35	2.70	2.35	**2.52**

Thus, three reaction regimes can be found corresponding to each of the three identified features: a reaction order of around 2 for the pristine, a reaction order of around 2.5 for the 700 nm blend features, and a reaction order of around 3.6-3.7 for the 1100 nm blend features.

3.3.2 Summary and Broader Discussion

From all measurements and calculations, pristine ZZ115 reveals an unusual duality. The actual β coefficient is lower by a factor of 10^{-2} - 10^{-3} compared to the Langevin bimolecular recombination coefficient β_L. Several factors could lead to this paradigm. A possibility would have pristine ZZ115 observe pure Langevin mechanics, but an intrinsic local distortion could locally reduce the charge carrier mobilities which would reduce the bimolecular recombination coefficient as seen with **Equation (1-11)** from the general introduction. Reduced charge carrier mobilities has been found to be a potential cause of reduction in bimolecular recombination coefficient compared to Langevin theory[27] by C. G. Shuttle *et al.* on P3HT:$PC_{60}BM$. Taking the

initial previously established hypothesis of the pristine ZZ115 1100 nm wavelength TAS feature as the ZZ115 polaron recombining in a crystalline medium, there arises at least two potential causes for reduction of bimolecular recombination rate.

The first potential cause for this reduction in β would be a reduction due to an intrinsic property of ZZ115 on a fundamental molecular level. Studies so far have not delved into an in-depth theoretical modelling of ZZ115 to reveal the presence or absence of an outstanding electronic or molecular characteristic and thus further study is necessary and will be done in a later chapter.

The second potential cause for this reduction in β would be from the ordered crystalline phase itself. It has very recently been measured in our previous paper that for ZZ115 pristine, a low energy intragap charge transfer state[13] exists, in addition to the HOMO of ZZ115 appearing delocalized. This intragap could serve as a source for this reduction in mobility by impeding the charges due to serving as an energy well, akin to a trap but not deep enough to fully trap the charges, even more so if the polaron is delocalised. Parallel to this, previous studies on similar molecules such as P3HT have shown local mobility increases due to possible π-π stacking [28], as well as increases in mobility as a result of annealing and thus[29] increased crystallinity. As such, local reduced crystallinity or impeded π-π stacking could lead to reduced local mobility in ZZ115, though this has not yet been observed. It is important to note however that many comparisons to previous studies are rendered difficult due to the focus on blend systems in comparison to pristine systems. In summary pristine exhibits an 1100nm wavelength TA feature showing unusual characteristics in the number of charges recombining as well as the bimolecular recombination rate coefficient. While it has been hypothesised that this is due to the ZZ115 polaron recombining in a crystalline medium with local charge carrier mobility reduction features, explanation of ZZ115's unusual bimolecular recombination behaviour has not been fully achieved.

The blend systems conversely show a very different paradigm altogether. Looking first at the 1100 nm wavelength feature, the addition of fullerene leads to a very different reaction order and overall behaviour compared to pristine ZZ115. Quite notably however, the bimolecular recombination rate coefficient for both pristine and

blend intersect (around 6×10^{-12} cm^3 s^{-1} as seen in ***Figure 3-15***), highly suggesting the features are the same fundamentally. On the other hand, the reaction order of over 3, α coefficient around 0.4, and $\beta(n)$ decay leads to a deviation with evidence of trap-limited recombination. In particular the high reaction order of over 3 is not covered by traditional reaction models and highlights the complexity of the recombination process for this feature. An important study T. Kirchartz and J. Nelson[30] suggested the high reaction order could be caused by the shape of the density of states as well as the spatial heterogeneity of charge carriers. Studies have searched for unusual features present in donor molecule systems for example the intragap state in pristine ZZ115 previously hypothesised[13]. Within our same study it was theorised than the introduction of fullerene would replace the inherent pristine intragap state, possibly formed from a spatial inhomogeneity of charge carriers, and localise the HOMO onto the dithienosilole donor unit of ZZ115. Our study did not consider $PC_{70}BM$ as a point of comparison, but the overall logic could possibly apply to other similar fullerene species, with the increased size of the fullerene creating a greater charge spatial inhomogeneity hence deeper traps and slower kinetics. It does stand thus that this blend feature corresponds to the ZZ115 polaron recombining in a crystalline phase, with the addition of the fullerene causing a possible structural and electronic change when compared to the original pristine 1100 nm feature.

The 700 nm feature present in the blend systems does not appear in the pristine polymer. As mentioned previously its wavelength does not correspond to any PC_xBM polaron or triplet, making it another ZZ115 polaron feature. The different transient kinetic characteristics compared to the 1100 nm would suggest a different medium but still a ZZ115 polaron. Based on previous studies on ZZ115 as well as other similar systems this would characterise the feature as a ZZ115 polaron in a mixed amorphous region. The lower reaction order of just under 3, α coefficient around 0.6, and $\beta(n)$ decay once again point to a trap-based recombination model, but to a lower extent than that of the 1100 nm feature, hence the hypothesis of the mixed amorphous phase. Emphasis has been made in previous studies on the delocalised nature of the polaron which would explain the faster kinetics due to a lesser susceptibility to traps. The faster kinetics may also be attributed to a greater ease of access to the donor-acceptor

interface within mixed amorphous phases. Interestingly such a reaction order (close to 3) has been theorised [31] and modelled for P3HT:$PC_{60}BM$. There it was found that P3HT is best modelled by having an exponential density of states and the charge recombination modelled by recombination using the tail states of the DOS, but the exact morphology modelled was not extensively delved into. Given the parameters used however the system could be described as a mixed amorphous phase. As such while evidently a different system it does provide credence to the allocation of the ZZ115 polaron in a mix amorphous phase at 700 nm. It is however a limited connection as other models such as Auger recombination are also third order and could also be used to model this feature. The current assignment of features (ZZ115 polaron in crystalline ZZ15 at 1100nm and ZZ115 polaron in mixed amorphous phase at 700nm) remains however the most likely assignment, though the exact mechanism governing the feature is still unknown.

From a broader perspective, previous works on several other donor/acceptor material systems have also found dual polaron features[2, 14, 17, 19] present. As mentioned previously, P3HT displays this dual feature when combined with $PC_{60}BM$ and $PC_{70}BM$. The novel electron donor/acceptor molecule XIND[14] also displays a dual polaron feature when combined with these two fullerene acceptors. Remarkably XIND also displays a dual polaron feature when paired with P3HT as XIND takes the role of electron acceptor. P3HT:$PC_{60}BM$ has been studied extensively such that a morphological optimisation has led to the promotion of intermolecular crosslinking and an overall emphasis on increased crystallinity for better device performance. As mentioned in the general introduction, this increase in crystallinity has been found to lead to a reduction in bimolecular recombination coefficient. The polymer XIND has not been studied as extensively but initial study has outlined the importance of the morphology due to the dual donor/acceptor properties of this polymer. A key point established by Jose *et al.*[14] was the important interplay between the bulk crystalline polarons and interfacial polarons, and the subsequent behavioural difference depending on the blended material. Finally the polymer series PffBT4T[19] has displayed this dual polaron feature with even a highlight of fast kinetics in an amorphous region and trapped localised polarons in crystalline region. The study

focuses more on the characterisation of triplet features but highlights the enhancement of crystallinity upon introduction of fullerene from enhanced ordering and π-π stacking. This latter point has not been found in ZZ115 but remains a possibility within the confines of the crystalline domains. It does stand thus that the structural medium and ordering of ZZ115 plays a crucial role leading to highly unusual properties in its pristine system, and blend properties reminiscent of other non-Langevin systems.

3.4. Conclusion

This chapter is part of a larger study aimed at understanding the bimolecular recombination process of charge carriers in organic photovoltaic cells. This experimental chapter aimed to provide the basic framework on which to base more detailed studies, as well as initial insights as to the influence of acceptor type on the non-Langevin material ZZ115. The results showcase the unusual nature of ZZ115 as a donor, with the pristine exhibiting transient kinetic properties unexpected and still not fully explained. The results also show evidence of trap limited bimolecular recombination in ZZ115 based samples regardless of the chosen acceptor. Two separate features were found for these samples which were theorised to be the ZZ115 polaron recombining in a ZZ115 crystalline region at the 1100 nm wavelength, and the ZZ115 polaron recombining in a mixed amorphous region at the 700 nm wavelength. These assignments are due to the former showing trap limited bimolecular recombination vs the trap free recombination of the pristine while the latter shows a much less limited recombination process. Substituting the $PC_{60}BM$ fullerene with $PC_{70}BM$ leads to very similar results albeit with deeper traps compared to $PC_{60}BM$ for the 1100 nm feature. This chapter has therefore laid the groundwork for the later study on the ZZ115:$PC_{60}BM$ and ZZ115:$PC_{70}BM$ systems performed in Chapter **4**.

3.5. References

1. J. C. Hummelen, B. W. Knight, F. LePeq, F. Wudl, J. Yao, and C.L. Wilkins, *Preparation and Characterization of Fulleroid and Methanofullerene Derivatives.* J. Org. Chem., 1995. **60**(3): p. 532-538.
2. P. R. Berger and M. Kim, *Polymer solar cells: P3HT:PCBM and beyond.* Journal of Renewable and Sustainable Energy, 2018. **10**.
3. Y. He and Y. Li, *Fullerene derivative acceptors for high performance polymer solar cells* Phys. Chem. Chem. Phys., , 2011. **13**: p. 1970-1983
4. F. Zhanga, Z. Zhuoa, J. Zhang, X. Wanga, X. Xua, Z. Wanga, . . . Y. Wang, *Influence of PC60BM or PC70BM as electron acceptor on the performance ofpolymer solar cells.* Solar Energy Materials & Solar Cells, 2011. **97**.
5. Y. Santo, I. Jeon, K. S. Yeo, T. Nakagawa, and Y. Matsuo, *Mixture of [60] and [70]PCBM giving morphological stability in organic solar cells.* Applied Physics Letters 2013. **103**.
6. C. Yanm, S. Barlow, H.Y. Z. Wang, A. K.-Y. Jen, S. R. Marder, and X. Zhan, *Non-fullerene acceptors for organic solar cells.* Nature reviews, 2018.
7. J. Peet, L. Wen, P. Byrne, S. Rodman, K. Forberich, Y. Shao, . . . D. Waller, *Bulk heterojunction solar cells with thick active layers and high fill factors enabled by a bithiophene-co-thiazolothiazole push-pull copolymer* Appl. Phys. Lett., 2011. **98**.
8. S. Hayashi, S.-I Yamamoto, and T. Koizumi, *Effects of molecular weight on the optical and electrochemical properties of EDOT-based π-conjugated polymers.* Sci Rep, 2017. **7**.
9. Spano, F.C., *Modeling disorder in polymer aggregates: The optical spectroscopy of regioregular poly(3-hexylthiophene) thin films.* The journal of chemical physics, 2005. **122**(23).
10. L. Wang and D. Beljonne, *Optical properties of regioregular poly(3-hexylthiophene) aggregates from fully atomistic investigations.* CrystEngComm, 2016(38).

11. T. M. Clarke, C. Lungenschmied, J. Peet, N. Drolet, K. Sunahara, A. Furube, and A.J. Mozer, *Photodegradation in Encapsulated Silole-Based Polymer: PCBM Solar Cells Investigated using Transient Absorption Spectroscopy and Charge Extraction Measurements* Advanced Energy Materials, 2013. **3**: p. 1473-1483.

12. T. M. Clarke, J. Peet, P. Denk, G. Dennler, C. Lungenschmied, and A. .J. Mozer, *Non-Langevin bimolecular recombination in a silole-based polymer:PCBM solar cell measured by time-resolved charge extraction and resistance-dependent time-of-flight techniques* Energy and Environmental Science, 2012(1).

13. Marin-Beloqui, J.M.Z., Guanran; Guo, Junjun; Shaikh, Jordan; Wohrer, Thibaut; Hosseini, Seyed Mehrdad; Sun, Bowen; Shipp, James; Auty, Alexander; Chekulaev, Dimitri; Ye, Jun; Chin, Yi-Chun; Sullivan, Michael; Mozer, Attila; Kim, Ji-Seon; Shoaee, Safa; Clarke, Tracey, *Insight into the origin of trapping in polymer / fullerene blends with a systematic alteration of the fullerene to higher adducts*. 2021: The journal of physical chemistry.

14. J. M. Marin-Beloqui, K. J. Fallon, H. Bronstein, and a.T.M. Clarke, *Discerning Bulk and Interfacial Polarons in a Dual Electron Donor/Acceptor Polymer.* J. Phys. Chem. Lett., 2019. **10**: p. 3813-3819.

15. J. Piris, T. E. Dykstra, A. A. Bakulin, P. H. M. van Loosdrecht, W. Knulst, M. T. Trinh, . . . L.D.A. Siebbeles, *Photogeneration and Ultrafast Dynamics of Excitons and Charges in P3HT/PCBM Blends.* J. Phys. Chem. C., 2009. **113**(3214500–14506).

16. E. A. Lukina, I. P. Pozdnyakov, A. S. Mereshchenko, M. N. Uvarov, and L. V. Kulik, *Photochemistry of P3HT and PC60BM in toluene solution: Evidence ofT–T energy transfer.* Journal of Photochemistry and Photobiology A: Chemistry, 2015.

17. J. Guo, H. Ohkita, H. Benten, and S. Ito†, *Charge Generation and Recombination Dynamics in Poly(3-hexylthiophene)/Fullerene Blend Films with Different Regioregularities and Morphologies.* Journal of the American Chemical Society, 2010.

18. T. M. Clarke, J. Peet, C. Lungenschmied, N. Drolet, X. Lu, B. M. Ocko, . . . M.A. Loi, *The role of emissive charge transfer states in two polymer–fullerene organic photovoltaic blends: tuning charge photogeneration through the use of processing additives.* Jounal of Materials Chaemistry A, 2014(31).

19. J. Guo, J. M. Marin-Beloqui, and T.M. Clarke, *Bimodal polarons as a function of morphology in high efficiency polymer/acceptor blends for organic photovoltaics.* Journal of Physics: Materials, 2021. **4**(4).

20. T. M. Clarke, C. Lungenschmied, J. Peet, N. Drolet, and A.J. Mozer, *Tuning Non-Langevin Recombination in an Organic Photovoltaic Blend Using a Processing Additive.* J. Phys. Chem. C., 2015. **119**.

21. F. Zhanga, Z. Zhuoa, J. Zhang, X. Wanga, X. Xua, Z. Wanga, . . . Y. Wang, *Influence of PC60BM or PC70BM as electron acceptor on the performance of polymer solar cells.* Solar Energy Materials & Solar Cells, 2011. **97**.

22. D. R. Lawson, D. L. Feldheim, C. A. Foss, P. K. Dorhout, C. M. Elliott, C. R. Martin, and B. Parkinson, *Near-IR Absorption Spectra for the Buckminsterfullerene Anions: an Experimental and Theoretical Study.* Journal of the Electrochemical society, 1992. **139**(7).

23. J. Nelson, *Diffusion recombination in polymer-fullerene blends and its influence on photocurrent collection.* Physical Review B, 2003. **67**(15).

24. T. M. Clarke, F. C. Jamieson, and J.R. Durrant, *Transient Absorption Studies of Bimolecular Recombination Dynamics in Polythiophene/Fullerene Blend Films.* J. Phys. Chem. C., 2009. **113**(49): p. 20934–20941.

25. T. M. Clarke, C. Lungenschmied, J. Peet, N. Drolet, and A.J. Mozer, *A Comparison of Five Experimental Techniques to Measure Charge Carrier Lifetime in Polymer/Fullerene Solar Cells.* Advanced Energy Materials, 2014. **5**(4).

26. T. M. Clarke, D. B. Rodovsky, A. A. Herzing, J. Peet, G. Dennler, D. DeLongchamp, . . . A.J. Mozer, *Significantly Reduced Bimolecular Recombination in a Novel Silole-Based Polymer: Fullerene Blend.* Advanced Energy Materials, 2011. **1**(6).

27. C. G. Shuttle, R. Hamilton, J. Nelson, B. C. O'Regan, and J. R. Durrant, *Measurement of Charge-Density Dependence of Carrier Mobility in an Organic Semiconductor Blend.* Advanced Functional Materials, 2010. **20**(5).
28. E. Tomita, K. Kim, K. Minegishi, A. Makamura, S. Kanehashi, and K. Ogino, *Enhancement of Out-of-Plane Hole Mobility in Poly(3-Hexylthiophene)-b-Poly(styrene) Film.* Macromolecular Chaemistry and Physics, 2018. **219**(18).
29. S. Cho and K. Lee, *Thermal annealing-induced enhancement of the field-effect mobility of regioregular poly(3-hexylthiophene) films.* Journal of Applied Physics, 2006. **100**(11).
30. T. Kirchartz and J. Nelson, *Meaning of reaction orders in polymer:fullerene solar cells.* Physical Review B, 2012.
31. R. C. I. Mackenzie, T. Kirchartz, G. F. A. Dibb, and J. Nelson, *Modeling Nongeminate Recombination in P3HT:PCBM Solar Cells.* The journal of physical chemistry, 2011. **115**(19).

Chapter 4: Gauging the effects of fullerene loading on ZZ115-fullerene films.

4.1. Introduction

Chapter **3** provided an introductory characterisation of ZZ115 based samples to provide insight on the bimolecular recombination process. The conclusions provided in Chapter **3** alluded to the need of better understanding of the material system in order to correctly identify the transient features as well as to explain differences found between two very similar fullerenes. This chapter aims to provide a more in depth look by studying how a variation in fullerene concentration affects the transient features found in Chapter **3** in terms of electronic and morphological disruption. In addition, another characterisation technique, ps-TAS, is used for additional insight on these transient features in addition to atomic force microscopy (AFM) providing morphological measurements that could elucidate the unusual nature of ZZ115.

The optimal blend ratio for best device performance has been found for many systems, such as a 1:1 ratio for the P3HT:$PC_{60}BM$ system thanks to many studies focused on purely device performance[1-8]. Even within the aforementioned studies there have been discrepancies, with a best device performance being found for a P3HT:$PC_{60}BM$ blend ratio ranging from 3:1, 2:1, 1:1, 1:2 or even 1:3. Consensus has appeared to have converged on the 1:1 ratio being the optimal ratio for the P3HT:$PC_{60}BM$ system. Conversely the PTB7:$PC_{70}BM$ system has also been studied and the optimal device ratio of 1:1.5[9-11]was found but the origin of such an optimal device ratio was not established. Other studies instead have studied the exact effect of an increased fullerene concentration and the underlying reason for why a material system has a particular optimal device blend ratio.

An in depth study by W. Huang *et al.* [12] found the optimal device ratio for PTB7:$PC_{70}BM$ to be around 1:1.5-1:2 through study of efficiency properties of blend devices. More importantly, the effect of fullerene loading on the microstructure was studied, finding three different regimes. The first regime found at low (<50wt%) fullerene loadings sees the fullerene highly dispersed within the mixed phase, with significantly hampered exciton dissociation. The medium loading (50-70wt%) sees the formation of fullerene clusters leading to enhanced energetic order. Finally, the high fullerene loading(>70wt%) sees fullerene domain size growing to exceed the

exciton diffusion length of the polymer leading to reduced exciton dissociation efficiency. A different study on the PBTTT:$PC_{70}BM$ system using TAS by D. W. Gehrig *et al.*[13] focused on the 1:1 (50wt%) and 1:4 (20wt%) blend ratios in order to compare a pure co-crystal morphology with a mix of crystal and fullerene aggregate morphology. The authors found that the fullerene aggregates play an important role in not only the charge generation but also the spatial charge separation as the 1:4 blend showed a greatly enhanced free carrier generation yield and separation efficiency. A previous study by A. C. Mayer *et al.* [14] on the PBTTT:$PC_{70}BM$ system had found the optimal device ratio of 1:4 stemming from fullerene intercalation forming ordered bimolecular crystals, suggesting the high fullerene loading necessary due to the combination of intercalation and fullerene aggregation to maximise free carrier generation. Another study by C. Zhang *et al.* [15] used a variety of techniques on the PTB7 polymer donor combined with a variety of acceptors including $PC_{60}BM$, PyF5, and FAP1. It was found that an increased miscibility of the donor-acceptor pair led to the optimal device blend ratio to steer towards the higher fullerene content devices. This was in addition to findings of the crystallinity of the system playing an important, but not vital, part in determining the optimal donor-acceptor ratio, based on an increase in electron mobility found after loading of amorphous-dominated fullerene PyF5 compared to loading of crystalline dominated fullerene FAP1. Another study by M. T. Sajjad *et al.* [16]analyses with PL a material combination of donor polymer AnE-PV and $PC_{60}BM$ using semi crystalline and amorphous forms of the donor polymer. The polymer was chosen for its ease of control of its amorphous and crystalline form. The influence of crystallinity with a variation in fullerene concentration of 0, 0.5 and 1 wt.% while also adjusting the mix of semi-crystalline and amorphous donor polymer was studied. It was found that a higher crystallinity increases the exciton diffusion length and reduces fullerene-donor polymer mixing. Thus, these studies have highlighted the complex interplay between fullerene aggregation, polymer crystallinity and fullerene-polymer mixing in determining the optimal device ratio. The fullerene-polymer mixing in particular has been found to be phenomenon of great importance in device optimisation for OPVs.

The presence of a mixed donor/acceptor phase in the OPV active layer is a well characterised phenomenon showing the significant challenge for morphology device optimisation, with an interplay between enhanced charge generation due to a favourable interface[17], and increased recombination due more difficult charge collection pathways[18]. The enhanced charge generation has led to mixed amorphous phases being found as a desired design quality since the advent of bulk heterojunction OPVs. This has been disputed with reports of good device performance with either no mixed phase[19]in a study by Oosterhout *et al.* on the small molecule system X2:$PC_{60}BM$, or with reduced donor-acceptor interface from mixed phase[20]as seen in a study by Veldman *et al.* on the copolymer PF10TB. Additionally, it was found[21], as seen in a study by Ferron *et al.* on P3HT:$PC_{60}BM$, that reducing the width of the mixed phase located between pure molecule phases promotes CT state separation thanks to a steeper energetic gradient combined with a proximity to delocalised states in the pure phases, thus improving charge generation. The full role of the mixed phase is still however not fully understood[22]and its effects are still studied to this day.

The interplay between localised and delocalised states in particular at the donor-acceptor interface is a key facet of efficient OPVs[23]. Charge carrier delocalisation has been [24, 25]deemed crucial for efficient free charge carrier generation and dissociation and has been shown to lead to enhanced charge separation but at the cost of faster recombination[26]. This delocalisation has been found, in a study[27]by Gautam *et al.* on DTG-TPD, P3HT, and PTB7 combined with $PC_{60}BM$, to be induced by fullerene loading, with in particular the interface between the donor and polymer as well as excited-state polarisability being key to state delocalisation.

It stands as such that acceptor concentration has a morphological effect, an energetic and electronic effect on the system which leads to potentially substantial changes in device performance and potentially charge recombination behaviour. This present study aims to use this variation in acceptor concentration to provide morphological and electronic insight into the studied systems and thus the transient features first identified in Chapter **3**, while also gleaning insight into the properties of certain blend ratios not commonly studied.

4.2. Experimental Methodology

The key focus of this chapter was, in addition to using previously described techniques, collaboration with partners in order to use different tools to gain additional insight on the observed features. The techniques used by collaborators are briefly described below.

4.2.1 Ultrafast TAS experimental details

While ps TAS follows the same general principles as μs TAS, there are a few important differences in experimental set-up. The main difference lies in the probe light not being generated by a continuous white light source (like a halogen lamp) but instead from a pulsed light with a time delay between the pump and the probe. The time delay is created thanks to a delay stage. The overall difference between ps and μs TAS is illustrated by comparing ***Figure 2-4*** from Chapter **2** with ***Figure 4-1.*** The probe beam generates a white light continuum thanks to a white light generator. The reason for this change in set up stems from the time resolution needed to observe species on such short lifetimes. Longer timescales require longer delay stages, which are not appropriate for μs timescales due to the stage length required (a delay stage of around 200 m).

The laser emits a pulsed signal on the femtosecond timescale. This beam is amplified and then split into two beams, the pump and the probe. The pump has a specific beam wavelength selected via an OPA to create the pulse pump signal. This pump signal has alternate pump pulses blocked by a synchronised chopper in order to measure the sample excited and unexcited similar to μs TAS measurements. The probe signal is delayed depending on the time scale studied thanks to a delay stage to create the probe signal. The pump signal hits the sample, exciting it. After a given time delay the probe passes through the sample and the signal is recorded.

The main aim of using ps TAS within the context of this study is to provide additional insight into the hypotheses established earlier in the microsecond TAS measurements of Chapter **3**. More precisely the aim is to investigate the transient absorption spectra

of ZZ115:$PC_{60}BM$ at earlier timescales to measure geminate recombination in ZZ115:$PC_{60}BM$.

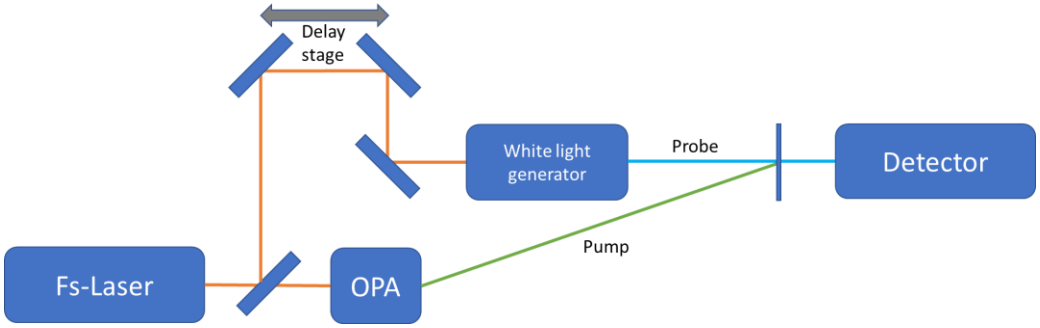

Figure 4-1: *Simplified diagram of ultrafast transient absorption spectroscopy set-up*

4.2.3. Atomic Force Microscopy (AFM)

The other experimental technique lies in atomic force microscopy (AFM). This technique relies on the electronic repulsion of a charged tip going along the atomic surface of a material to describe the surface morphology of the sample, with a typical set-up given in ***Figure 4-2***. The movement of the tip attached to a cantilever is recorded by a laser signal. The resulting voltage from the tip movement allows a mapping of the surface roughness. The use of AFM within the context of this study is to provide a direct morphological view of the different material systems studied and the effects of concentration variation of the acceptor on the morphology. This technique notably allows a very good view of the overall surface morphology but is unfortunately limited in resolution due to cantilever oscillation coupled with the photodiode time resolution (1-5 nm lateral resolution with 1 Å height resolution[28]), in addition to the inherent limitation of the surface morphology potentially differing from the bulk morphology.

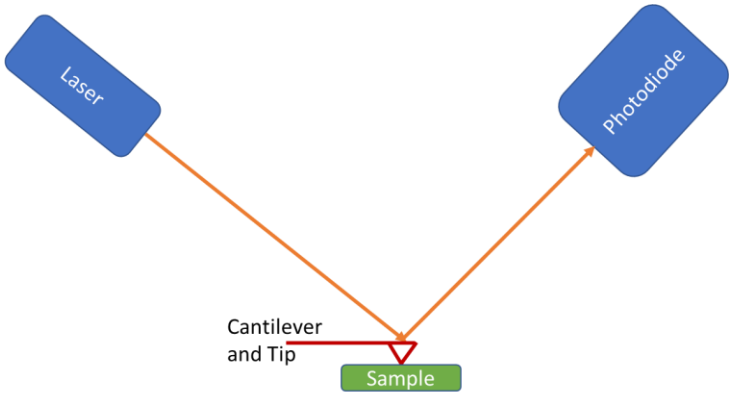

Figure 4-2: *Simplified diagram of an AFM set-up*

4.3 Results and discussion

4.3.1 Study of $PC_{60}BM$ concentration dependence in ZZ115

A first series of measurements were done using UVVIS spectroscopy to ascertain the effects of fullerene variation on the blend absorbance. Sample preparation was performed according to the details in appendix **Table A-2**.

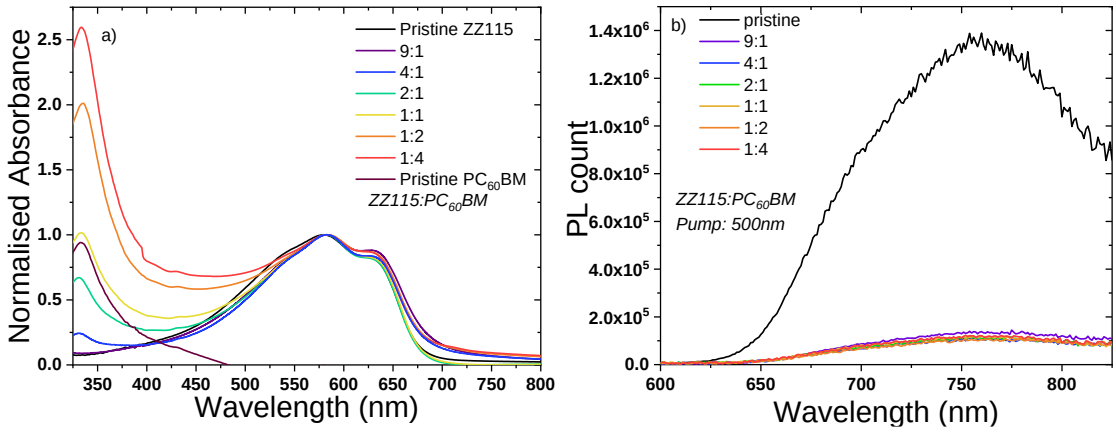

Figure 4-3: a) *Normalised ground state absorbance spectra of ZZ115:$PC_{60}BM$ samples, pristine ZZ115 and $PC_{60}BM$ at different blend ratios. Spectrum normalised to 580 nm peak.* ***b)*** *Photoluminescence spectra of ZZ115:$PC_{60}BM$ samples and pristine ZZ115*

ZZ115 pristine absorbance is characterised and described in Chapter **3** section **3.2.3**. ZZ115 appears to fluctuate in crystallinity (seen in the 575 nm peak fluctuation in ***Figure 4-3a***) with fullerene loading but no consistent pattern can be discerned. As such it can be postulated that these variations are due to variance in the sample preparation process, causing the samples to have slightly varying morphologies. The degree of variation should not be significant enough to substantially affect the TAS measurements. The lack of major variation however suggests the fact that the fullerene does not influence the morphology of the ZZ115 based phases implying $PC_{60}BM$ has a primarily electronic and energetic influence on the transient features of ZZ115. The invariance is unusual as a similar study by Keivanidis *et al.* [29]on P3HT:$PC_{60}BM$ found a much more significant change in absorbance with $PC_{60}BM$ concentration variation even on the annealed version. As such the underlying morphological effect of $PC_{60}BM$ on the donor molecule should be different in ZZ115 than on P3HT, possibly explaining the observed kinetic differences as seen in Chapter

3 and suggesting non-Langevin bimolecular recombination behaviour is not purely tied to morphology.

The photoluminescence spectra of the ZZ115:$PC_{60}BM$ blends seen in ***Figure 4-3b*** show little difference with fullerene loading. Pristine ZZ115 possesses a Stokes shift of around 0.17 eV which is quite a significant shift compared to other OPV molecules such as P3HT[30]only showing a Stokes shift of around 0.07 eV. As previously discussed in Chapter **3** the high Stokes shift of ZZ115 suggests a complex relaxation pathway. The lack of change in ZZ115 stokes shift with fullerene loading suggests however that the overall vibrational profile of ZZ115 does not change in blend.

A key observation is the impact of PL quenching with addition of $PC_{60}BM$, with a 10% fullerene loading leading to a 90% PL quenching. Further increase in fullerene concentration leads to a slightly larger PL quenching to around 94-95% quenching but no discernible trend is observed with fullerene variation. Such a large PL quenching even at low $PC_{60}BM$ loading highlights the efficiency in quenching for ZZ115 and the important influence of $PC_{60}BM$ on exciton dynamics. This observation is consistent with the lack of change in absorbance with $PC_{60}BM$ loading. As such a small distinctive difference in exciton quenching behaviour between the 10% addition and the other blends is hinted at, which could translate to two different emission regimes occurring in ZZ115:$PC_{60}BM$ blends. This potential two blend regime system is not quite observed in the aforementioned P3HT study by Keivanidis *et al.* [29]. The annealed P3HT saw a reduced quenching at 10% fullerene but the extent of quenching was significantly reduced (50% compared to 90% here), and the P3HT PL quenching saw a trend of increased quenching with increased fullerene concentration. As the difference is within uncertainty range however the observed difference may be simply experimental error. Regardless the lack of major variance in both absorbance and PL measurements with fullerene concentration suggests a lack of change in underlying morphology with fullerene loading. On the other hand, the heavy quenching even at low fullerene loadings of 10% suggests a highly favourable donor-acceptor interface and fast exciton recombination dynamics. From the absorbance spectrum, the excitation wavelength of 500 nm was chosen for TAS

measurements on ZZ115:$PC_{60}BM$ samples for similar reasons as for pristine ZZ115 and the measurements performed in Chapter **3**.

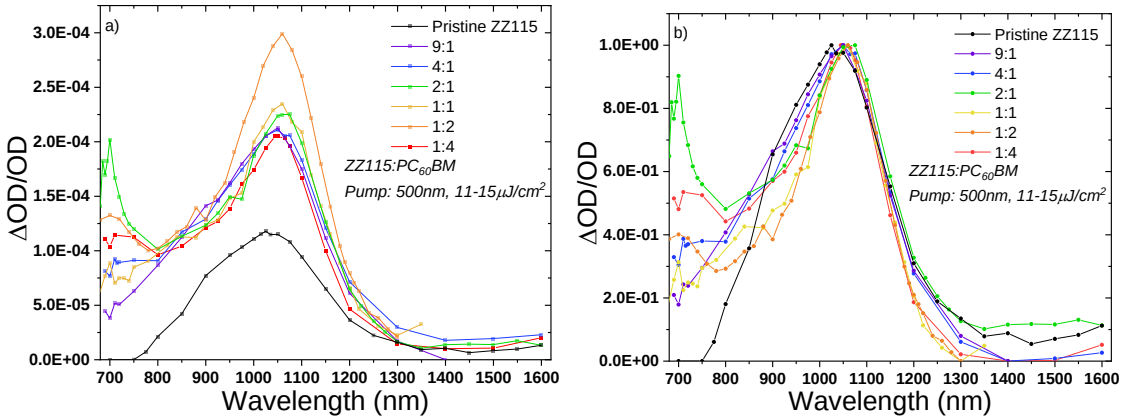

Figure 4-4: a) *Transient absorption spectrum and* ***b)*** *normalised Transient absorption spectrum of ZZ115:$PC_{60}BM$ samples at 1 μs Measurements taken at 500 nm excitation wavelength and with an 11 to 15 uJ/cm² excitation energy density. Spectrum is normalised for absorbance*

The pristine ZZ115 TA spectrum, given in more detail in ***Figure 3-3***, shows a single broad peak centred on the 1025 nm wavelength. The introduction of $PC_{60}BM$ as seen in ***Figure 4-4*** leads to the formation of a second peak around 700 nm with the intensity increasing until 33% (2:1 blend) fullerene. Notably the intensity of the 700 nm peak appears independent of the 1100nm peak as highlighted ***Figure 4-4b***. The 1025-1050 nm peak remains present for all blend ratios; however, it appears to shift slightly by around 25 nm with introduction of $PC_{60}BM$ content as mentioned in Chapter **3**. The 1050 nm peak shift is consistent and seemingly independent of fullerene concentration. Both blend features behave differently with fullerene concentration variation, suggesting different origins and therefore natures. The 1100 nm peak amplitude is at its lowest at the pristine ZZ115, three times lower than the 1:2 blend and close to two times lower than the other blends. The significantly higher ΔOD signal of the 1:2 blend vs the other blends, denoting a higher charge carrier concentration, is consistent with the ideal device blend ratio of 1:2 and suggests the key polaron for efficient device performance lies in the 1100 nm feature.

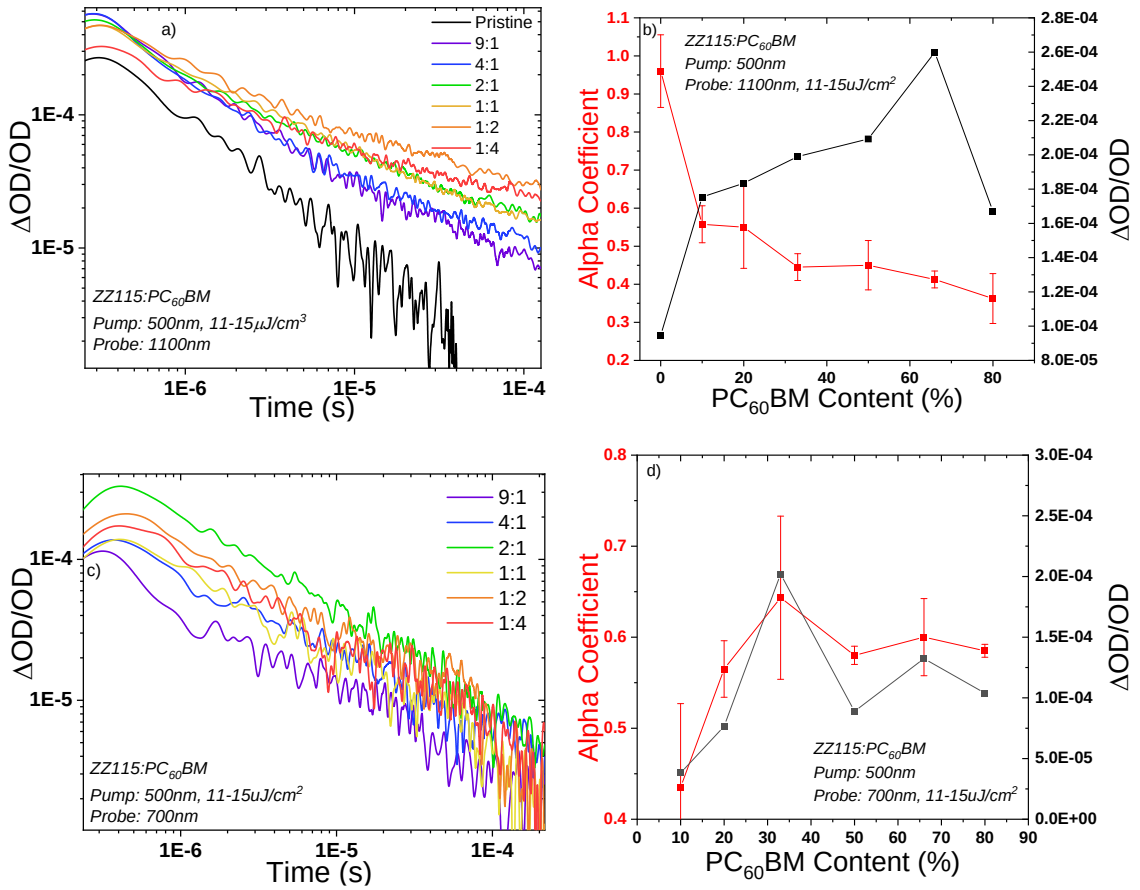

Figure 4-5: *Transient absorption kinetics for ZZ115:PC60BM samples at different blend ratios. Kinetics were normalised by photons absorbed and measured at 500 nm excitation wavelength, with energy density dependent hovering around 12 uJ/cm² and at probe wavelength* ***a)*** *1100 nm and* ***b)*** *700 nm. Mean of different alpha coefficients measured for each ZZ115 sample and the deviation of measurements recorded. at probe wavelength* ***c)*** *1100 nm and* ***d)*** *700 nm*

An initial hypothesis postulated in Chapter **3** section **3.2.2** identified the 1100 nm peak as the ZZ115 polaron in a ZZ115 crystalline medium and the 700 nm peak as the ZZ115 polaron in a mixed amorphous medium. 1100 nm probe decay dynamics seen in ***Figure 4-5a*** show a clear difference between the pristine ZZ115 sample and the blend samples. Increasing the PC60BM content appears to slow down the kinetics as highlighted by ***Figure 4-5b*** with the measured alpha coefficient going from 0.55 at 10% fullerene (9:1 blend) to 0.42 at 66% fullerene (1:2 blend). The trend inversely follows the observed intensity trend found in ***Figure 4-5a*** until over 66% fullerene content (1:2 blend) is reached, at which point the intensity drops by half. It appears thus that an increased PC60BM concentration could lead to a higher density of traps and hence slower kinetics within crystalline ZZ115 domains.

The 700 nm feature seen in ***Figure 4-5c-d*** seems to have much more homogenous kinetics, with α averaging a value of 0.6 past a saturation point of 33% fullerene concentration (2:1 blend). Notably the kinetics are faster for the higher blend ratios compared to 1100 nm probe wavelength measurements with an alpha of 0.6 found for the 700 nm feature at the 80% (1:4 blend) while the 1100 nm feature has an alpha of 0.4. The recombination process appears to still be trap limited but to a lesser degree, suggesting the polaron recombining in a mixed amorphous phase. The close to 1-to-1 correspondence between the alpha and ΔOD coupled with the inexistence of the 700 nm feature in pristine ZZ115 further suggests the recombination occurring in a mixed amorphous phase. At low fullerene loadings (10%) the mixed amorphous phase would exist but at very small sizes owning from the likely strict mixed phase composition, similar to the 3:7 ratio seen in P3HT:$PC_{60}BM$ mixed amorphous phases[31]. The small domain sizes with proximity to pure polymer domains would possibly lead to the slower kinetics (with a measured alpha of 0.45 for the 9:1 blend) due to charge heterogeneity. Higher fullerene loadings (33%) would lead to larger mixed domain until an optimal composition is reached balancing polymer concentration and D/A interface. Kinetics become faster due to increased domain sizes and increased donor/acceptor interface thereby increasing the probability of charges recombining due to finding said interface. Importantly the trap depth remains constant past the maximum as the medium does not change significantly from an energy level perspective and the level of purity remains constant, and with it the trap depth. This hypothesis is consistent with previous work done on ZZ115:$PC_{60}BM$ [32-34]showing the material system to form amorphous regions as well as with studies finding dual polaron features in other OPV material systems[35].

4.3.2 Study of $PC_{70}BM$ concentration dependence in ZZ115

As with the $PC_{60}BM$ study, ZZ115:$PC_{70}BM$ was studied using UV-VIS to ascertain sample quality and the effect of fullerene concentration variation.

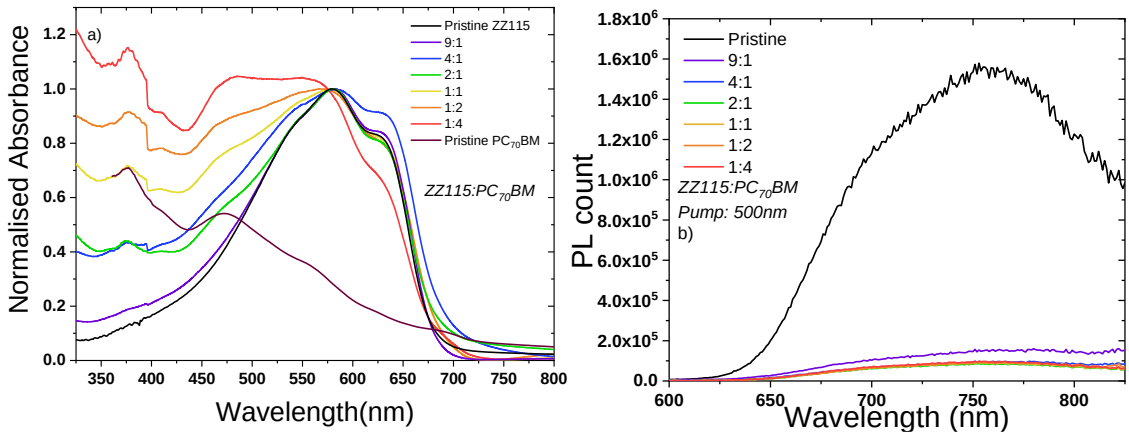

Figure 4-6: a) *Normalised ground state absorbance spectra of ZZ115:$PC_{70}BM$ samples, pristine ZZ115 and pristine $PC_{70}BM$ at different blend ratios. The spectrum was normalised to the 580 nm peak.* ***b)*** *Photoluminescence spectra of ZZ115:$PC_{70}BM$ samples and the pristine ZZ115.*

Looking at the variation in $PC_{70}BM$ content with UV-VIS and PL spectroscopy as seen in ***Figure 4-6***, similar observations to ZZ115:$PC_{60}BM$ systems can be made as described with ***Figure 4-3***. Considering the established kinetic differences in Chapter **3** between $PC_{60}BM$ and $PC_{70}BM$, the lack of variation reinforces the hypothesis of the fullerene not influencing the morphology of the ZZ115 phases. As with $PC_{60}BM$, the addition of $PC_{70}BM$ to ZZ115 leads to PL quenching regardless of the blend ratio. 10% fullerene content results in 90% quenching as seen by ***Figure 4-6b*** and further fullerene loadings lead 94%-95% quenching. The same observations and hypothesis for ZZ115:$PC_{60}BM$ would apply to ZZ115:$PC_{70}BM$ and would suggest that possible differences owing to different miscibility in ZZ115, not observed but reported in P3HT[36], do not have an influence on the overall morphology and vibronic structure of ZZ115.

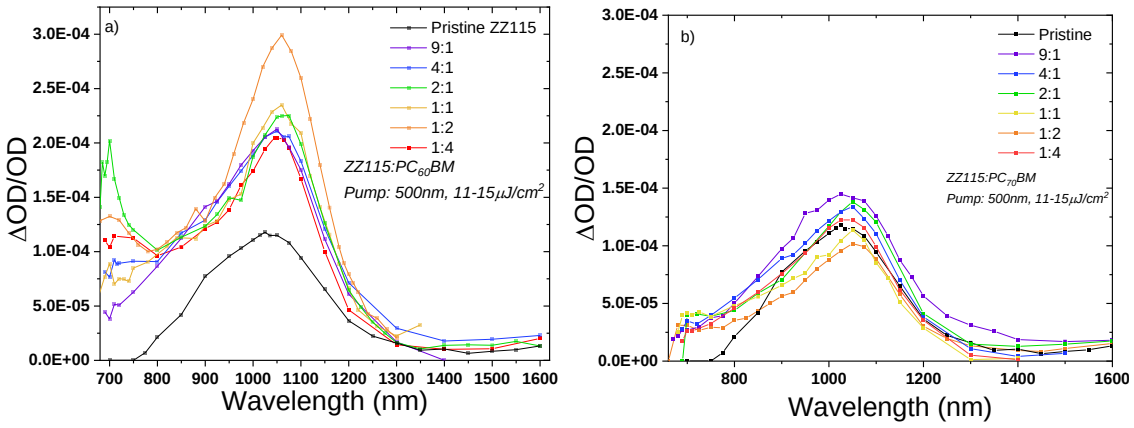

Figure 4-7: *Transient absorption spectrum of* ***a)*** *ZZ115:PC60BM and* ***b)*** *ZZ115:PC70BM samples at 1 μs timescale. Measurements taken at 500 nm excitation wavelength and with an 11 to 15 uJ/cm² excitation energy density. Spectrum is normalised for absorbance*

Changing the acceptor from PC60BM to PC70BM for ZZ115 does indeed seem to lead to changes in the TA spectrum in terms of features observed. As with ZZ115:PC60BM, two transient features at 1100 nm and 700 nm are observed but with significant changes in amplitude. As initially observed in ***Figure 3-10:*** Transient absorption spectra of ZZ115 pristine, ZZ115:PC60BM samples and ZZ115:PC70BM samples at a (1:2) blend ratio at 1 μs, and 10 μs timescale. Measurements were taken at 500 nm excitation wavelengths and with an 11-13 uJ/cm2 excitation energy density. The spectrum is adjusted for photons absorbed. the PC70BM blends produces significantly less charges than the PC60BM blends. Certain blend ratios remain quite comparable in amplitude at the 1100 nm peak (for the 2:1 ratio, the PC60BM based has an amplitude of 2×10^{-4} while PC70BM has 1.9×10^{-4}) but overall a lack of trend is seen in 1100nm amplitude for PC70BM based samples at the 1 μs timescale. The key difference between the two fullerene spectra lies in the intensity of the 1:2 blend ratio for ZZ115:PC60BM seeing a signal around 1.75 times higher. It is possible that such an optimal ratio does not exist to the same extent for ZZ115:PC70BM. The central main ZZ115 feature in the 1050 nm peak appears unchanged however in terms of shift with fullerene loading compared to PC60BM. The 700nm feature on the other hand is greatly reduced in amplitude for all blends compared to PC60BM based samples (for the 1:1 blend ratio ZZ115:PC70BM sees $\Delta OD=5\times10^{-5}$compared to $\Delta OD=1.75\times10^{-4}$ for ZZ115:PC60BM). This reduction in amplitude of the 700 nm feature may be due to the

absorbance spectra of $PC_{70}BM$[37] having a longer feature extending to the 700 nm range, thus overlapping with the 700 nm TAS feature and potentially supressing it. The fact that the 700 nm feature remains visible could hint at this 700 nm feature being very prominent but centred on a lower wavelength such 650 nm. Regardless the similarities in the spectrum in terms of features found could suggest that the features are very similar as previously discussed in Chapter **3.**

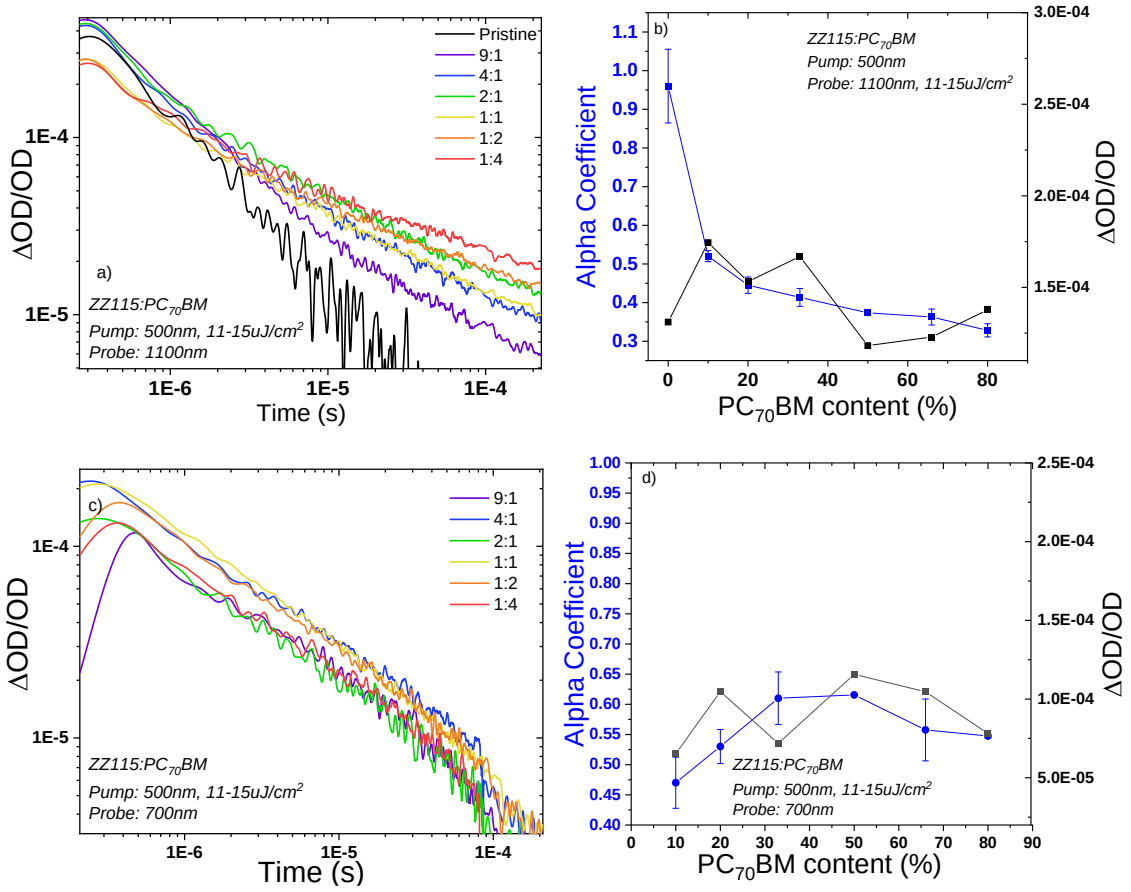

Figure 4-8: *Transient absorption kinetics for ZZ115:$PC_{70}BM$ samples at different blend ratios. Kinetics were normalised by photons absorbed and measured at 500 nm excitation wavelength, with energy density dependent hovering around 12 uJ/cm² and at probe wavelength:* ***a)*** *1100 nm or* ***c)*** *700nm. Mean of different alpha coefficients measured for each ZZ115 sample and the deviation of measurements recorded for the* ***b)*** *1100 nm or* ***d)*** *700nm.*

As with $PC_{60}BM$, $PC_{70}BM$ based samples show a consistent decrease in kinetics with fullerene content variation though $PC_{70}BM$ appears to have slightly slower recombination kinetics than $PC_{60}BM$ at the 1100 nm probe wavelength (0.42 for $PC_{60}BM$ vs 0.34 for $PC_{70}BM$ for the 1:2 blend). The slower kinetics does suggest a difference between the two fullerene blends, highlighted and discussed in more detail with ***Figure 4-9***. The difference in amplitude trend between the two fullerene blends

first seen in ***Figure 4-7*** is highlighted in ***Figure 4-8b*** with a very different charge generation trend observed as instead the amplitude follows the kinetics relatively closely.

Shifting the probe wavelength to 700 nm however leads to similar alpha values between $PC_{70}BM$ and $PC_{60}BM$ with faster kinetics than the 1100nm wavelength feature and discussed in more detail with ***Figure 4-9***. In contrast to the 1100 nm the amplitude follows overall the same trend as ZZ115:PC60BM, suggesting a much closer similarity between the two fullerenes for this transient feature as compared to the 1100 nm feature.

4.3.3 Blend kinetic comparison

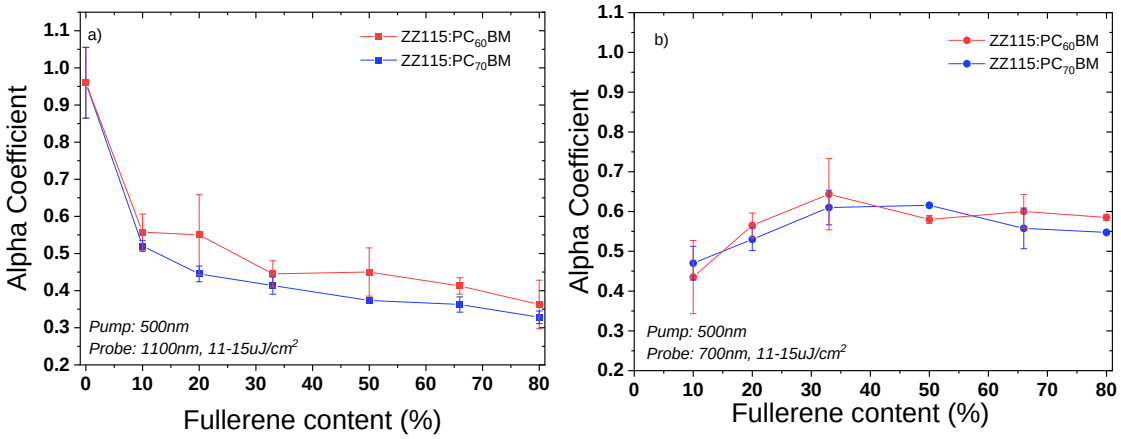

Figure 4-9: *Average measurement of the alpha coefficient of the TA kinetics for ZZ115:$PC_{60}BM$ (blue) and ZZ115$_{70}$BM (red) samples against fullerene concentration. Measurements were taken at* ***a)*** *1100 nm probe wavelength while* ***b)*** *shows measurements taken at 700 nm probe wavelength.*

As summarised by ***Figure 4-9***, the kinetics of both fullerene acceptors follow a similar trend at both probe wavelengths. The downward trend of the 1100nm alphas (***Figure 4-9a***) would suggest that $PC_{70}BM$ samples are similar in properties and structure to $PC_{60}BM$ samples but with deeper traps and thus slower kinetics. The difference in kinetics between the two acceptors reinforces the previously mentioned assignment of ZZ115 polaron in ZZ115 crystalline region, as the larger $PC_{70}BM$ molecule would disrupt the interchain distance between ZZ115 molecules more than $PC_{60}BM$, in a similar manner to ICBA and ICTA seen in our previous paper[38].

In contrast, at the 700 nm probe wavelength (***Figure 4-9b***) the kinetic traces are virtually identical between the two fullerene systems. These findings reinforce the

hypothesis that the 700 nm wavelength feature for ZZ115:$PC_{60}BM$ is the delocalised ZZ115 polaron recombining in a mixed amorphous phase, as the recombination is seemingly independent of the exact medium it takes place ($PC_{60}BM$ or $PC_{70}BM$). Crucially the 10% fullerene is the slowest blend ratio. This clear difference compared to the other blend ratios coincides with the blend ratio supposedly having the smallest mixed amorphous regions. As such this intermediary point acts as a validation of the theory due to the mixed amorphous domains possibly not being fully formed at this fullerene content. While no studies have examined mixed amorphous domains in great detail for ZZ115, P3HT was found to form mixed amorphous region with a mixed domain composition of 3:7 P3HT:$PC_{60}BM$ ratio[31]. While ZZ115 may not form domains at such a ratio, it is possible a similar ratio occurs for ZZ115 and due to this these domains cannot fully form at 10% fullerene.

A similar method to that of Chapter **3** section **3.3** was used for additional calculations of the bimolecular recombination coefficient and lifetime, with the final calculated reaction order given in ***Figure 4-10***.

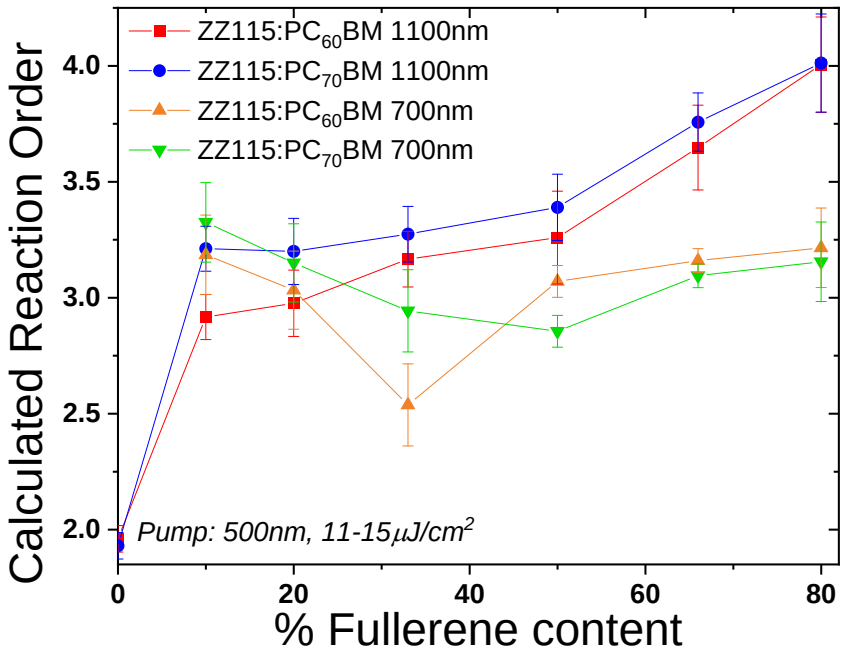

Figure 4-10: *Summary of calculated reaction orders against fullerene content from the kinetics of all the ZZ115:$PC_{60}BM$ blends and ZZ115:$PC_{70}BM$ at 1100 nm and 700 nm probe wavelength.*

A look at the reaction orders calculated from TAS kinetics as seen in ***Figure 4-10*** highlights the difference in ZZ115 polaron features found in the ZZ115:fullerene

blends. The 1100 nm polaron for both fullerene blends has a reaction order of around 3 at the 10% fullerene content (9:1 blend), increasing linearly with fullerene content until a reaction order of around 4 at the 80% fullerene content (1:4 blend). The ZZ115:$PC_{70}BM$ blends also sees a slightly higher reaction order across the range of fullerene variation (3.2 for ZZ115:$PC_{70}BM$ vs 2.9 for ZZ115:$PC_{60}BM$). Conversely the 700 nm polaron sees once again a reaction order of around 3 at the 10% fullerene content (9:1 blend) for both fullerene blends but increased fullerene loading does not lead to a significant change in reaction order. The main exception lies in in the 2:1 ZZ115:$PC_{60}BM$ blend which sees a reduction in reaction order to around 2.5.

As the initial hypothesis placed this feature as the ZZ115 polaron recombining in a mixed amorphous phase, it would be expected that a change in fullerene concentration would lead to changes in transient properties. This lack of variance however strongly hints at the delocalised nature of the ZZ115 polaron feature within this domain and suggests, as mentioned before, that an increase in fullerene concentration only increases the size of this domain, and possibly increases pure fullerene domains, but does not significantly alter the mixed amorphous domain. The relatively static reaction order of around 3 appears to confirm this model[39] as mentioned previously.

4.4 Supplementary measurements

While TAS is a powerful technique to model characterise bimolecular recombination, additional techniques were used by collaborators to provide further insight in the measured features and especially the 1100 nm feature.

4.4.1 Picosecond TAS

Measurements at earlier timescales were performed in order to clarify the nature of the observed spectral transient features on a pristine ZZ115 film, 9:1 ZZ115:$PC_{60}BM$ blend and 1:2 ZZ115:$PC_{60}BM$ blend due to time and logistical considerations. Firstly, a spectrum was constructed as shown in ***Figure 4-11*** at various timescales.

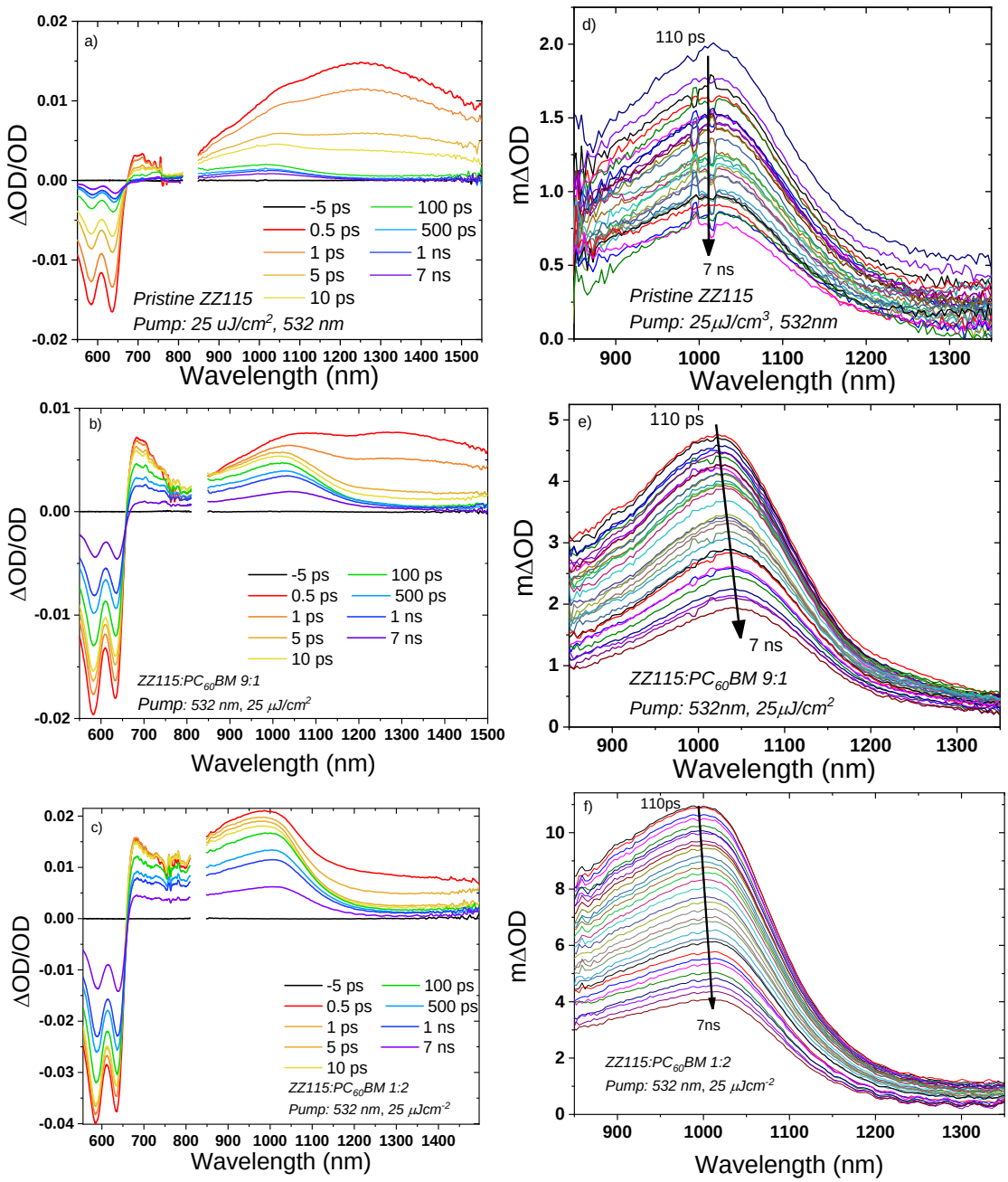

Figure 4-11*Ultrafast TA spectrum on the* ***a)*** *pristine ZZ115,* ***b)*** *9:1 blend and* ***c)*** *1:2 blend for different timescales, all measured at 532 nm wavelength and 25 μJ/cm². Included also is a highlight of the shift in 1020 nm polaron peak with increasing timescale for the* ***e)*** *pristine ZZ115,* ***f)*** *9:1 blend,* ***g)*** *1:2 blend. Measurements were done at the Lord Porter Laboratory, University of Sheffield by Jose Marin Beloqui and Tracey Clarke.*

All spectra show several significant findings at the ps timescale compared to the μs timescale. As expected, the ground state bleach causes a negative signal to be observed until the 700 nm wavelength. A very significant peak is seen around the 1250 nm wavelength for the pristine, is present to a lesser extent in the 9:1 blend and very minor in the 1:2 blend. This feature in all cases disappears completely at longer

timescales, assigning it as the ZZ115 exciton. Adjacently, a shoulder is seen in the pristine at the 1020 nm wavelength that becomes a distinct peak in the blend films. Notably this peak remains at longer timescales which is consistent with earlier microsecond measurements assigning the feature as the ZZ115 polaron, but more importantly a noticeable red shift of 20-25 nm occurs in the blend films and not the pristine. The extent of the shift however appears to be identical for the 9:1 and the 1:2 blend and is consistent with previous measurements on the microsecond scale This significant red shift could allude to a progressive localisation of the ZZ115 polarons in the crystalline domain, with the identical shift in the different blend ratios highlighting the shift's independence in fullerene concentration. The 20-25 nm red shift is also observed on the microsecond timescale and remains the same shift at the longer timescales, reinforcing the assignment as the ZZ115 polaron. It would thus appear that the ZZ115 exciton decays from 1250 nm leaving only the polaron feature at 1020 nm. A 700 nm peak appears in the pristine but disappears after 100 ps in contrast to the blends where this peak remains at longer timescales. Quite noticeable is the intensity of the 700 nm peak being much greater in the 1:2 blend when compared to 9:1 blend, all of which is consistent with microsecond data.

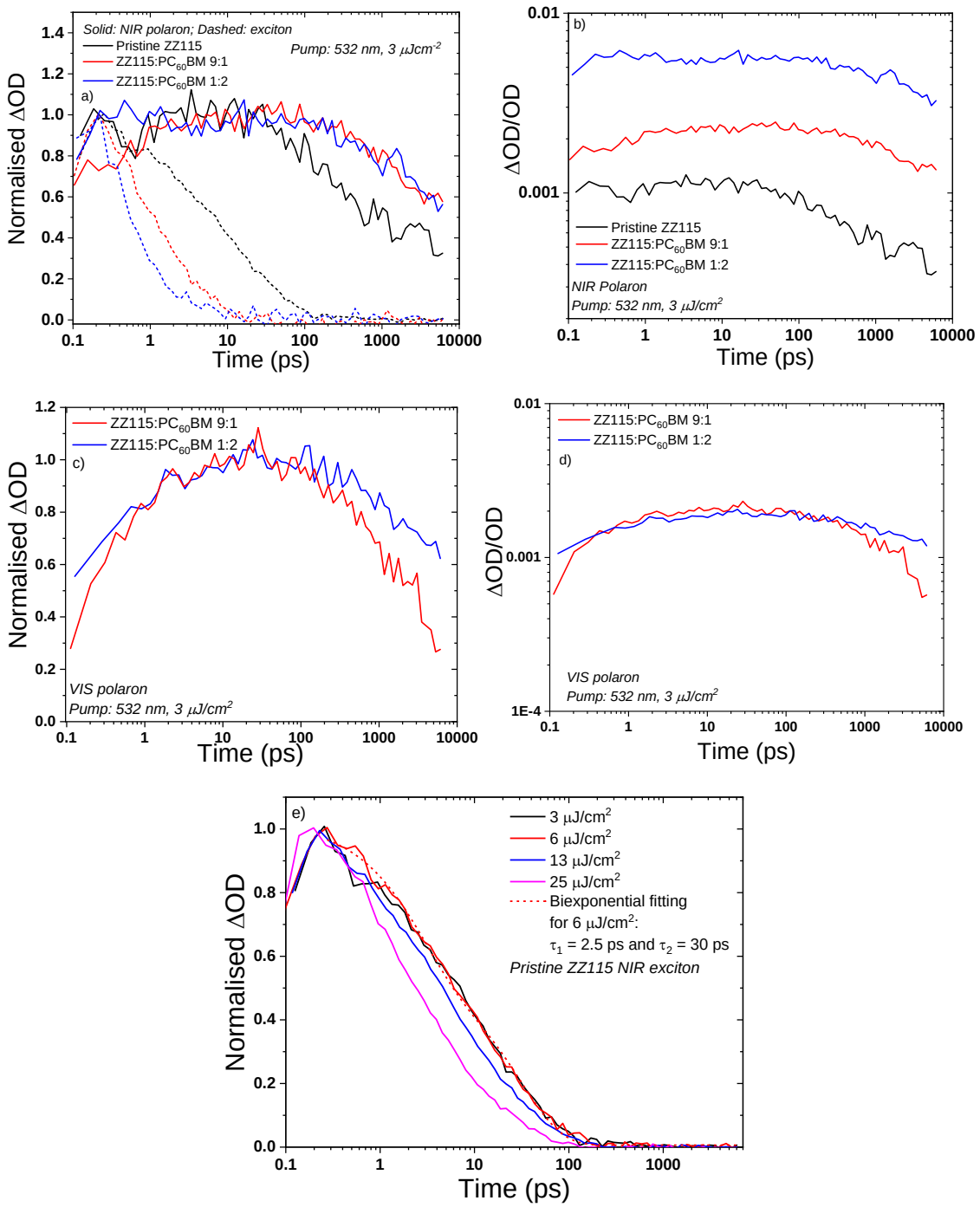

Figure 4-12: *Ultrafast TA global analysis kinetics on the pristine ZZ115, 9:1 blend and 1:2 blend measured at 532 nm wavelength and 25 μJ/cm² with* ***a)*** *normalised kinetics at the NIR with both extrapolated polaron (solid lines) and exciton (dashed lines) features, and* ***b)*** *kinetics with extrapolated NIR polaron traces non normalised,* ***c)*** *normalised kinetics at the VIS for the extrapolated polaron and* ***d)*** *kinetics with extrapolated VIS polaron traces non normalised.* ***e)*** *excitation density dependence of ΔOD for pristine ZZ115 with biexponential fitting Measurements were done at the Lord Porter Laboratory, University of Sheffield by Jose Marin Beloqui and Tracey Clarke.*

A kinetic assessment of the NIR features achieved through global analysis, shows the exciton decay following a biexponential decay for all systems. The addition of 10%

$PC_{60}BM$ leads to faster kinetics as seen in ***Figure 4-12a*** as the exciton becomes quenched**.** Further addition of fullerene leads to a greater quenching of the exciton as shown by the 1:2 blend dashed trace compared to the 9:1 trace. The presence of this biexponential decay at such a low excitation density is notable, with pristine ZZ115 exhibiting no change in decays at higher energies and no sign of monomolecular activity. The pristine exciton can therefore be assigned to two decay pathways. Exciton relaxation would occur at 30 ps while the faster exciton dissociation would occur at the 2.5 ps. In contrast the faster exciton kinetics of the blends suggest little to no relaxation, with the main exciton pathway being exciton dissociation.

Conversely, the polaron dynamics show quite notable differences between the three blends. The pristine sees a constant polaron population until exciton decay significantly around 40 ps, at which point the polaron starts decaying. This heavily suggest geminate recombination within pristine ZZ115 at the ps timescale, followed by bimolecular recombination at the μs timescale. In contrast the 9:1 sees the NIR polaron population increase by 20% before decaying after 200 ps, attributed to a close to one-to-one correspondence of exciton dissociation and increased polaron population, with little evidence of geminate recombination. Finally, the 1:2 blend has a long lived high polaron population (close to 2-3 times the population of the 9:1) in line with previous μs TAS. The lack of increase in polaron population highlights the presence of new and more complex pathways (such as CT states) to polaron generation stemming from the increased presence of the fullerene.

In contrast to the VIS polaron population follows a parabola with the 9:1 blend polaron population diminishing up to 30% from its peak while the 1:2 blend only diminishes to 70%, illustrated by ***Figure 4-12c***. The rise and fall unfortunately could be attributed to several processes occurring at this wavelength region, such as ground state bleach, but the differing extent of population decrease could illustrate the differing size of the mixed amorphous phase within the 9:1 blend as compared to the 1:2 blend.

While the bimolecular recombination kinetics are primarily observed on a microsecond scale, picosecond measurements are vital for exciton measurements and

serve as a confirmation of the previous attribution of polaron recombination found in microsecond measurements.

4.4.2 AFM

A final set of measurements was done to ascertain the surface morphology of the material systems. The measurements were done in two sets with the first done on pristine ZZ115 and blends with $PC_{60}BM$, ICMA, ICBA and ICTA at the 9:1 ratio while the second was done on blends of ZZ115 with $PC_{60}BM$ and $PC_{70}BM$ at the 1:2 ratio. The resulting images of the two sets can be seen in ***Figure 4-13***.

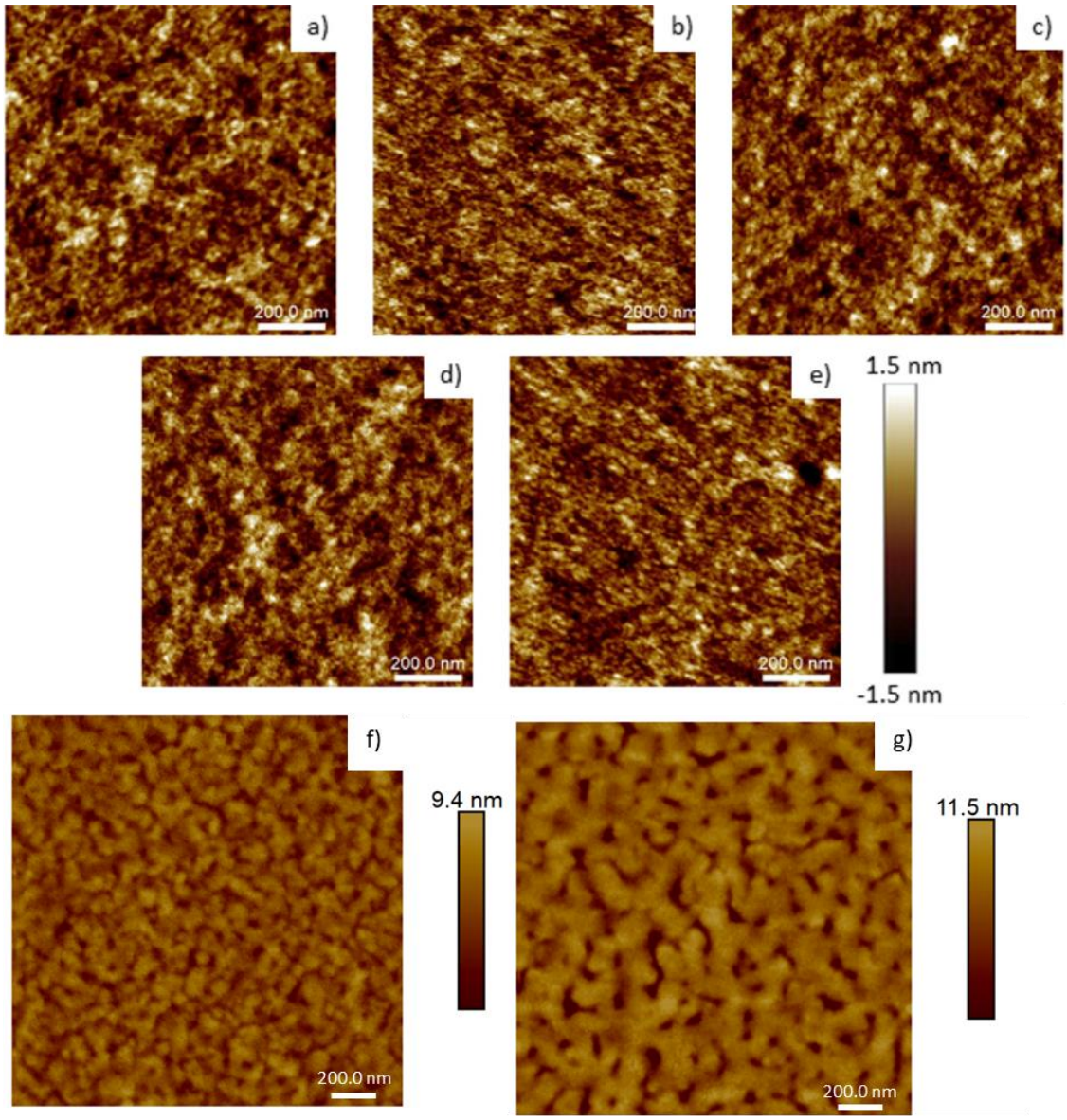

Figure 4-13: *AFM images of* ***a)*** *pristine ZZ115,* ***b)*** *ZZ115:$PC_{60}BM$,* ***c)*** *ZZ115:ICMA,* ***d)*** *ZZ115:ICBA, and* ***e)*** *ZZ115:ICTA films, where the blends all have 9:1 by weight ratios. AFM images of* ***f)*** *ZZ115:$PC_{60}BM$ and* ***g)*** *ZZ115:$PC_{70}BM$ with blends at a 1:2 weight ratio. Measurements done by Jose Marin-Beloqui and Junjun Guo.*

A first initial addition of fullerene was found to have little to no effect on the overall morphology regardless of the acceptor. The R_a values, the average of the absolute values of the surface height deviations measured from the mean plane, vary from 0.352 nm and 0.368 nm across the blends and being close to that of the pristine at 0.355 nm. While there is a possibility that molecular size changes such as molecule orientations may be missed, it is more likely that the first initial change in kinetics (α=1 in the pristine at 1100 nm compared to α=0.55 for the 9:1 blend) observed after introduction of fullerene is not a result of morphological changes within the system. In contrast, significant introduction of fullerene leads to a drastic change in morphology with increased measured R_a values of 1.3 nm for $PC_{60}BM$ 1:2 blend and 2.1 nm for $PC_{70}BM$ 1:2 blend. The very clear difference between the two fullerenes can be explained by the increased size of the $PC_{70}BM$. As the $PC_{70}BM$ is a larger molecule it could have a reduced miscibility in ZZ115, leading it to form larger pure fullerene domains or aggregates and therefore an increased R_a. A similar phenomenon to that observed in this study was reported for P3HT[36] and other donor molecules[40]. The observed differences in morphology are in line with the observations of slight kinetic differences between the two acceptors, as well as the reduced number of generated charges in $PC_{70}BM$ based samples in comparison to $PC_{60}BM$ based samples. The reduction in generated charges could be now attributed to the worse donor-acceptor interface stemming from reduced miscibility evidenced by ***Figure 4-13f-g.*** The worse donor-acceptor interface would be due to the pure $PC_{70}BM$ fullerene domains being larger which would explain the notable differences in morphology observed in ***Figure 4-13f*** and ***Figure 4-13g***.

4.5 Overall Discussion

Chapter **3** of this thesis identified: a ZZ115 polaron in a crystalline ZZ115 medium within pristine ZZ115, a ZZ115 polaron in a crystalline ZZ115 medium within ZZ115:$PC_{60}BM$ and ZZ115:$PC_{70}BM$ blends, and a ZZ115 polaron in a mixed amorphous domain within ZZ115:$PC_{60}BM$ and ZZ115:$PC_{70}BM$ blends. In this chapter, a series of measurements, using UVVIS, PL, ps-TAS, μs-TAS and AFM, was performed

on ZZ115 based blend samples with varying fullerene acceptor concentrations. These measurements aimed to expand on the hypotheses put forth by providing more insight as to the nature of the identified features. A summary of the established hypotheses regarding the influence of fullerene on ZZ115 is given in ***Figure 4-14***.

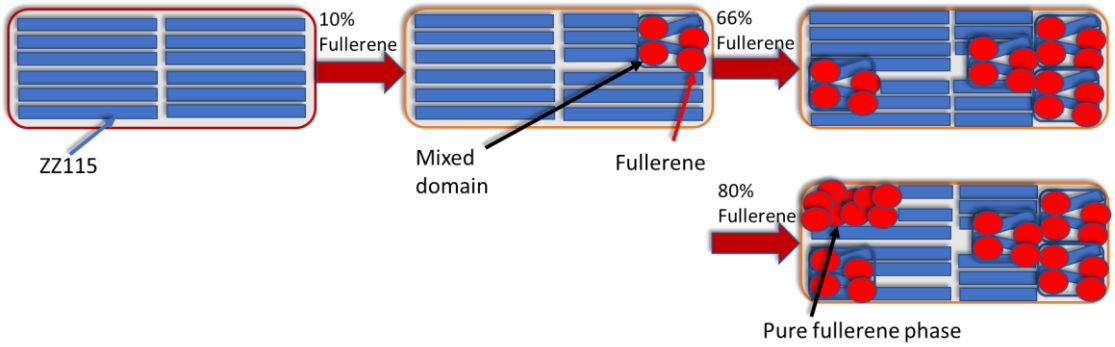

Figure 4-14: *Diagram visually representing established hypotheses for the effect of fullerene loading on ZZ115 films. Fullerene introduction in ZZ115 would first result in the formation of mixed domains. Further fullerene loading would increase the size of the mixed domains, leading to a more favourable donor-acceptor interface. Past an optimal composition, additional fullerene loading would lead to the formation of pure fullerene domains.*

Fullerene loading would thus have the following effect on ZZ115. ZZ115 pristine starts with semi-crystalline domains, with an abnormally high number of charges bimolecularly recombining due to an intragap state combined with a delocalised HOMO. At 10% fullerene, the ZZ115 crystalline phase is disrupted by the introduction of fullerene and formation of a mixed domain. The inherent intragap state inherent to ZZ115 and found to be present in many other materials[41]is replaced by fullerene induced CT states and the previously delocalised HOMO is now localised by the fullerene. At higher fullerene content the higher reaction order of the observed ZZ115 crystalline polarons would stem from a non-homogenous distribution of charge carriers, possibly due to aggregation at the more favourable donor-acceptor interface or possibly from increased ZZ115 interchain separation due to the presence of fullerene. The kinetic difference observed between $PC_{60}BM$ and $PC_{70}BM$ would be due to, in the first stage, $PC_{70}BM$ having a higher molecule size compared to $PC_{60}BM$ leading to increased localisation of the HOMO. As fullerene concentration is increased, the increased size of the $PC_{70}BM$ molecule would lead to

more pronounced traps within the ZZ115 crystalline phase formed from possible fullerene aggregation at the donor-acceptor interface.

Within this established hypothesised framework, the question remains as to what determines the optimal blend ratio in the ZZ115:fullerene system. For ZZ115:$PC_{60}BM$ the optimal blend ratio for device performance is the 1:2 ratio [32, 42-45]. Within this study the 1:2 ratio showed the highest number of recombining charges at close to 50% more recombining charges compared to other blends (seen in ***Figure 4-7***) while the bimolecular recombination kinetics are the second slowest out of all blend ratios. The 1:2 blend ratio was also found to display a rough morphology as seen in ***Figure 4-13f*** as compared to the smooth morphology of the 9:1 blend seen in ***Figure 4-13b***. The 1:2 blend should be composed of pure crystalline ZZ115 regions, pure fullerene regions (as evidenced by the high roughness found in AFM images in ***Figure 4-13f***) and an intermixed amorphous phase. The 1:2 fullerene concentration blend would lead to the optimal composition as it would strike a balance between a large enough ZZ115 concentration to form large enough pure donor phases (unlike the 80% blend), a large enough $PC_{60}BM$ concentration to form mixed amorphous domains (unlike the 10% blend) and formation fullerene aggregates within these mixed domains.

It is important to note that while the ZZ115:$PC_{60}BM$ has a clear optimal ratio from the literature and this present study, the same is not as evident for ZZ115:$PC_{70}BM$. Applying similar logic to the $PC_{60}BM$ blend would predict the 1:2 blend ratio to be the optimal choice ZZ115:$PC_{70}BM$. The lack of charges in comparison (as illustrated in Chapter **3** ***Figure 3-13)*** and the clearly larger fullerene domains (visible from ***Figure 4-13g***) highlight the importance of the donor/acceptor interface and the energy offset. As such the present hypothesis is that, while $PC_{70}BM$ should be able to morphologically replicate the circumstances that lead to the performance of ZZ115:$PC_{60}BM$, evidenced by the close to identical behaviour in UVVIS, PL and AFM behaviour, $PC_{70}BM$ has a higher localisation effect on the ZZ115 HOMO similar to previously reported effects by larger fullerenes than $PC_{60}BM$[38], resulting in a hampered charge generation, leading to the observed recombining charge intensities of ***Figure 4-7*** and ***Figure 4-8***.

Looking at a broader context, ZZ115 highlights the complexity of bimolecular recombination with two different features obeying different recombination regimes. More importantly the complexity of competing morphological and electronic effects arising from a variation in fullerene concentration was illustrated through a comparison between the acceptors $PC_{60}BM$ and $PC_{70}BM$. From an exploration into bimolecular recombination mechanics, the significant change between low acceptor concentration blends and higher ones was highlighted with a possible interplay between electronic disruption of the inherent donor properties and morphological effects on the different phases. While the structural order of the donor phase was found to play a critical part for reducing the bimolecular recombination factor[46, 47]in comprehensive studies on P3HT:$PC_{60}BM$, a balance between impeded bimolecular recombination and unimpeded charge generation and separation is necessary for optimal device performance.

4.6 Conclusion

A more in-depth study of the systems examined in Chapter **3** was performed as well as complemented by additional studies done thanks to collaborators. Firstly, a study of ZZ115 blended with $PC_{60}BM$ and $PC_{70}BM$ was done similar to that of chapter **3**, but with a variation in fullerene concentration. Parallel to this, additional measurements were done by collaborators using different methods to obtain key insights on specific properties such as the ZZ115 blend morphologies and pre microsecond transient features. On a first observation, an increase in fullerene loading within ZZ115:$PC_{60}BM$ and ZZ115:$PC_{70}BM$ leads to a general decrease in bimolecular recombination kinetics power law for the 1100 nm feature and no significant changes for the 700 nm feature past the addition of 10% fullerene. These observations result in an increasing calculated reaction order for the former feature and a close to stagnant reaction order for the latter feature. Supplementary measurements showed ps-TAS data serving as a confirmation of hypothesis established for the nature of the NIR polaron feature and AFM data providing insight on morphological evolution of fullerene concentration. The invariance of fullerene

on the assigned mixed amorphous bimolecular recombination kinetics speaks to the ZZ115 HOMO delocalisation in this domain as well as possibly the fixed composition of this phase with fullerene addition possibly only changing the domain size. Moreover, this chapter has served to confirm hypotheses on the NIR polaron feature established in chapter **3** with addition of fullerene affecting the ZZ115 crystalline region and leading to deeper traps, possibly due to a combination of DOS shape changing and charge carrier heterogeneity. Thus, this chapter highlighted the interplay between crystalline phases and mixed amorphous domains from a bimolecular recombination kinetic perspective. The exact underlying mechanism of each feature and the unusual behaviours found at the "optimal" blend ratio of 1:2 for both ZZ115:$PC_{60}BM$ and ZZ115:$PC_{70}BM$ still remain unclear but will be the focus of the next chapter.

4.7 References

1. I. Naik, R. Bhajantri, L. Naik, B. S. Patil, U. S. Pragasm, S. Rathod, and J. Naik, *Optically tuned poly (3-hexylthiophene-2,5-diyl) P3HT/PCBM (modified fullerene) blend for plastic solar cell.* Nanosystems: Physics, Chemistry, Matehmatics, 2016. **7**.
2. A. Supriyanto, A. Mustaqim, M. Agustin, A. H. Ramelan, Suyitno, E. S. Rosa, . . . F. Nurosyid, *Fabrication of organic solar cells with design blend P3HT: PCBM variation of mass ratio.* IOP Conference Series: Materials Science and Engineering, 2016.
3. Y. A. M. Ismail, T. Soga, and T. Jimbo, *Effect of Composition on Conjugation Structure and Energy Gap of P3HT:PCBM Organic Solar Cell.* International journal of New Horizons in Physics, 2015.
4. B. Kadem and A. Hassan, *The effect of fullerene derivatives ratio on P3HT-based organic solar cells.* Energy Procedia, 2015.
5. Z. Abada, A. Mellit, and M. Benghanem, *Influence of blend composition and annealing temperature on optical properties of organic photovoltaic cell*

based on P3HT:PCBM interpenetrating blend. International journal of Green Energy, 2019. **17**(1).

6. Kalonga, G., G. K. Chinyama, M.O. Munyati, and M. Maaza, *Characterization and optimization of poly (3-hexylthiophene-2, 5- diyl) (P3HT) and [6, 6] phenyl-C61-butyric acid methyl ester (PCBM) blends for optical absorption.* Journal of Chemical Engineening and Materials Science, 2013. **4**.
7. M. S. Ulum, E. Sesa, A. Nismayanti, and W. Belcher, *Donor acceptor ratio effect on P3HT:PCBM nanoparticulate organic photovoltaic device performance.* Journal of Physics: Conference Series, 2018.
8. S. Bi, Z. Ouyang, Q. Guo, and C. Jiang, *Performance enhancement by vertical morphology alteration of the active layer in organic solar cells.* Royal Society of Chemistry, 2018. **8**.
9. D. M. Schwaiger, W. Lohstroh, and P. M-Buschbaum, *The Influence of the Blend Ratio, Solvent Additive, and Post-production Treatment on the Polymer Dynamics in PTB7:PCBM Blend Films.* Macromolecules, 2021. **54**(13).
10. Z. He, C. Zhong, Z. Su, M. Xu, H. Wu, and Y. Cao, *Enhanced power-conversion efficiency in polymer solar cells using an inverted device structure.* Naturephotonics, 2012. **6**.
11. C. Liu, C. Yi, K. Wang, Y. Yang, R S. Bhatta, M. Tsige, . . . X. Gong, *Single-Junction Polymer Solar Cells with Over 10% Efficiency by a Novel Two-Dimensional Donor–Acceptor Conjugated Copolymer.* Applied Materials and Interfaces, 2015.
12. W. Huang, N. Chandrasekaran, S. K. K. Prasad, E. Gann, L. Thomsen, D. Kabra, . . . C. R. McNeill, *Impact of Fullerene Mixing Behavior on the Microstructure, Photophysics, and Device Performance of Polymer/Fullerene Solar Cells.* ACS Applied Materials and Interfaces, 2016. **8**(43).
13. D. W. Gehrig, I. A. Howard, S. Sweetnam, T. M. Burke, M. D. McGehee, and F. Laquai, *The Impact of Donor–Acceptor Phase Separation on the Charge Carrier Dynamics in pBTTT:PCBM Photovoltaic Blends.* Macromolecular Rapid Communications, 2015. **36**(11).

14. A. C. Mayer, M. F. Toney, S. R. Scully, J. Rivnay, C. J. Brabec, M. Schraber, . . . M. D. McGehee, *Bimolecular Crystals of Fullerenes in Conjugated Polymersand the Implications of Molecular Mixing for Solar Cells.* Advanced Functional Materials, 2009. **19**.
15. C. Zhang, S. Langner, A. V. Mumyatov, D. V. Anokhin, J. Min, J. D. Perea, . . . C.J. Brabec, *Understanding the correlation and balance between the miscibility and optoelectronic properties of polymer–fullerene solar cells.* Journal of Materials Chemistry A, 2017. **5**(33).
16. M. T. Sajjad, A. J. Ward, C. Kastner, A. Ruseckas, H. Hoppe, and I.D.W. Samuel, *Controlling Exciton Diffusion and Fullerene Distribution in Photovoltaic Blends by Side Chain Modification.* The Journal of Physical Chemistry Letters, 2015. **6**.
17. P. Westacott, J. R. Tumbleston, S. Shoaee, S. Fearn, J. H. Bannock, J. B. Gilchrist, . . . N. Stingelin, *On the role of intermixed phases in organic photovoltaic blends.* Energy and Environmental Science, 2013(9).
18. A. Pivrikas, N.S.S., G. Juška, and R. Österbacka, *A review of charge transport and recombination in polymer/fullerene organic solar cells.* Prog. Photovolt. , 2007. **15**: p. 677–696.
19. S. D. Oosterhout, V. Savikhin, J. Zhang, Y. Zhang, M. A. Burgers, S. R. Marder, . . . M.F. Toney, *Mixing Behavior in Small Molecule:Fullerene Organic Photovoltaics.* Chemistry of Materials, 2017. **29**(7).
20. D. Veldman, O. Ipek, S. C. J. Meskers, J. Sweelssen, M. M. Koetse, S. C. Veenstra, . . . R.A.J. Janssen, *Compositional and Electric Field Dependence of the Dissociation of Charge Transfer Excitons in Alternating Polyfluorene Copolymer/Fullerene Blends.* Journal of the American Chemical Society, 2008. **130**(24).
21. T. Ferron, M. Waldrip, M. Pope, and B.A. Collins, *Increased charge transfer state separation via reduced mixed phase interface in polymer solar cells.* Journal of Materials Chemistry A, 2019(9).
22. S. Mukherjee, C. M. Poctor, G. C. Bazan, T.-Q. Nguyen, and H. Ade, *Significance of Average Domain Purity and Mixed Domains on the*

Photovoltaic Performance of High-Efficiency Solution-Processed Small-Molecule BHJ Solar Cells. Advanced Energy Materials, 2015. **5**(21).

23. G. D'Avino, L. Muccioli, Y. Oliver, and D. Beljonne, *Charge Separation and Recombination at Polymer–Fullerene Heterojunctions: Delocalization and Hybridization Effects.* The Journal of Physical Chemistry Letters, 2015. **7**.
24. P. K. Nayak, K. L. Narasimhan, and D. Cahen, *Separating Charges at Organic Interfaces: Effects of Disorder, Hot States, and Electric Field.* The Journal of Physical Chemistry Letters, 2013. **4**(10).
25. H. Bassler and A. Kohler, *"Hot or cold": how do charge transfer states at the donor–acceptor interface of an organic solar cell dissociate?* Physical Chemistry Chemical Physics, 2015(43).
26. X.K. Chen, M. K. Ravva, H. Li, S. M. Ryno, and J.-L. Bredas, *Effect of Molecular Packing and Charge Delocalization on the Nonradiative Recombination of Charge-Transfer States in Organic Solar Cells.* Advanced energy Materials, 2016. **6**(24).
27. B. Gautam, E. Klump, X. Yi, I. Constantinou, N. Shewmon, A. Salehi, . . . F. So, *Increased Exciton Delocalization of Polymer upon Blending with Fullerene.* Advanced Materials, 2018. **30**(30).
28. V. Sudarsan, *Chapter 4 - Materials for Hostile Chemical Environments*, in *Materials under extreme conditions*, T. A. K and S. Banerjee, Editors. 2017, Elsevier.
29. P. E. Keivanidis, T. M. Clarke, S. Lilliu, T. Agostinelli, J. E. Macdonald, J. R. Durrant, . . . J. Nelson, *Dependence of Charge Separation Efficiency on Film Microstructure in Poly(3-hexylthiophene-2,5-diyl):[6,6]-Phenyl-C61 Butyric Acid Methyl Ester Blend Films.* The Journal of Chemical Physics Letters, 2010. **1**(4).
30. L. Wang and D. Beljonne, *Optical properties of regioregular poly(3-hexylthiophene) aggregates from fully atomistic investigations.* CrystEngComm, 2016(38).

31. A. J. Moule, *P3HT-based Solar Cells: structural properties and photovoltaic performances*, in *P3HT Revisited – From Molecular Scale to Solar Cell Devices*, S. Ludwigs, Editor. 2014. p. 199.

32. T. M. Clarke, C. Lungenschmied, J. Peet, N. Drolet, K. Sunahara, A. Furube, and A.J. Mozer, *Photodegradation in Encapsulated Silole-Based Polymer: PCBM Solar Cells Investigated using Transient Absorption Spectroscopy and Charge Extraction Measurements* Advanced Energy Materials, 2013. **3**: p. 1473-1483.

33. Scharber, M.C., *On the Efficiency Limit of Conjugated Polymer:Fullerene-Based Bulk Heterojunction Solar Cells.* Advanced materials, 2016. **28**(10).

34. S. Sweetnam, K. R. Graham, G. O. N. Ndjawa, T. Heumüller, J. A. Bartelt, T. M. Burke, . . . M.D. McGehee, *Characterization of the Polymer Energy Landscape in Polymer:Fullerene Bulk Heterojunctions with Pure and Mixed Phases.* Journal of the American Chemical Society, 2014. **136**: p. 14078–14088.

35. J. M. Marin-Beloqui, K. J. Fallon, H. Bronstein, and a.T.M. Clarke, *Discerning Bulk and Interfacial Polarons in a Dual Electron Donor/Acceptor Polymer.* J. Phys. Chem. Lett., 2019. **10**: p. 3813-3819.

36. F. Zhanga, Z. Zhuoa, J. Zhang, X. Wanga, X. Xua, Z. Wanga, . . . Y. Wang, *Influence of PC60BM or PC70BM as electron acceptor on the performance of polymer solar cells.* Solar Energy Materials & Solar Cells, 2011. **97**.

37. P. C. Y. Chow, S. Albert-Seifried, S. Gelinas, and R.H. Friend, *Nanosecond Intersystem Crossing Times in Fullerene Acceptors: Implications for Organic Photovoltaic Diodes.* Adv. Mater., 2014. **26**: p. 4851–4854.

38. J. Marin-Beloqui, G. Zhang, J. Guo, J. Shaikh, T. Wohrer, S. M. Hosseini, . . . T.M. Clarke, *Insight into the Origin of Trapping in Polymer/Fullerene Blends with a Systematic Alteration of the Fullerene to Higher Adducts.* The Journal of Physical Chemistry C, 2021. **126**(5): p. 2708–2719.

39. R. C. I. Mackenzie, T. Kirchartz, G. F. A. Dibb, and J. Nelson, *Modeling Nongeminate Recombination in P3HT:PCBM Solar Cells.* The journal of physical chemistry, 2011. **115**(19).

40. Y. He and Y. Li, *Fullerene derivative acceptors for high performance polymer solar cells* Phys. Chem. Chem. Phys., , 2011. **13**: p. 1970-1983

41. S. Zeiske, O. J. Sandberg, N. Zarrabi, W. Ki, P. Merdith, and A. Armin, *Direct observation of trap-assisted recombination in organic photovoltaic devices.* Nature Communications, 2021. **12**.

42. J. Peet, L. Wen, P. Byrne, S. Rodman, K. Forberich, Y. Shao, . . . D. Waller, *Bulk heterojunction solar cells with thick active layers and high fill factors enabled by a bithiophene-co-thiazolothiazole push-pull copolymer* Appl. Phys. Lett., 2011. **98**.

43. T. M. Clarke, D. B. Rodovsky, A. A. Herzing, J. Peet, G. Dennler, D. DeLongchamp, . . . A.J. Mozer, *Significantly Reduced Bimolecular Recombination in a Novel Silole-Based Polymer: Fullerene Blend.* Advanced Energy Materials, 2011. **1**(6).

44. T. M. Clarke, J. Peet, C. Lungenschmied, N. Drolet, X. Lu, B. M. Ocko, . . . M.A. Loi, *The role of emissive charge transfer states in two polymer–fullerene organic photovoltaic blends: tuning charge photogeneration through the use of processing additives.* Jounal of Materials Chaemistry A, 2014(31).

45. T. M. Clarke, C. Lungenschmied, J. Peet, N. Drolet, and A.J. Mozer, *Tuning Non-Langevin Recombination in an Organic Photovoltaic Blend Using a Processing Additive.* J. Phys. Chem. C., 2015. **119**.

46. L. Xu, J. Wang, and J. W. P. Hsu, *Structural Order: The Dominant Factor for Nongeminate Recombination in Organic Photovoltaic Devices.* The journal of Physical Chemistry C, 2017. **121**(17).

47. S. Wilken, D. Scheunemann, S. Dahlström, M. Nyman, J. Parisi, and R. Österbacka, *How to Reduce Charge Recombination in Organic Solar Cells: There are Still Lessons to Learn from P3HT:PCBM.* Advanced Electronic Materials, 2021. **7**(5).

Chapter 5: ZZ115:$PC_{60}BM$ charge transport and the VOTCA methodology

5.1. Introduction

Chapter **3** and **4** aimed to experimentally characterise the OPV donor molecule ZZ115 in an effort to characterise and assess factors that may influence bimolecular recombination. This chapter aims to provide insight into these observations by outlying the step-by-step methodology in modelling the main molecules of interest: ZZ115 and $PC_{60}BM$. After a suitable model is established, a large-scale calculation using the VOTCA software and methodology was attempted. While modelling methods such as molecular dynamics and kinetic Monte Carlo can be suited for larger systems, VOTCA combines multiple methods and offers an increased accuracy of properties measured as well as an opportunity to combine quantum mechanical models with classical mechanics. The VOTCA software, initially developed by Victor Ruhle, Christoph Junghans, Alexander Lukyanov, Kurt Kremer, and Denis Andrienko[1] was selected for its ability to model exciton transport in large systems. It is thus the aim of this chapter to introduce the VOTCA workflow and apply it to model charge transport in large systems in order to properly complement hypotheses and observations from the experimental Chapters **3** and **4**. A more detailed explanation of the full workflow of VOTCA can be found in the software's manual [2].

5.1.1 OPV computational modelling and choice of techniques

Studies on OPVs have employed a variety of modelling techniques including those described in Chapter **2** sections **2.3** to fulfil different needs**.** The seminal paper by J. Nelson[3] on bimolecular molecular recombination characterisation, discussed in more detail in Chapters **1**, **3** and **4**, primarily used Monte Carlo simulations to model charge transport and recombination in a material combination of MDMO-PPV and $PC_{60}BM$. A Monte Carlo method was used as the study focused on a large-scale system using modelled transfer rates. Moreover, a morphological study by J. Na and R. Chang on a material combination of P3HT, $PC_{60}BM$ and $PC_{70}BM$ were performed using Molecular Dynamics in order to investigate the effects of solvent evaporation[4]. MD was used for its ability to model large systems from a molecular mechanical approach

with no need to consider excited states, only morphological effects. On the other hand several studies on a variety of molecules have employed DFT and its extension TD-DFT[5, 6] in order to directly calculate properties such as the HOMO-LUMO, band gap and UV-VIS absorption spectrum. DFT is used for its ability to fairly accurately calculate fundamental electronic properties of the molecules at reasonable computational cost. KMC, MD and DFT methods can be manually combined but few software[7] are streamlined to execute a full scale calculation combining multiple different methodologies. VOTCA is one of them and was chosen to model charge transport across ZZ115:$PC_{60}BM$ based structures.

5.1.2 Transient properties and time dependent DFT

While DFT in of itself is a powerful method, a further extension of the approach is necessary to model transient features. One option is time-dependant density functional theory (TD-DFT) which aims to solve the time dependant version of the Schrodinger equation as shown in **Equation (5-1)**.

$$\left(\hat{U} + \hat{T} + \hat{V}(t)\right)\psi(\vec{r}, t) = E\psi(\vec{r}, t) \qquad \textit{(5-1)}$$

The general principals of DFT as described by section **2.3.1** in Chapter **2** remain true but must be updated with the addition of the time variable. The key new formalism is the Runge Gross theorem formulated in 1984[8] which serves as an analogue to the Hohenberg-Kohn theorem. Just as for the Hohenberg-Kohn theorem, the Runge Gross theorem postulates that the external time dependant potential $\hat{V}_{ext}(\vec{r}, t)$ can be determined by the time evolving one-body density $n(\vec{r}, t)$ for a given initial state ψ_0. Thus a time-dependent variation of the Kohn-Sham equations can be solved to calculate all the observables by proceeding with the following scheme. First an initial DFT calculation is done on the system to find the initial orbitals at the time t=0. The time dependent Kohn-Sham equations are then solved using a time-dependent self-consistency based on predicted and varying time steps. The orbitals found from this self-consistency step are then used to find the time-dependent particle density and therefore all the relevant observables, in particular the excited states and frequencies of excited state transitions, in a manner similar to normal DFT.

5.2. Initial modelling methodology and properties of interest

5.2.1 Relaxed ground state structure

A first step in fundamental characterisation of the molecule of interest lies in finding its ground state structure. This is done by doing a simple DFT calculation on the system of interest, ideally on a starting structure approaching or approximate to that of a relaxed structure (For ZZ115 this would be a planar structure). B3LYP[9, 10] with the DEF2-SVP basis set to describe the exchange correlation function, the functional and basis set chosen for this study, is a commonly used functional-basis set in OPV calculations. A more detailed explanation for the choice of this methodology is provided in Chapter **6** section **6.1.2** but to summarize B3LYP was found to provide reasonable accuracy at low computational cost. The ORCA software[11] was used in this chapter and study for these DFT calculations. For the ZZ115 molecule, another important consideration is the choice of oligomer used in DFT calculations. The oligomer was chosen after the monomer, dimer and trimer molecules were calculated and compared with experimentally measured properties.

5.2.2 Excited states and absorption

While several properties can be calculated using ground state DFT calculation, excited state calculations can be used to find the absorption spectrum found through the excited state transitions calculated using TD-DFT. Each excited state would be characterised by an oscillator strength and different contributions from occupied to unoccupied orbital transitions. In this study the calculations made use of the TDA approximation which leads to less computationally intensive calculations and was found to give good results[12] coupled with a Davidson algorithm[13]. The calculated absorption can then be compared to the UV-VIS spectrum measured in Chapters **3** and **4**.

5.3 VOTCA workflow and methodology

VOTCA is divided into two different modules. The module of interest is excitation transport module or VOTCA-XTP [14-16] whose operation is detailed below.

5.3.1 VOTCA-XTP workflow

A starting structure is built and relaxed using molecular dynamics, with either the GROMACS or LAMMPS software. In this study it was the GROMACS software[17] that was chosen for its ease of use and compatibility. Trajectory and topology are generated and allow for general mapping of the system by the VOTCA software. A list of all possible charge hopping sites and therefore possible sites for charge transfer is then generated from the system map, determined by first the list of neighbours defined by molecular pairs separated by a cut-off distance of choice. Following this the site energies are calculated from the electrostatic and polarisation effects on each molecule. This is combined with the precalculated reorganisation energies to give the final evaluation of the site energies for each molecule. DFT calculations are then performed on these individual sites to determine the orbitals relevant to charge transport and to be compared with the orbitals of the neighbouring pairs. The possible neighbouring pairs are then calculated using DFT with the objective of calculating the electronic coupling between each pair and thus the transfer integrals. The electronic coupling elements J_{ij} are determined thanks to **Equation (5-2)**

$$J_{ij} = \langle \phi_i | \hat{H} | \phi_j \rangle \tag{5-2}$$

With ϕ_i the HOMO or LUMO of the molecule and $\hat{H}$ the Hamiltonian of the site i-j dimer. From these calculations each potential hopping site is examined, and the charge transfer rates ω_{ij} between molecules are determined for each possible pair and thus the whole system using Marcus Theory as described in **Equation (5-3).**

$$\omega_{ij} = \frac{2\pi}{\hbar} \frac{{J_{ij}}^2}{\sqrt{4\pi\lambda_{ij}k_bT}} \exp\left[-\frac{(\Delta E_{ij} - \lambda_{ij})^2}{4\lambda_{ij}k_bT}\right] \tag{5-3}$$

With T the temperature, k_b the Boltzmann constant, λ_{ij} the reorganisation energy and ΔE_{ij} the difference between the site energies. Finally with these rates a Kinetic Monte Carlo simulation is performed to examine the charge carrier dynamics. A summary of the complete VOTCA workflow is given in ***Figure 5-1***.

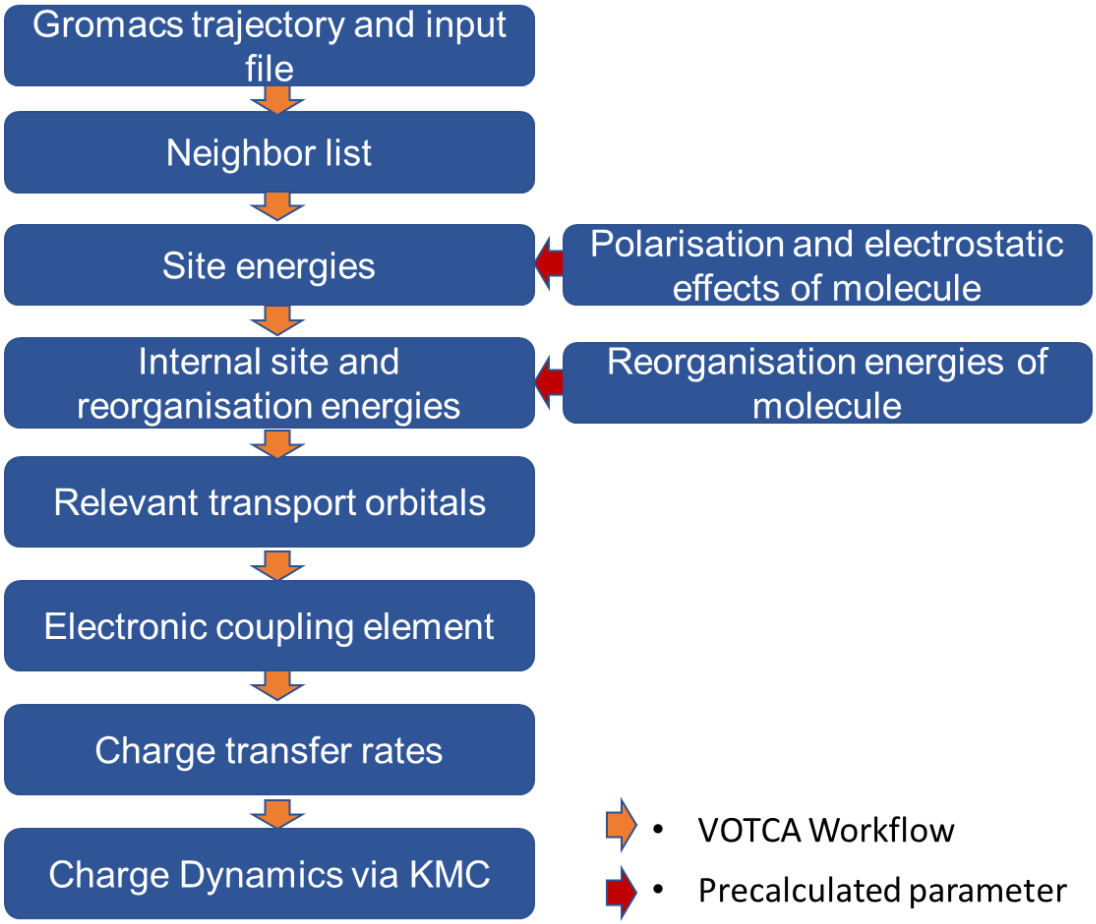

Figure 5-1: *Simplified diagram of the VOTCA workflow.*

5.3 Initial single molecule characterisation

5.3.1 ZZ115 order and characterisation

A first step to model ZZ115 is to find the ideal oligomer model ZZ115 to use for future calculations. To do this the first three orders in the monomer, dimer and trimer forms of ZZ115 were modelled using DFT with B3LYP/DEF2-SVP level of theory. Calculations were attempted on the tetramer but proved to be insufficiently accurate as the calculated orbitals proved to not be fully converged. The sidechains were truncated to methyls to facilitate calculations as well as enable later DFT calculations on larger size molecules. Such a simplification is permissible as side chains

do not generally affect molecule geometries[9, 18]. After an approximate structure was built, a first geometry optimisation was done using DFT. The resulting structures are shown in ***Figure 5-2***, showing all oligomers as having planar structures and with identical bond lengths and dihedral angles across the entire molecules. The only major structural difference between the oligomers lies in the length of the molecule.

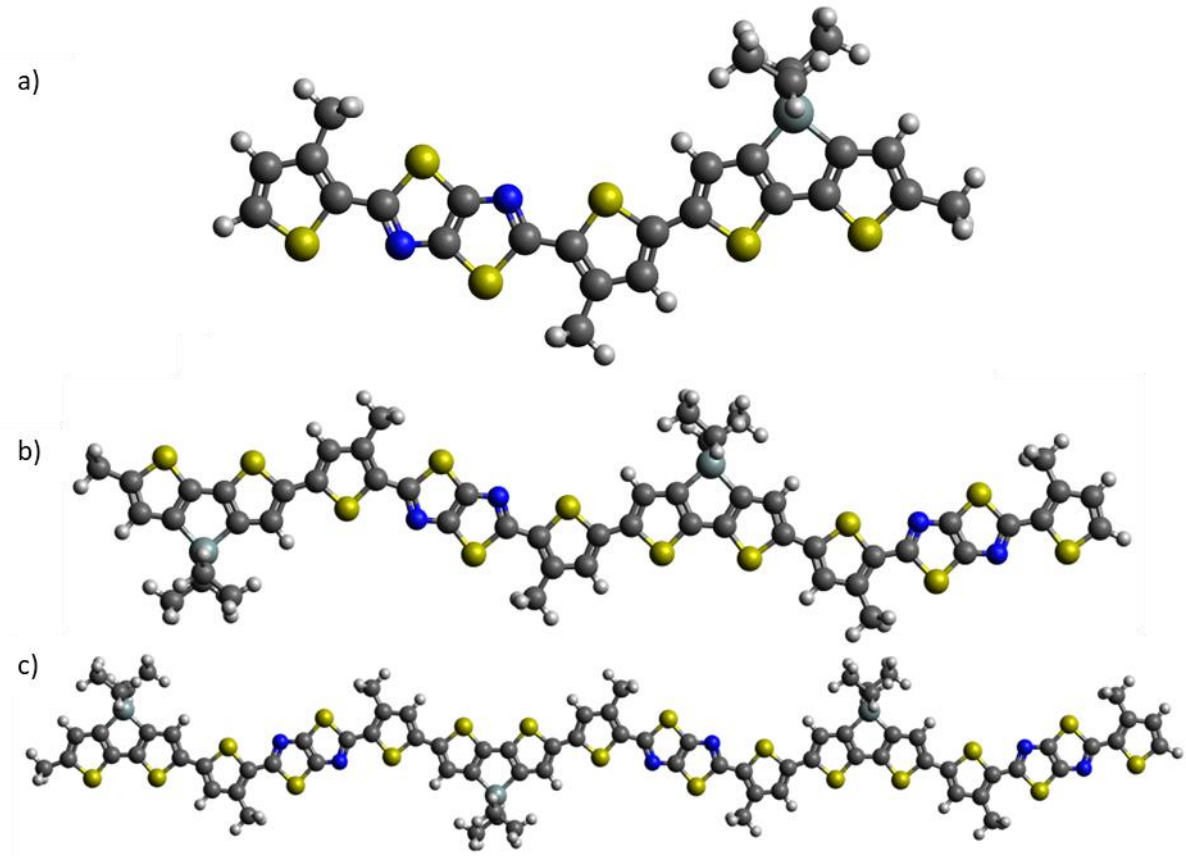

Figure 5-2*: 3D representation of ZZ115 monomer* ***a)****, dimer* ***b)*** *and trimer* ***c)*** *with side chains removed visualised using the Avogadro software*

From this relaxed ground state structure, the different molecular orbitals of each molecule were determined with the first HOMO-LUMO levels described in ***Figure 5-3***.

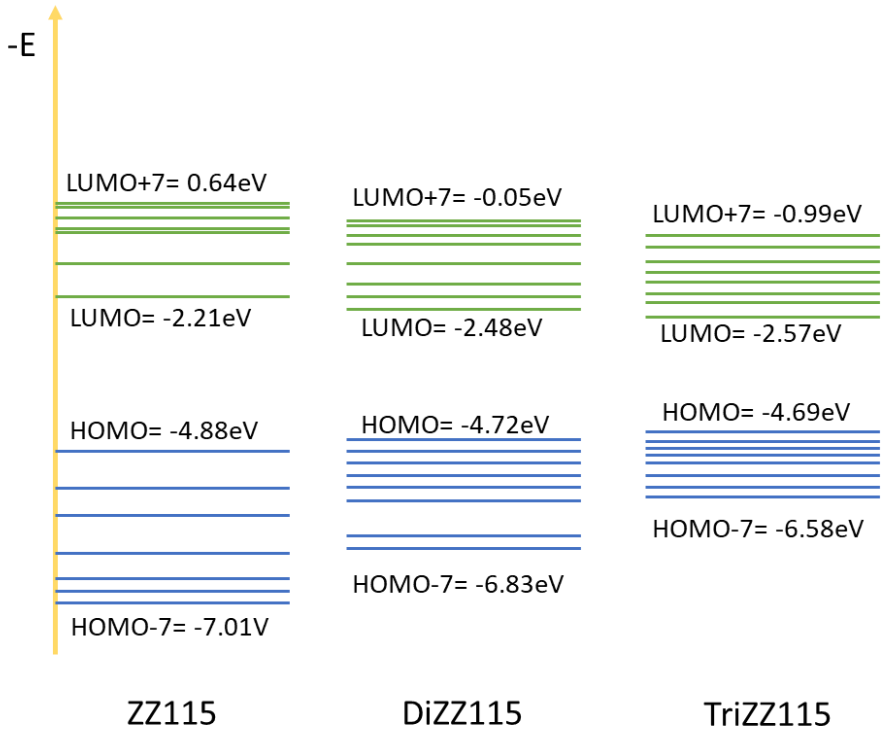

Figure 5-3: *Energy level diagram of calculated molecular orbitals for ZZ115 monomer, dimer (DiZZ115) and trimer (triZZ115). The individual lines in green and blue represent the individual calculated orbitals.*

Orbital energy calculations confirm the molecule's characterisation of an electron donor molecule. The HOMO and LUMO levels are in line with other donor molecules used in OPVs [9, 19, 20] but the calculated values differ from the ZZ115 experimental values found in previous experimental studies[21, 22] as seen by **Table 5-1**. The narrowing of the band gap going from 2.67 eV for the monomer to 2.12 eV for the trimer from increased polymer conjugation is also illustrated in ***Figure 5-3*** and is typical of conjugated polymers as seen with a similar calculation done on P3HT[23]. One consideration would lie in the inherent nature of DFT potentially misestimating the orbital levels by a non-trivial margin[24]. This is in addition to considerations of crystallinity and morphology playing a role in the orbital energy levels, considerations not yet included in calculations of ZZ115. The end result is a limited ability to compare orbital levels calculated through DFT with those measured experimentally, a natural consequence of the difference between the optical bandgap (the HOMO-LUMO difference, estimated by techniques such as DFT) and electrochemical bandgap (reduction potential and oxidation potential difference, measured through techniques like cyclic voltammetry)[25]. Nevertheless, a comparison provides an

indication of the best suited form of the ZZ115 polymer to use in future calculations, with the dimer form appearing closest to experimental measurements but the trimer accounting for DFT- experimental differences better.

Table 5-1: *Calculated HOMO, LUMO and Bandgap of the ZZ115 monomer, dimer, and trimer as well as values experimentally found in the literature via cyclic volumetry*

(eV)	ZZ115	DiZZ115	TriZZ115	Experimental values
LUMO	-2.2	-2.5	-2.6	-2.8[21] /-3.4[26]
HOMO	-4.9	-4.7	-4.7	-5.1[21] /-5.3[26] /-5.3[27]
Band gap	**2.7**	**2.2**	**2.1**	**2.3[21]/1.9[26]**

To further examine the different oligomers, the HOMO and LUMO were visualised and analysed as shown in ***Figure 5-4***.

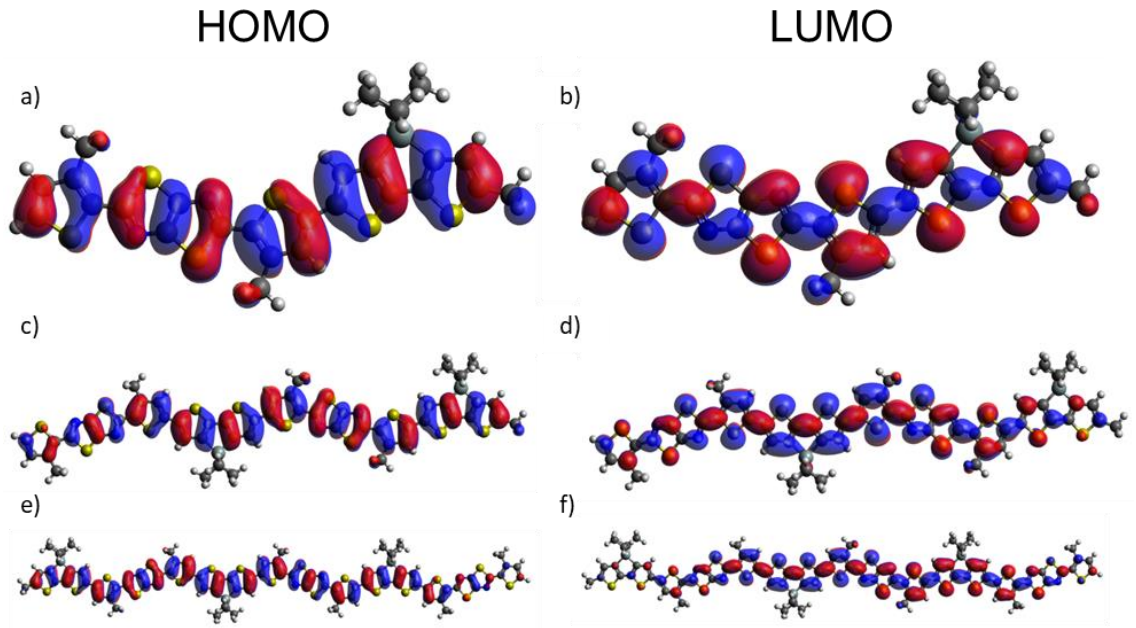

Figure 5-4: *3D representation of ZZ115 monomer orbitals with* ***a)*** *HOMO and* ***b)*** *LUMO, ZZ115 dimer with* ***c)*** *HOMO and* ***d)*** *LUMO and ZZ115 trimer with* ***e)*** *HOMO and* ***f)*** *LUMO. With the blue and red colours indicating isosurfaces with ±0.01 for all orbitals, visualised using the Avogadro software*

An inspection of the molecular orbitals highlights the conjugated nature of ZZ115 as the HOMO to LUMO transition characterised by a π to π* orbital shape transition seen as an aromatic to quinoidal orbital shape transition. This orbital shape transition is consistent for all oligomers studied, though the trimer appears to not have the

HOMO or LUMO spread across the entire molecule, suggesting the trimer as a better choice to ascertain orbital localisation effects.

Following this, the excited states (singlets) were calculated and the transitions leading to these states determined using TDDFT. The resulting calculated absorption spectra plotted using the oscillator strength of the excited state transitions compared to the experimentally measured spectrum from Chapter **3** is given by ***Figure 5-5***.

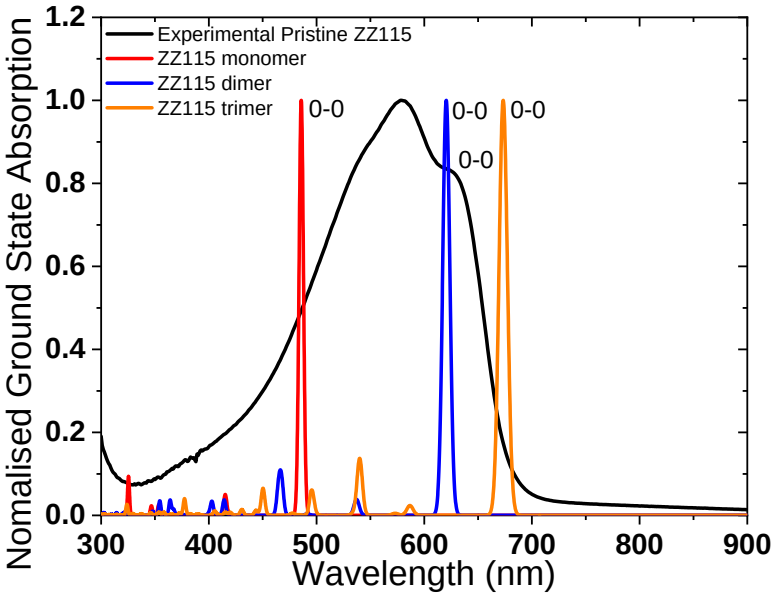

Figure 5-5: *Graph of calculated absorption spectra for all three considered forms of ZZ115 (red, blue and orange respectively) with the measured experimental spectrum (black). The HOMO to LUMO transitions for each calculated oligomer are given with the assigned 0-0 peak of the experimental ZZ115 absorption*

A comparison of the three calculated oligomers reveals very distinctive spectra. The ZZ115 monomer can be characterised by three main energy states at the 486 nm, 415 nm and 325 nm wavelength, with the primary transition from HOMO to LUMO occurring at the 486 nm wavelength. The dimer has the HOMO-LUMO transition peak at 620 nm and secondary peak at 460 nm. Finally, the trimer has the HOMO-LUMO transition peak at 675 nm. Comparing these calculated spectra to the experimentally measured spectra shows differences with all three oligomers as the 0-0 peak transition of the experimentally measured spectrum at 630 nm. The experimental secondary 0-1 peak at 580 nm also diverges from any of the calculated oligomer peaks. As an underestimation of the S_1 energy is expected by DFT, this would suggest the trimer as best suited to represent ZZ115 based excited states, underestimating the S1 energy by 0.14 eV.

From the ground state and excited state calculations the trimer oligomer appears the best suited compared to experimental measurements both from this thesis and in the literature. However, the dimer was ultimately chosen to model ZZ115 as it appeared to correspond to experimental measurements close enough but with a significantly reduced computation cost. The ORCA software used is limited in that systems of more than 200 atoms start to see SCF convergence issues and a system comprised of ZZ115 dimer + $PC_{70}BM$ already approaches the limit. Moreover, due to the number of DFT calculations required in the VOTCA methodology for large systems, a reduced computational cost is welcome. As such it is the dimer form that was investigated in more detail for the remainder of the study.

5.3.2 $PC_{60}BM$ characterisation

Simulations were done on individual fullerene molecules for a better point of comparison and understanding of the blend material systems. $PC_{60}BM$ was modelled using the same parameters for the ZZ115 based calculations as outlined previously. This resulted in the structure as shown in ***Figure 5-6***. As with ZZ115 the orbital energies of the relaxed structure were calculated to obtain the HOMO and LUMO as listed in ***Table 5-2*** and represented in ***Figure 5-7***.

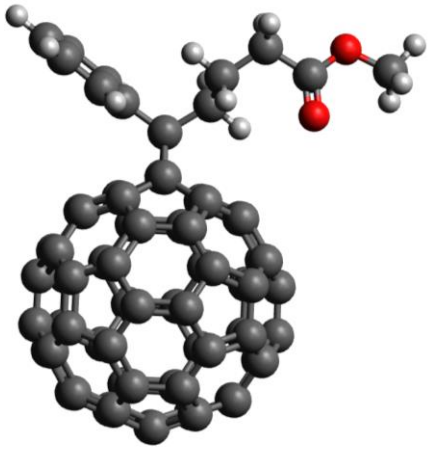

Figure 5-6: *Representation of $PC_{60}BM$ molecule used in calculations rendered in the Avogadro software.*

Table 5-2: *Calculated HOMO, LUMO and Bandgap of $PC_{60}BM$ as well as experimental (cyclic voltammetry) and computational values found in the literature*

	Calculated $PC_{60}BM$	$PC_{60}BM$ Experimental values	$PC_{60}BM$ Computational values
LUMO	-3.3	-3.7[28]/ -3.9[29]	-3.5[30]
HOMO	-5.8	-6.1[28]/ -5.9[29]	-6.1[30]
Bandgap	2.5	2.4[28]/ 2.0[29]	2.6[30]

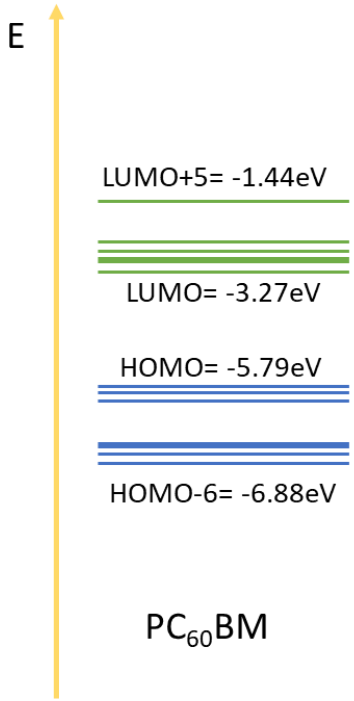

Figure 5-7: *Energy level diagram of calculated molecular orbitals for $PC_{60}BM$*

As highlighted by ***Table 5-2***, a small discrepancy between is observed between the experimental values and the presently calculated orbitals, with the band gap differing by 0.1 eV to 0.4 eV. While a similar discrepancy was found previously for the ZZ115 series, the discrepancy has been observed in another similar comparison done via a combination of DFT and cyclic voltammetry[31], with the key observation being a consistent discrepancy ranging from 0.2 eV to 0.9 eV between the band gap obtained via DFT and that obtained experimentally. It would appear thus that the present model of $PC_{60}BM$ is suitable for further calculations. As with ZZ115, TD-DFT was used to calculate $PC_{60}BM$ absorption spectrum as shown in ***Figure 5-8***, allowing additional validation of the modelled $PC_{60}BM$.

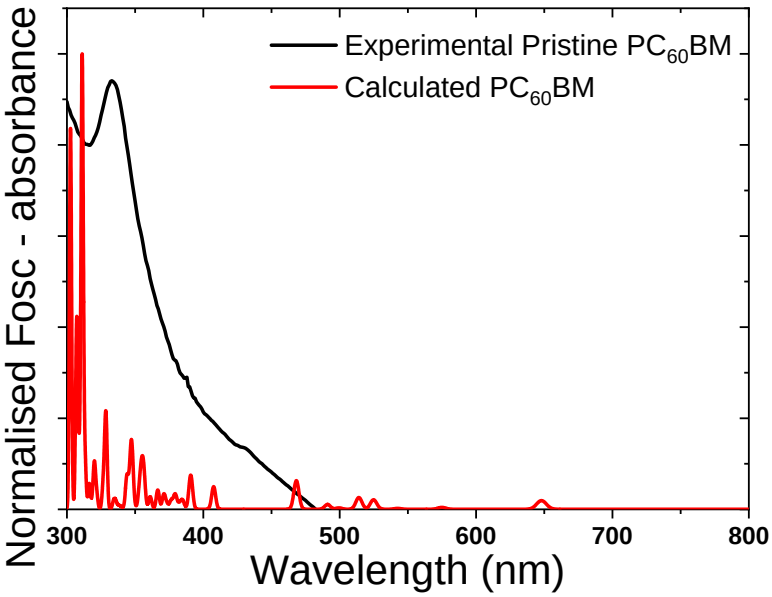

Figure 5-8: *Comparison of calculated PC60BM spectrum with measured experimental spectrum*

A comparison of the fullerene simulation with the previous experimental measurements reveals a close similarity in overall shape. A slight shift in the highest peak of around 25 nm between the computational and experimental traces is consistent with bandgap discrepancies. PC60BM therefore appears suitably close to experiment that VOTCA calculations would serve as a suitable comparison with results found in Chapters **3** and **4**.

5.4 VOTCA calculations

5.4.1 Example calculation: Methane

To illustrate the VOTCA method in action as well as test for consistency in methodology a relaxed system of 1000 methane molecules was used provided by the VOTCA tutorial section. The initial system methane system from a GROMCAS trajectory and topology appears as shown in ***Figure* 5-9*.***

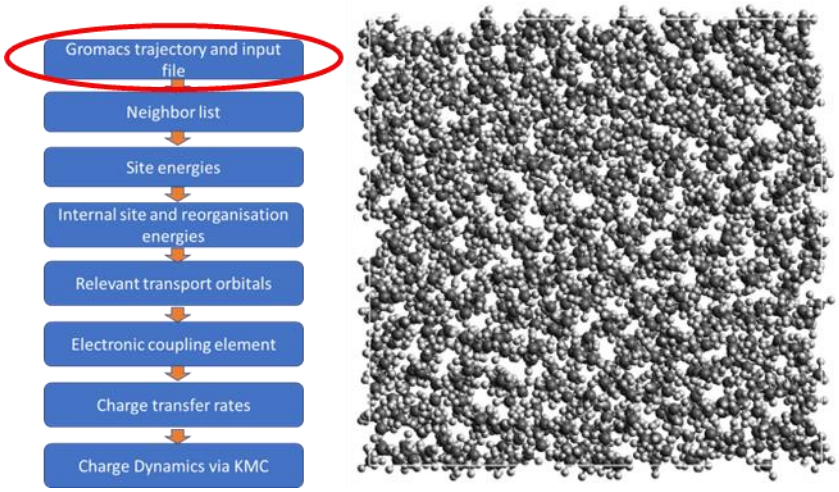

Figure 5-9: *Render of methane system using the Avogadro software.*

From this initial molecular dynamically relaxed structure, the list of potential neighbours was calculated at 21093 potential pairs of which 8586 were modelled with classical mechanics. Following this the site energies of all 1000 methane molecules was computed. As calculations for each methane molecule are done on the ground state, charged (electron doped), discharged (hole doped), and S_1 state, this yields a total of 4000 calculations or 4 for each site. A calculation done on the very first molecule leads to the following site energies as described in **Table 5-3**. The total energy is calculated as the sum of the electrostatic and polarisation contributions to the molecule.

Table 5-3: *Example of calculation results for site energies on one methane molecule for four different states.*

	Ground state	Charged	Discharged	S_1
Static Energy (eV)	0.0022	-0.0245	0.0543	0.0065
Polar Energy (eV)	-0.0033	-0.8324	-0.7532	-0.0130
Total energy (eV)	-0.0011	-0.8569	-0.6991	-0.0065

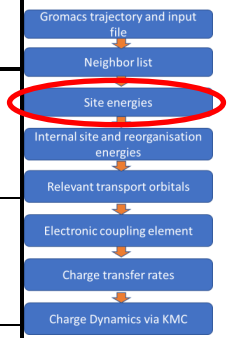

The next step involves executing quantum mechanical calculations on each individual molecule, giving 1000 total jobs. The reorganization energies are then calculated using

the precalculated internal energies as given by **Table 5-4** and the relevant transport orbitals are then determined and verified.

Table 5-4: *Example of calculation results for reorganisation energies on one methane molecule for four different states.*

End transition state	Reorganisation Energy (eV)
Hole doped	0.3
Electron doped	0.7
S_1	0.3
Triplet	0.7

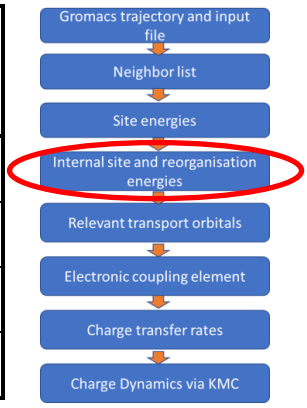

Following this, quantum mechanical calculations are done on each site pair. From the initial list of 21093 pairs, removing the 8586 classical pairs leaves 12507 QM pairs to calculate and couplings to evaluate. An example of QM coupling calculated is found in **Table 5-5.**

Table 5-5: *Example of calculation results for site pair QM calculations on a methane molecule pair.*

Hole Coupling (eV)	0.02256
Electron Coupling (eV)	0.04269

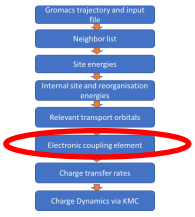

On the remaining 8586 classical pairs the classical coupling of transition is then determined before a final coupling calculation is performed. Following this a Kinetic Monte Carlo simulation is done using the previously calculated couplings. For a single electron travelling through the system under an electric field along the X axis of 1×10^{-8} V/nm the following properties were calculated as summarised in ***Table 5-6***.

Table 5-6: *Example of calculation results for KMC calculations on one methane molecule under an electric field along the X axis of 1×10^{8} V/nm for a simulation time of $5.92s\times10^{-9}s$.*

Direction	X	Y	Z
Average Carrier Velocity (nm/s)	1.205×10^{8}	5.672×10^{7}	1.960×10^{7}
Distance travelled (nm)	7.137×10^{-1}	3.359×10^{-1}	1.161×10^{-1}
Average Mobility in field direction (m^2/Vs)	1.205×10^{-2}		

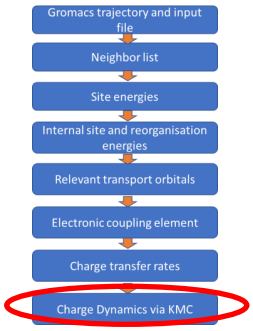

Thus, in a system comprised of 1000 methane molecules, the trajectory of a single electron was determined. While the calculation only used one charge carrier, one could feasibly inject as many charge carriers as deemed necessary and compute the spatial distribution of charges and energetic disorder. This methodology applied to ZZ115 could give insights on potential inhomogeneous spatial distribution of charges at the donor, acceptor interface hypothesised in Chapter **4**. With an example calculation tested on a 1000 methane molecule system, the same steps were employed to model ZZ115.

5.4.2 Attempted VOTCA calculations on ZZ115: Initial test and calculations

Unfortunately, calculations on a full scale ZZ115 based system were not able to be done within the allocated time period of this study. Presented here is a summary of the work done over the course of a year, trying to achieve the methodology tested and outlined above, a description of problems encountered and the attempts at solving these issues.

A very early test aimed to use a system comprised of two ZZ115 dimer molecules as shown by ***Figure 5-10*** This test system was deliberately chosen with an intermolecular distance of around 4 Å as the aim was to test the viability of calculations and familiarisation with the software and previous experimental studies found an intermolecular distance of around this length, explained in more detail in Chapter **6**

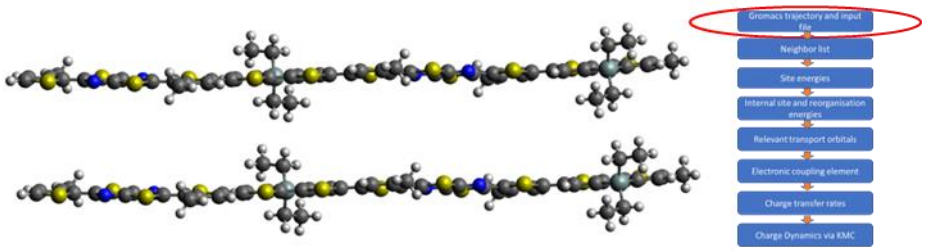

***Figure 5-10**: Render of test ZZ115 system using the Avogadro software.*

As only one pair of molecules is present, the neighbour list calculation was short but using the same parameters as the methane calculation the pair was properly identified by the software. Accordingly, the site energies were calculated in **Table 5-7**.

***Table 5-7:** Example of calculation results for site energies on one ZZ115 molecule for four different states.*

	Ground state	Charged	Discharged	Excited S1
Static Energy (eV)	0	0	0	0
Polar Energy (eV)	0	0	0	0
Total energy (eV)	0	0	0	0

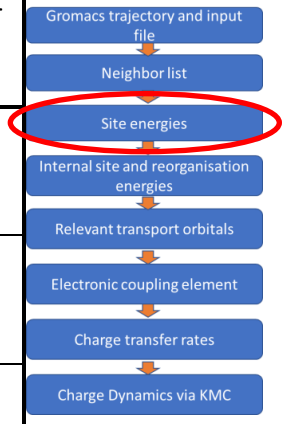

It would initially appear that the site energies calculation failed but as there is only one other molecule found in the polar region, at a significant distance, both starting neutrally charged, the resulting calculation would have a site energy of 0 for all possible states. Even so calculations were continued with the reorganisation energies calculated beforehand given in **Table 5-8**.

Table 5-8: *Example of calculation results for reorganisation energies from the ground state on one ZZ115 molecule for four different states.*

End transition state	Reorganisation Energy (eV)
Hole doped	0.58
Electron doped	0.47
S1	0.61
Triplet	0.45

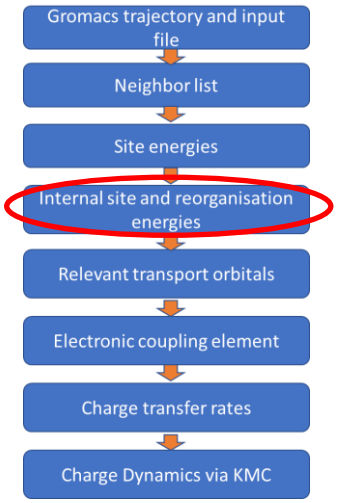

An important distinction in methodology between the methane system and the test ZZ115 systems lies in the DFT calculation software. VOTCA comes with its own DFT toolkit which is employed for the methane system but unfortunately does not scale well enough with molecule size and would fail when dealing with systems of over 150 atoms. Instead, VOTCA is compatible with the ORCA software allowing more advanced DFT calculations, a necessary feature for the ZZ115 system. The resulting calculated couplings are given in **Table 5-9**

Table 5-9: *Example of calculation results for site pair QM calculations on a ZZ115 molecule pair.*

Hole Coupling (eV)	1.067×10^{-8}
Electron Coupling (eV)	7.977×10^{-9}

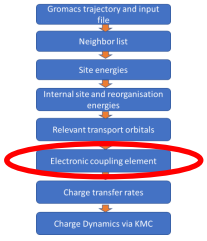

As can be somewhat expected given the chosen system the calculated couplings are flawed with calculated electronic couplings being far from expected in terms of range (P3HT-P3HT is the range of meV[32]). This is most likely due to the system once again comprising of only two neutral state molecules separated by a significant distance, hence a low coupling. KMC calculations were performed even with this two-molecule system and using the above couplings as proof of concept with the results given in

Table 5-10.

Table 5-10: *Example of calculation results for KMC calculations on two ZZ115 molecule system.*

Direction	X	Y	Z
Average Carrier Velocity (nm/s)	0	0	0
Distance travelled (nm)	0	0	0
Average Mobility in field direction (nm^2/Vs)	0		

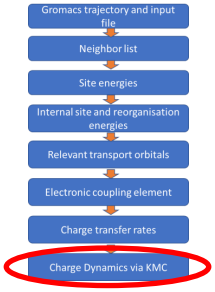

As was expected, the results show a KMC calculation with effectively no change in the system as the rate of transfer was effectively 0. Nevertheless, the methodology was demonstrated with the initial properties required calculated, and parameter and initial system optimization could lead to an accurate calculation providing meaningful results. Upscaling attempts to model larger system however ultimately led to failure.

5.4.3 Problems and limitations encountered

A primary problem from the VOTCA methodology and its use with the ZZ115 system stemmed from the calculations required during the calculation of transfer integrals of hopping sites as shown in ***Figure 5-1***. As a DFT calculation is required for each pair of hopping sites, this leads to a number of calculations going beyond the number of molecules in the system. Due to the size of the ZZ115 dimer, this caused calculations using the innate VOTCA DFT module to fail, especially for the larger hopping site calculations. VOTCA is compatible with the ORCA software which allows the calculations to run but then issues arose from attempting to run the calculations in parallel on multiple nodes, as communication between the two software showed issues when trying to scale the allocated memory for each DFT calculation. The end result was a severe limitation in number of possible calculations and led to the scaling down of systems in order to focus on molecule-molecule interactions. An estimation of the timeline of events involved in the VOTCA software is provided in **Table 5-11**.

Table 5-11: *Simplified timeline of research using the VOTCA software with issues encountered*

Events	Issues Encountered	Solution Employed	Timeframe
Gromacs training			2 weeks
Votca installation	Module Compatibility	-Trial and error -Communication with server admin	2 weeks
ACPYPE and Antechamber installation	N/A	N/A	2 days
VOTCA tutorial run	-Parallelisation of heavy calculation segments -Various minor bugs -New installation issues from Software upgrade	-Direct communication with VOTCA developers and server admin -Trial and error of the option files	1 month
ZZ115 Gromacs file preparation	-ACPYPE not working properly -ACPYPE-Antechamber communication issues	Edit of the ACPYPE script	2 weeks
ZZ115 Input file preparation and calculation	N/A	N/A	2 weeks
$PC_{60}BM$ Input file preparation and calculation	N/A	N/A	1 Week
Votca Test ZZ115 system steps 1 to 3			1 week
Votca Test ZZ115 sytstem steps 4 to 6	-Orca/Votca inteface issues	-Communication with VOTCA developers and research group members	1 month
Larger ZZ115 Gromacs file preparation and calculation	- Parameter optimisation		1 week
Votca larger ZZ115 system steps 6 to 8	-KMC module results file compatibility		1 Month

5.4.4 Possible solutions to encountered problem

Two very crucial aspects to solve some of the problems encountered is working on a full performance optimisation and upscaling calculations. As the in-built DFT module struggles with high atom count, the ORCA module will be needed and thus fixing parallelisation compatibility issues will be paramount. Additionally, memory compatibility and optimization as well as resource allocation could help the strain on the performance that led to calculation failures. In parallel to sorting out the encountered problems however a greater emphasis was made on molecule-molecule interactions for ZZ115 and other related molecules, with the results of these calculations shown in Chapter **6**.

5.5 Conclusion

A series of calculations using Density Functional Theory and its derivative Time-dependent Density Functional Theory was done on the same material systems studied in previous chapters to obtain insight on the electronic ground state behaviour of ZZ115 and $PC_{60}BM$ as well as find the best way to model ZZ115. The VOTCA software is combination of different computational methods that aims to provide a simulation of charge transport, that was used to provide additional insight into experimental results. While an initial proof of concept using a system of 1000 methane molecules was demonstrated, setbacks and limitations prevented the full calculations to be completed on large ZZ115 based systems, even with a general methodology established. Nevertheless, solutions for resolving these setbacks were given with the possibility of these large-scale calculations being completed in a future work using the same methodology.

5.6 References

1. V. Ruhle, C. Junghans, A. Lukyanov, K. Kremer, and D. Andrienko, *Versatile Object-Oriented Toolkit for Coarse-Graining Applications.* 2009. **5**(12).
2. Team, V.D. *Votca XTP Manual*. 2022; Available from: https://www.votca.org/xtp/XTP-MANUAL.html.
3. J. Nelson, *Diffusion recombination in polymer-fullerene blends and its influence on photocurrent collection.* Physical Review B, 2003. **67**(15).
4. J. Na and R. Chang, *Morphological Stability of Organic Photovoltaics: Coarse-grained Molecular Dynamics Simulation Studies.* Bulletin of the Korean Chemical Society, 2021. **42**(7).
5. M. Bourass, A. T. Benjelloun, M. Benzakour, M. Mcharfi, F. Jhilal, F. Serein-Spirau, . . . M. Bouachrine, *DFT/TD-DFT characterization of conjugational electronic structures and spectral properties of materials based on thieno[3,2-b][1]benzothiophene for organic photovoltaic and solar cell applications.* Journal of Saudi Chemical Society, 2017. **21**(5).
6. M. B. Salim and R. Nekovei, *Electronic Properties and Molar Excitation Coefficient for Organic Solar Cells Materials by using TD-DFT Method*, in *2019 IEEE 46th Photovoltaic Specialists Conference (PVSC)*. 2019, IEEE.
7. C. D. Sherrill, D. E. Manolopoulos, T. J. Martinez, and A. Michaelides, *Electronic strcutre software.* The Journal of Chemical Physics, 2020. **153**(7).
8. E. Runge and E.K.U. Gross, *Density-Functional Theory for Time-Dependent Systems.* Physcial Review Letters, 1984. **52**(12).
9. Q. Zhang, Y. J. Wheng, W. Sun, Z. Ou, O. Odunmbaku, M. Li, . . . K. Sun, *High-Efficiency Non-Fullerene Acceptors Developed by Machine Learning and Quantum Chemistry.* Advance Science, 2022. **9**.
10. M. Bourass, A. T. Benjelloun, M. Benzakour, M. Mcharfi, M. Hamidi, S. M. Bouzzine, . . . M. Bouachrine, *Theoretical Studies by Using the DFT and TD-DFT of the effect of the bridge formed of thienopyrazine in solar cells* Journal of Materials and Environmental Science, 2015. **6**(6).

11. F. Neese, *The ORCA program system.* Computational Molecular Science, 2012. **2**(1).

12. A. Chantzis, A. D. Laurent, C. Adamo, and D. Jacquemin, *Is the Tamm-Dancoff Approximation Reliable for the Calculation of Absorption and Fluorescence Band Shapes?* Journal of Chemical Theory and Computation, 2013. **9**.

13. E. R. Davidson, *The iterative calculation of a few of the lowest eigenvalues and corresponding eigenvectors of large real-symmetric matrices.* Journal of Computational Physics, 1975. **17**(1).

14. J. Wehner, L.B., J. Brown, C. Junghans, O. Caylak, Y. Khalak, P. Madhikar, G. Tirimbo, B. Baumeier, *Electronic Excitations in Complex Molecular Environments: Many-Body Green's Functions Theory in VOTCA-XTP.* Journal of Chemical Theory and Computation, 2018. **14**(12).

15. V. Ruhle, A. Lukyanov, F. May, M. Schrader, T. Vehoff, J. Kirkpatrick, . . . D. Andrienko, *Microscopic Simulations of Charge Transport in Disordered Organic Semiconductors.* Journal of Chemical Theory and Computation, 2011. **7**(10).

16. G. Tirimbo, V. Sundaram, O. Caylak, W. Scharpach, J. Sijen, C. Junhans, . . . B. Baumeier, *Excited-state electronic structure of molecules using many-body Green's functions: Quasiparticles and electron–hole excitations with VOTCA-XTP.* The Journal of Chemical Physics, 2020. **152**.

17. H. Bekker, H. J. C. Berendsen, E. J. Dijkstra, S. Achterop, R. van Drunen, D. van der Spoel, . . . M.K.R. Renardus, *Gromacs: A parallel computer for molecular dynamics simulations.* 1993.

18. R. Rydberg and L. Olsen, *The Accuracy of Geometries for Iron Porphyrin Complexes from Density Functional Theory.* The journal of Physical Chemistry A, 2009. **113**(43).

19. G. Weihao, *An overview on P3HT:PCBM, the most efficient organic solar cell material so far. .* Solid State Physics II, 2009.

20. J. M. Marin-Beloqui, K. J. Fallon, H. Bronstein, and a.T.M. Clarke, *Discerning Bulk and Interfacial Polarons in a Dual Electron Donor/Acceptor Polymer.* J. Phys. Chem. Lett., 2019. **10**: p. 3813-3819.

21. M. Zhang, X. Guo, and Y. Li, *Synthesis and Characterization of a Copolymer Based on Thiazolothiazole and Dithienosilole for Polymer Solar Cells.* Advanced Energy Materials, 2011. **1**(4): p. 557-560.

22. J. Peet, L. Wen, P. Byrne, S. Rodman, K. Forberich, Y. Shao, . . . D. Waller, *Bulk heterojunction solar cells with thick active layers and high fill factors enabled by a bithiophene-co-thiazolothiazole push-pull copolymer* Appl. Phys. Lett., 2011. **98**.

23. M. A. Ansari, S. Mohiuddin, F. Kandemirli, and M.I. Malik, *Synthesis and characterization of poly(3-hexylthiophene): improvement of regioregularity and energy band gap.* Royal Society of Chemistry, 2018. **8**.

24. T. M. McCormick, C. R. Bridges, E. I. Carrera, P. M. Dicarmine, G. L. Gibson, J. Hollinger, . . . D.S. Seferos, *Conjugated Polymers: Evaluating DFT Methods for More Accurate Orbital Energy Modeling.* Macromolecules, 2013. **46**.

25. R. Holze, *Optical and Electrochemical Band Gaps in Mono-, Oligo-, and Polymeric Systems: A Critical Reassessment.* Orgnaometallics, 2014. **33**.

26. J. Marin-Beloqui, G. Zhang, J. Guo, J. Shaikh, T. Wohrer, S. M. Hosseini, . . . T.M. Clarke, *Insight into the Origin of Trapping in Polymer/Fullerene Blends with a Systematic Alteration of the Fullerene to Higher Adducts.* The Journal of Physical Chemistry C, 2021. **126**(5): p. 2708–2719.

27. Scharber, M.C., *On the Efficiency Limit of Conjugated Polymer:Fullerene-Based Bulk Heterojunction Solar Cells.* Advanced materials, 2016. **28**(10).

28. Ossila, *PC60BM*. 2022: Ossila.com.

29. Y. He and Y. Li, *Fullerene derivative acceptors for high performance polymer solar cells* Phys. Chem. Chem. Phys., , 2011. **13**: p. 1970-1983

30. A. Pal, L. K. Wen, C. Y. Jun, I. Jeon, Y. Matsuo, and S. Manzhos, *Comparative density functional theory–density functional tight binding study of fullerene derivatives: effects due to fullerene size, addends, and*

crystallinity on band structure, charge transport and optical properties. Physical Chemistry Chemical Physics, 2017(41).

31. D. Vanossi, L. Cigarini, A. Giaccherini, E. da Como, and C. Fontanesi, *An Integrated Experimental/Theoretical Study of Structurally Related Poly-Thiophenes Used in Photovoltaic Systems.* Molecules, 2016. **21**.
32. Kose, M.E., *Evaluation of Excitonic Coupling and Charge Transport Integrals in P3HT Nanocrystal.* The Journal of Physical Chemistry C, 2011. **115**.

Chapter 6: ZZ115 DFT characterisation and comparison with other donor polymers

6.1 Introduction

Chapters **3** and **4** observed two transient features, hypothesised to be a ZZ115 polaron recombining in a ZZ115 crystalline domain, and a ZZ115 polaron recombining in a mixed amorphous domain. Chapter **5** aimed to confirm the assigned transient features of ZZ115 measured Chapters **3** and 4, and while the VOTCA methodology was established, the study was unable to be finished within the allocated time. Chapter **6** serves as a compilation of work done in parallel to addressing the issues encountered in Chapter **5**, while aiming to provide some insight into the observations of Chapter **4**, most notably on the fundamental properties of the ZZ115 blends and possible corroboration with APS data. As such this Chapter aims to outline DFT-related calculations done on ZZ115 based systems as well as closely related systems in PCPDTTTz and Si-PCPDTBT.

6.1.1 Material Selection

Previous chapters focused on the influence of various acceptors on the ZZ115 molecule. This chapter however aims to compare the ZZ115 donor molecule with other closely related donor molecules. The first molecule of interest is PCPDTTTz, the ZZ115 molecular structure but with the crucial silicon atom replaced with a carbon atom, as illustrated by ***Figure 6-1***. PCPDTTTz has been compared to ZZ115 in several experimental studies [1, 2] by T. Clarke *et al.* noting a very distinct difference in charge recombination characteristics. PCPDTTTz was found to have a Langevin behaviour when combined with $PC_{60}BM$, and a longer lived CT state, possibly caused by a reduced crystallinity and therefore more difficult dissociation from more difficult pathways, compared to its silicon counterpart. Additionally greater charge generation was observed for the silicon variant when blended with $PC_{60}BM$. Moreover, analogue studies on Si-PCPDTBT vs PCPDTBT[3, 4] found the silicon to induce significant advantages in device photo-characteristics and morphology, with an increased charge generation and increased π-π stacking. A closer look at the intrinsic differences between ZZ115 and PCPDTTTz could provide additional insight into the influence of the silicon atom on a fundamental level, possibly shedding light onto the causes for the experimentally observed differences.

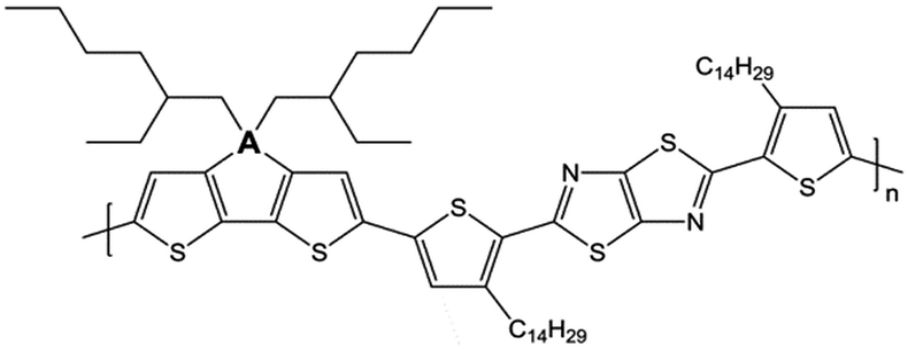

Figure 6-1: *Structure of the polymers of interest with A=Si for ZZ115 and A=C for PCPDTTTz.*

Another important molecule for comparison is the aforementioned Si-PCPDTBT. Si-PCPDTBT and ZZ115 have been compared before[1, 5, 6] due to a structurally similar donor unit as shown in ***Figure 6-2***. The main observations found from our previous paper[5] were a lack of variance in recombination kinetics and density of states with different fullerene acceptors contrasting with variations in kinetics and density of states found in ZZ115. Providing insight into the electronic differences between the two molecules could help explain the differences found in our previous paper and the importance of the common donor unit.

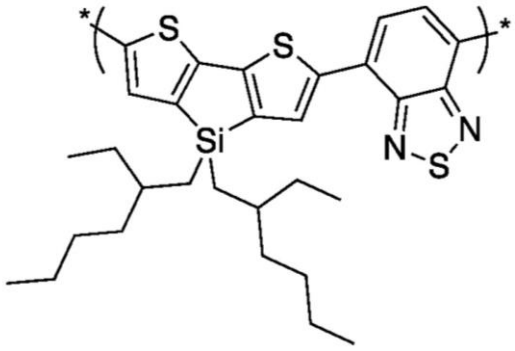

Figure 6-2: *Structure of the polymer Si-PCPDTBT*

6.1.2 Modelling the bandgaps in OPVs and choice of functional

As with molecular orbitals, the bandgap in OPVs has been discussed before in Chapter **1** sections **1.4**-**1.5.** In relation to this chapter the bandgap can be calculated using DFT. DFT suffers from a degree of inaccuracy in orbital energy and shape calculations unless utilising specific corrections[7, 8]. The bandgap calculation notably misestimates the bandgap[9] and has been a focus of research in order to correct these inaccuracies. Currently B3LYP is one of the most widely used functional in OPVs

thanks to its ability to partially correct these inaccuracies[10]. Even so other functionals based on B3LYP such as CAM-B3LYP[11] have developed offering advantages and disadvantages depending on the system. The interactions between two molecules were modelled with a greater consideration on the choice of functional that would best suit the calculations. The aim of this study lies in assessing the excited states of the materials of interest, thus the choice of functional would prioritise accurate orbital energies and accurate long-range interactions for proper assessment of intermolecular interactions. While B3LYP is among the most commonly used functional in OPV calculation, it has been reported to be worse for certain types of calculations[12] especially for TDDFT calculations. Nine different functionals were compared on a ZZ115:$PC_{60}BM$ system with the S_0 to S_1 excitation calculated and compared in ***Table 6-1***. The relaxed structure shown in ***Figure 6.14b*** was calculated first using B3LYP/DEV2-SVP level of theory, without any dispersion correction. The parameters for the initial relaxation were chosen for computation and time efficiency. The ground state was then calculated using the same basis set and accuracy criteria but with the functional of interest to confirm the validity of the previously shown results as well as to evaluate the use of B3LYP as a functional used for these calculations. The initial methodology plan included calculations of the excited state energy as an additional means of comparison but calculations using certain functionals proved too computationally expensive (wB2PLYP, wB2GPPLYP, WB97x) or were unable to finish SCF convergence at the desired level of accuracy (CAM-B3LYP, LC-B3LYP, SCAN). As a result of this functional study, the functional B3LYP was confirmed as the functional of choice for all calculations due to its ability to provide an accurate estimation of the bandgap (0.09 eV difference between computational and experimental) at a reasonable computational cost.

Table 6-1: *Calculated bandgaps of ZZ115:$PC_{60}BM$ system with different functionals*

Functional	MO6[13]	PBE0[14]	WB97x[15]	wB2PLYP [16]	wB2GPPLYP [16]
Main advantage of functional	Metallic based chemistry and noncovalent interactions	Valid for many systems and parameter free	Long range charge transfer excitation	Most accurate for electronic excitation energies	Variant of wB2PLYP
Promise for current Study	Electronic excitation energies accuracy	Compatibility with system of interest and ease of calculation	CT state energy accuracy	Excited state accuracy	Excited state accuracy
Calculated Bandgap (eV)	1.87	1.7	5.10	5.39	5.43
Functional	**CAM B3LYP[11]**	**LC B3LYP[15]**	**SCAN Functional [17]**	**B3LYP**	**Experiment [5]**
Main advantage of functional	B3LYP with added charge transfer excitation	B3LYP with improved long range interaction	Rare-gas atoms and nonbonded interactions	Works for most systems with experimental parameterisation	
Promise in current Study	CT state energy accuracy	Improved intermolecular electronic interaction accuracy	Accurate at lower computational cost	Compatibility with system of interest and ease of calculation	
Calculated Bandgap (eV)	3.53	5.09	0.57	**1.47**	**1.56**

6.1.3 Density of states (DOS)

The electronic density of states has been introduced previously in this study briefly in Chapter **1** section **1.5**. To summarise, the density of states of an OPV system was suggested to have an important role in bimolecular recombination[18, 19], with in particular the tail states of the density of states suggested to play an important role. Recently however our previous paper[5] outlined how these tail states were not the primary cause of charge trapping in bimolecular recombination but instead the broadening of the DOS may also have a strong influence on bimolecular recombination trapping. Moreover, a study[20] by T. Linderl *et al.* found crystalline regions to deviate from the traditional gaussian DOS model whereas amorphous regions followed the established model very well.

The DOS is experimentally measured though techniques such as Ambient Photoemission spectroscopy (APS). APS is limited however, in that only the first

HOMO level is visible[21]. Comparisons with DFT calculated DOS are furthermore limited in that APS measures the HOMO-LUMO response for oligomers comprised of upwards of 20 molecule units[22] while DFT is limited by computational capabilities to only around 10 for the smaller molecules[23]. Within this study calculations are limited to the dimer form due to computational costs in addition to accuracy concerns. Calculations of DOS remain relevant to gauge the effects of external factors (such as the blending of donor and acceptor) and interactions within the orbitals of the donor and acceptor.

6.1.4 Aim and Workflow

While DFT and TDDFT have been established as powerful but limited tools to describe OPV photophysical properties, they are used in this study for two separate aims. The first aimed at comparing the ZZ115 molecule, in its dimer form, with PCPDTTTz and Si-PCPDTBT. Therein the orbital energies, DOS and excited state transitions would be compared and notable differences between the three characterised. In a second aim, calculations on blend systems studied in Chapter **3** and **4** were performed to provide insight on charge generation and bimolecular recombination kinetic differences caused by the introduction of $PC_{60}BM$ vs $PC_{70}BM$ on ZZ115. Additionally, the ZZ115:$PC_{60}BM$ blend was compared to both PCPDTTTz:$PC_{60}BM$ and Si-PCPDTBT:$PC_{60}BM$ to gauge the impact of the fullerene molecule on the three donor molecules.

6.2 Dimer Calculations

Using the same calculation methodology (B3LYP/DEF2-SVP level of theory) as ZZ115 detailed in Section **5.3** of Chapter **5**, including using the dimer form of the polymer, the resulting relaxed structure for both PCPDTTTz and Si-PCPDTBT are shown in ***Figure 6-3***. The dimer forms were chosen even for Si-PCPDTBT for consistency with previous calculations on ZZ115 in Chapter **5**. As with ZZ115 calculations the side chains were removed for decreased computational load. For the sake of clarity all donor molecules will be called by their full names even when only using their dimer forms.

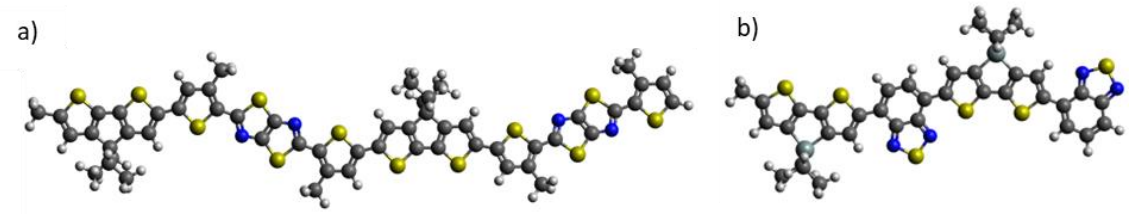

Figure 6-3: *Representation of* ***a)*** *PCPDTTTz dimer molecule and b) Si-PCPDTBT dimer molecule used in calculations rendered in the Avogadro software.*

As can be expected, the resulting PCPDTTTz dimer is extremely close to the ZZ115 structure, with deviations in dihedral angles of less than 5° and identical bond lengths barring a shortening of the bond length with the central donor atom on the dithienosilole (or carbon equivalent) unit (1.53 Å for C-C bond length in PCPDTTTz vs 1.90 Å for Si-C bond length in ZZ115 and Si-PCPDTBT). On the other hand, Si-PCPDTBT exhibits a similar planar structure with the donor dithienosilole unit behaving identically to ZZ115. Thus, there appears to be no major structural difference between the three donor molecules.

6.2.1 Ground state calculations: density of states

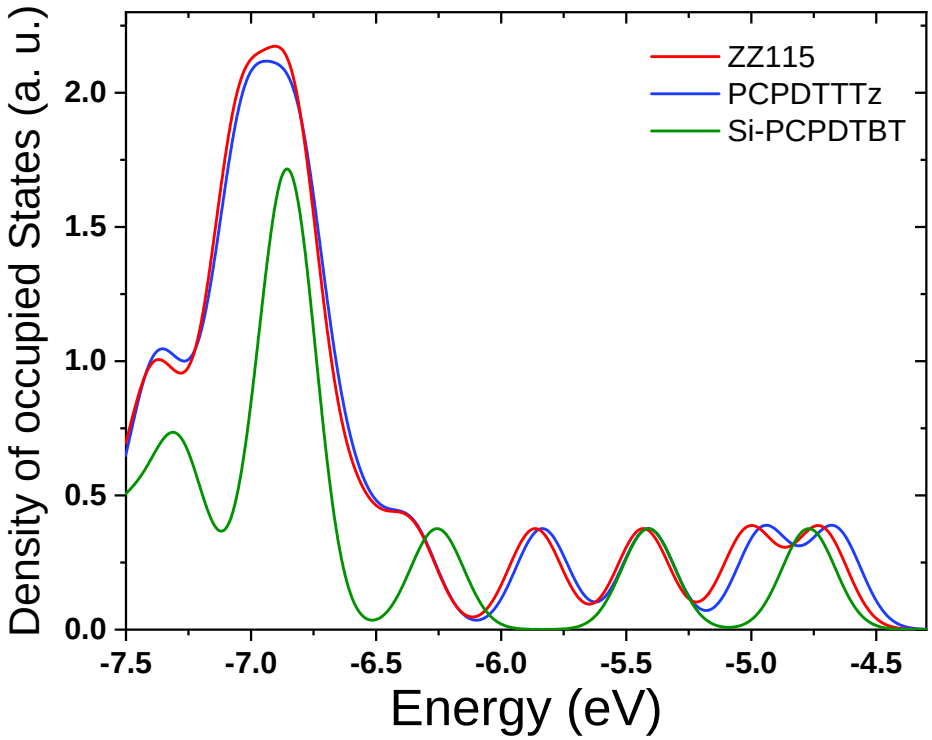

Figure 6-4: *Density of states of ZZ115, PCPDTTTz ZZ115 and Si-PCPDTBT for the first set of occupied orbitals.*

A first look at the different calculated orbitals in the DOS as seen in ***Figure 6-4*** reveals strong similarities between ZZ115 and PCPDTTTz, with the main discrepancy lying

in a 0.5 eV shift in energy of the HOMO and HOMO-1. In contrast, Si-PCPDTBT differs significantly in DOS with HOMO levels more energetically separated. The substitution of the silicon atom with carbon in ZZ115 does not appear to have a significant impact on the overall orbital energies but the substitution of the thiazolothiazole acceptor unit in ZZ115 to the shorter benzothiadiazole unit leads to widely separated molecular orbitals, most likely owning from the deeper HOMO levels of the thiazolothiazole unit[24, 25].

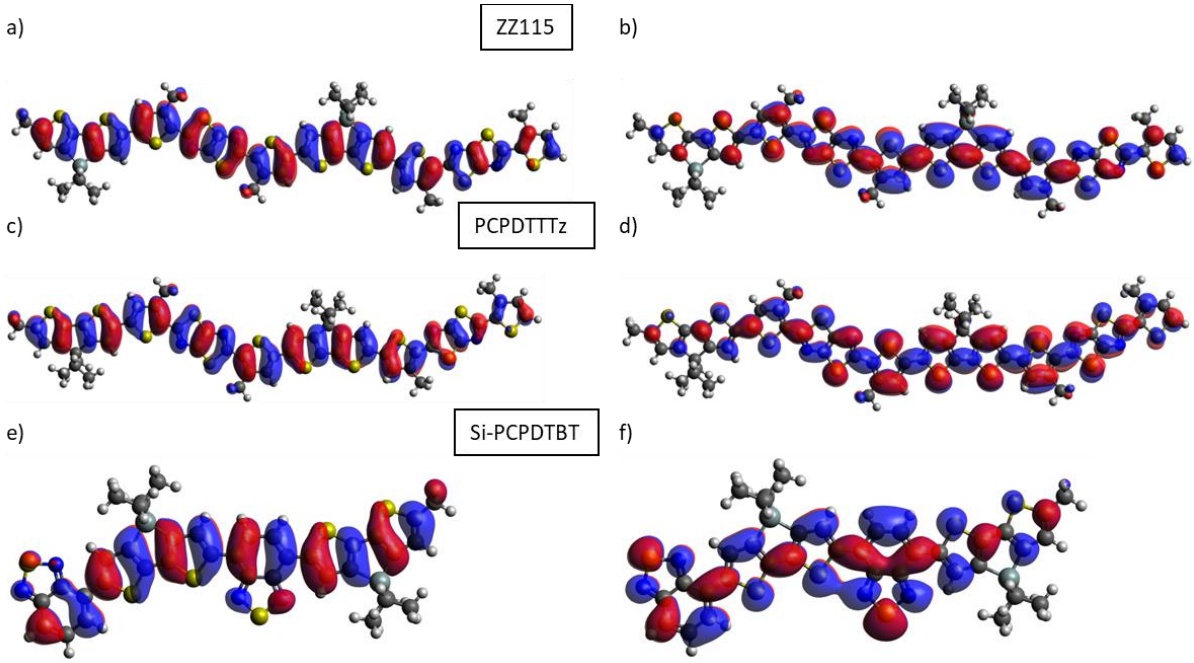

***Figure 6-5**: 3D representation of ZZ115 **a)** HOMO and **b)** LUMO orbitals, PCPDTTTz **c)** HOMO and **d)** LUMO orbitals and Si-PCPDTBT **e)** HOMO and **f)** LUMO orbitals. With the blue and red colours indicating isosurfaces with ±0.01 for all orbitals, visualised using the Avogadro software*

A look at the HOMO and LUMO orbital shapes for all three molecules of interest represented in ***Figure 6-5*** reveals an identical orbital shape behaviour with a strong overall conjugation characteristic of OPV materials and the HOMO to LUMO transition characterised by a π to π* orbital shape transition seen as an aromatic to quinoidal orbital shape transition. Therefore, differences in molecular composition (silicon to carbon substitution or acceptor unit substitution) do not seem to have an effect on the main pristine dimer orbitals.

6.2.2 Excited state calculations

Excited state calculations were performed using ZINDO/s for ease of calculation with a geometry using B3LYP/DEF2-SVP level of theory. This method was found to lead to fairly accurate modelling of long range interactions at a good computational cost

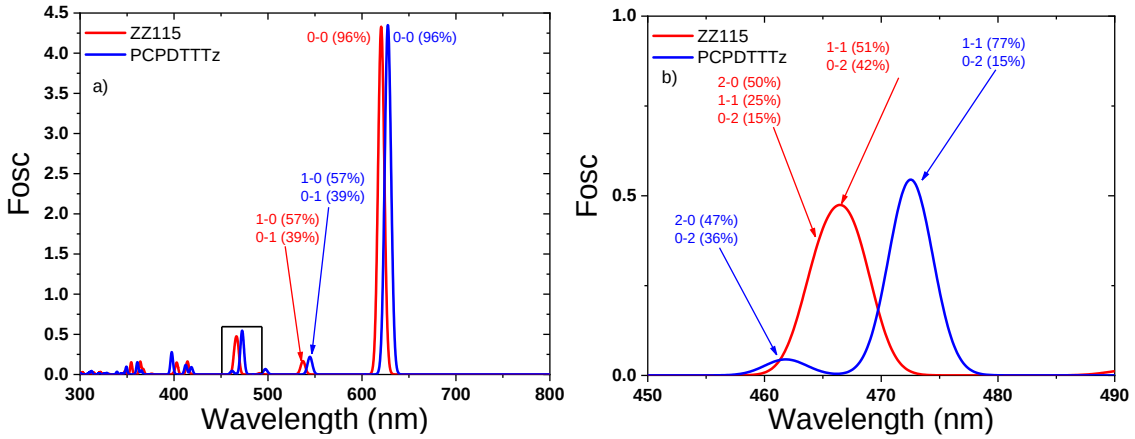

***Figure 6-6**: Calculated absorption spectrum for ZZ115 and PCPDTTTz with associated transitions from HOMO to LUMO levels (0-0 = HOMO-LUMO). **a)** shows the full spectrum with the orbital transitions associated with the first two excited state transitions **b)** shows an inset of 450nm to 490nm with the orbital transitions associated with the visible excited state transitions*

The excited state transitions of both ZZ115 and PCPDTTTz seen in ***Figure 6-6a*** behave very similarly, consistent with experimental measurements[2]. Swapping the bridge atom from silicon to carbon leads a general red shift of 7 nm in absorption for the largest excited state transitions, resulting from the slight energy difference of 0.5 eV in the HOMO between the two molecules affecting the transitions where the HOMO and HOMO-1 is involved. At the smaller wavelengths, however, more significant differences are observed. Most notably the 465nm peak in ZZ115, comprised of two degenerate excited states, splits in two more spaced out excited states with different associated transitions (the 463 nm state in ZZ115 is composed of a HOMO-2 to LUMO transition at 50%, a HOMO-1 to LUMO+1 transition at 25%, and a HOMO to LUMO+2 at 15% compared to the 461 nm state in PCPDTTTz composed of a HOMO-2 to LUMO at 47% and HOMO to LUMO+2 at 36%). Inspecting the orbitals associated with the 4th energy state as seen in ***Figure 6-7*** shows close to identical orbital shapes for both orbital transitions with the only difference between the two molecules residing in the transition contribution shifting from 54% HOMO-1 to LUMO+1 for ZZ115 to 77% for PCPDTTTz. It would therefore appear

that differences in orbital transitions seen between ZZ115 and PCPDTTTz stem more favourable HOMO and HOMO-1 based orbitals transitions in PCPDTTTz from the higher energies of the HOMO and HOMO-1 levels. These differences remain relatively minor and overall the two molecules behave very similarly at the excited state level.

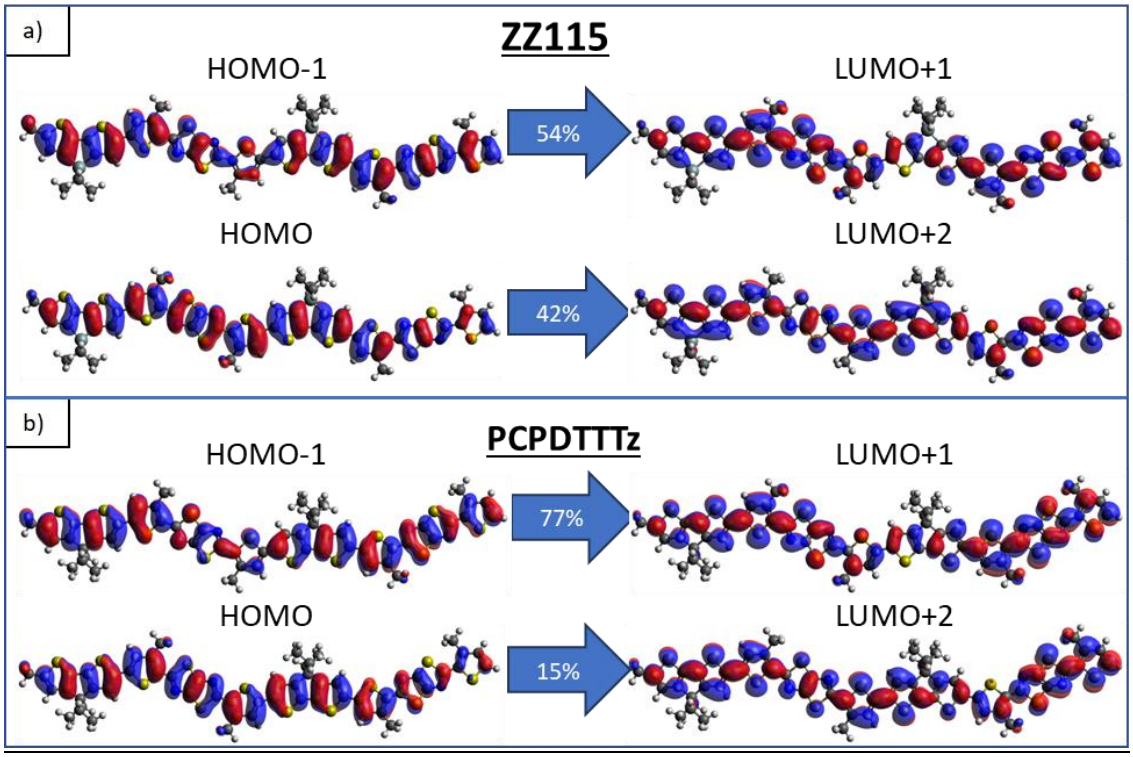

Figure 6-7: *Calculated orbitals associated with the* ***a)*** *467.6nm excited state in ZZ115 and the* ***b)*** *472.5nm excited state in PCPDTTTz.*

In comparison to the above donor molecules the absorption spectrum of Si-PCPDTBT is given in ***Figure 6-8***.

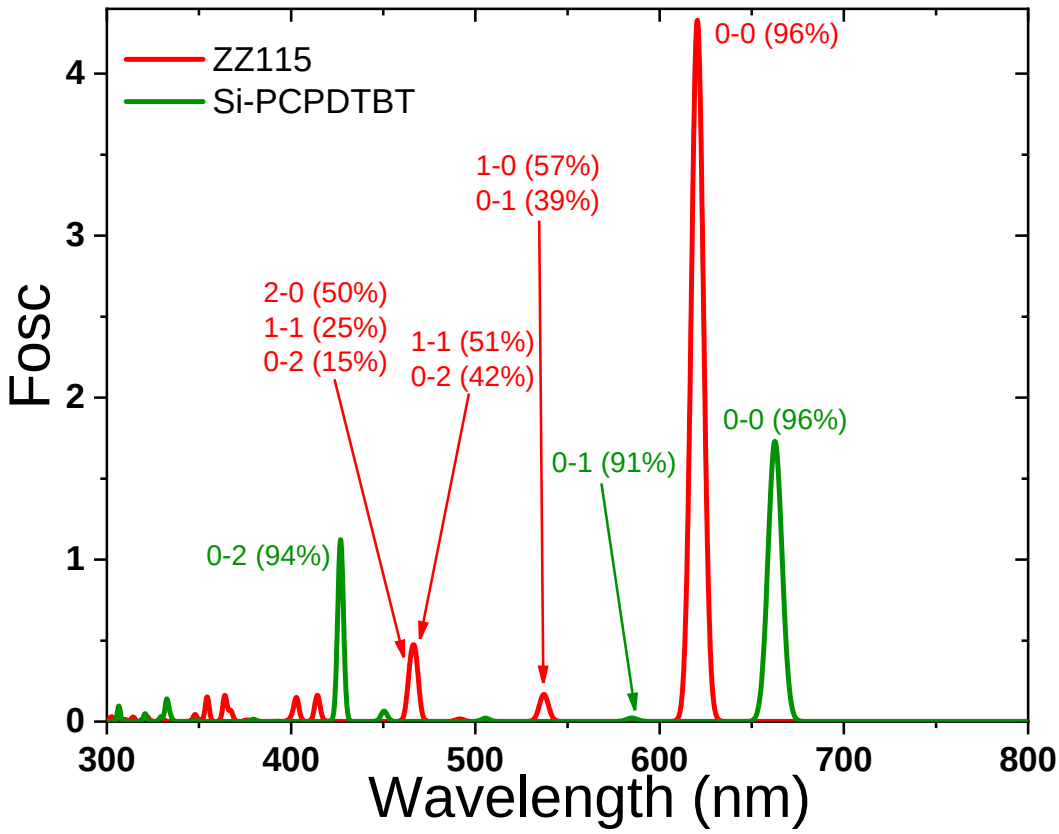

Figure 6-8: *Calculated absorption spectrum of Si-PCPDTBT and ZZ115 with associated transitions from HOMO to LUMO levels (0-0 = HOMO-LUMO).*

An initial look at the calculated absorption spectrum reveals major differences between the Si-PCPDTBT and ZZ115 donor molecules, most notably a larger focus on transitions from the HOMO level in Si-PCPDTBT. As Si-PCPDTBT is characterised by wide gaps between HOMO levels from ***Figure 6-4***, transitions involving higher occupied orbital levels would be restricted to higher energies. Si-PCPDTBT therefore behaves very differently at the excited state level showing clear well-defined transitions. Having established the ground state and the excited state profile of the three donor molecules of interest calculations on the blend were performed.

6.3 Blend Calculations

6.3.1 Relaxed structure

The interactions of ZZ115 dimer and $PC_{60}BM$ were studied first. These calculations aimed to find the best configuration for the two molecules in terms of intermolecular distance and position. The methodology used for finding the relaxed configuration

was the following. The relaxed individual molecules of ZZ115 and $PC_{60}BM$ calculated in Chapter **5** Section **5.3** were taken and assembled to a starting configuration**.** Using B3LYP/DEF2-SVP level of theory the structure was relaxed. The energy of the system was then calculated with the intermolecular distance and position along the molecule varying. The resulting variation in intermolecular dimer energy is described in ***Figure 6-9***.

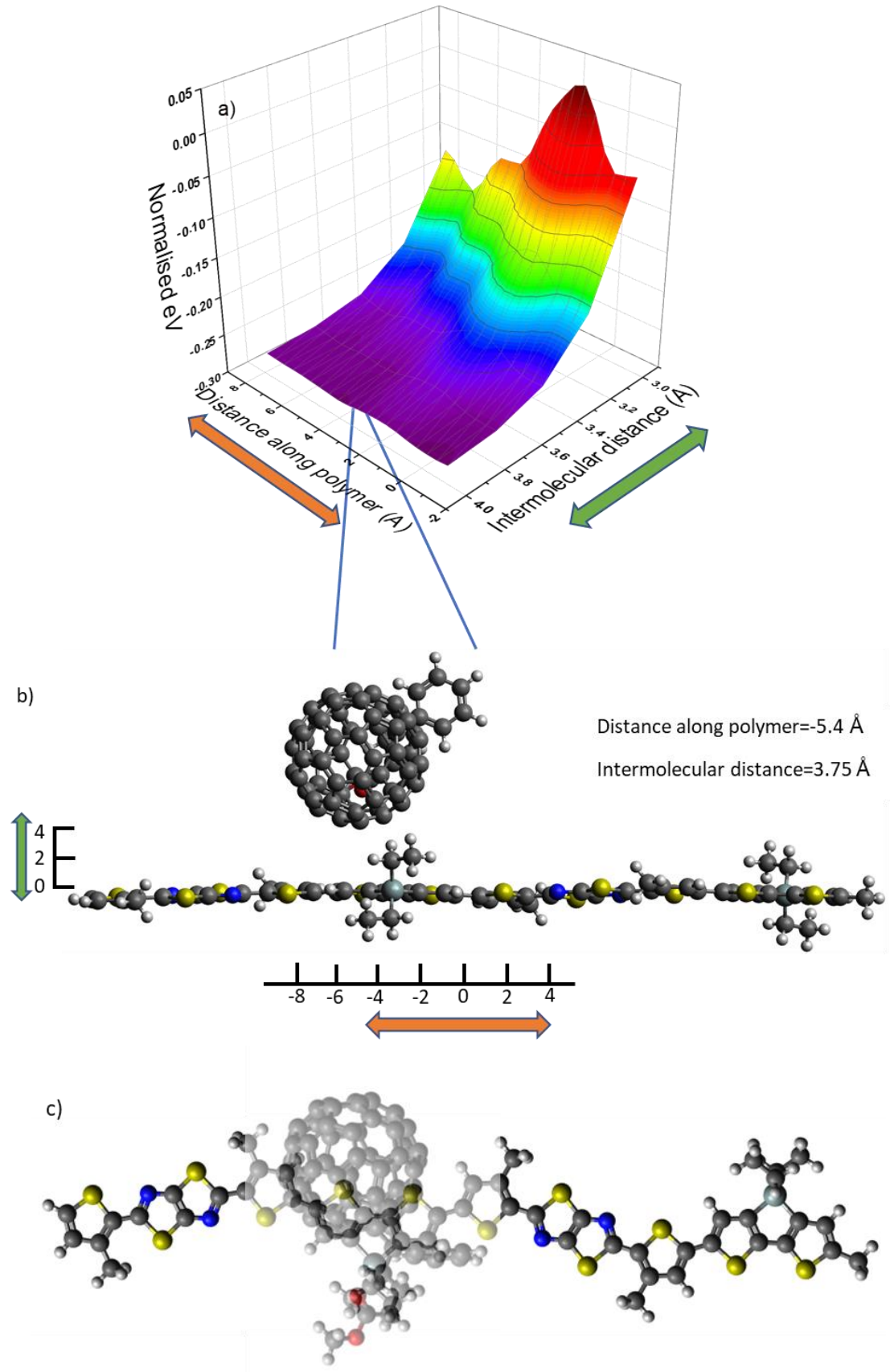

Figure 6-9: *a) 3D graph of calculated internal energy against varying intermolecular distance and varying distance along the ZZ115 molecule with inset of highest energy configuration. b) Representation of ZZ115:$PC_{60}BM$ system calculated to be the lowest energy configuration rendered in the Avogadro software, c) view from the side illustrating the placement of the $PC_{60}BM$ molecule along ZZ115.*

The 3D distance scan shows a minimum system obtained with an intermolecular distance of 4 Å between ZZ115 and $PC_{60}BM$, with a $PC_{60}BM$ molecule position as shown in ***Figure 6-9bc***. This configuration sees the fullerene positioned close to centred on the dithienosilole donor unit. The absolute minimum energy configuration was found at 4 Å the difference in energy is minimal. More importantly, ZZ115 π-π stacking distance was experimentally measured to be around 3.7Å[2] while the P3HT-$PC_{60}BM$ intermolecular distance was found to be 3.5 Å[26]. Considering the difference in energy between 4 Å and 3.75 Å as seen in ***Figure 6-9a*** is around 0.006 eV and no dispersion correction was used, the observed discrepancy in energy can be considered to be within calculation uncertainty range[8]. Both 4 Å and 3.75 Å configurations were used in ground state and excited calculations and no major differences in orbital energies, shapes and excited state transitions were found. Thus, for the rest of this study the intermolecular distance of 3.75 Å was used. Of note the highest energy configuration has the $PC_{60}BM$ molecule 3 Å from ZZ115 and completely on the donor dithienosilole unit, while the lowest energy configuration at an intermolecular distance of 3 Å has the $PC_{60}BM$ molecule closer to the acceptor unit, highlighting the unfavourable nature of the interaction.

As with ZZ115:$PC_{60}BM$, calculations were performed on ZZ115:$PC_{70}BM$, PCPDTTTz:$PC_{60}BM$ and Si-PCPDTBT:$PC_{60}BM$. The minimum energy configuration was calculated using the same methodology as for ZZ115:$PC_{60}BM$, resulting in the configurations shown in ***Figure 6-10***.

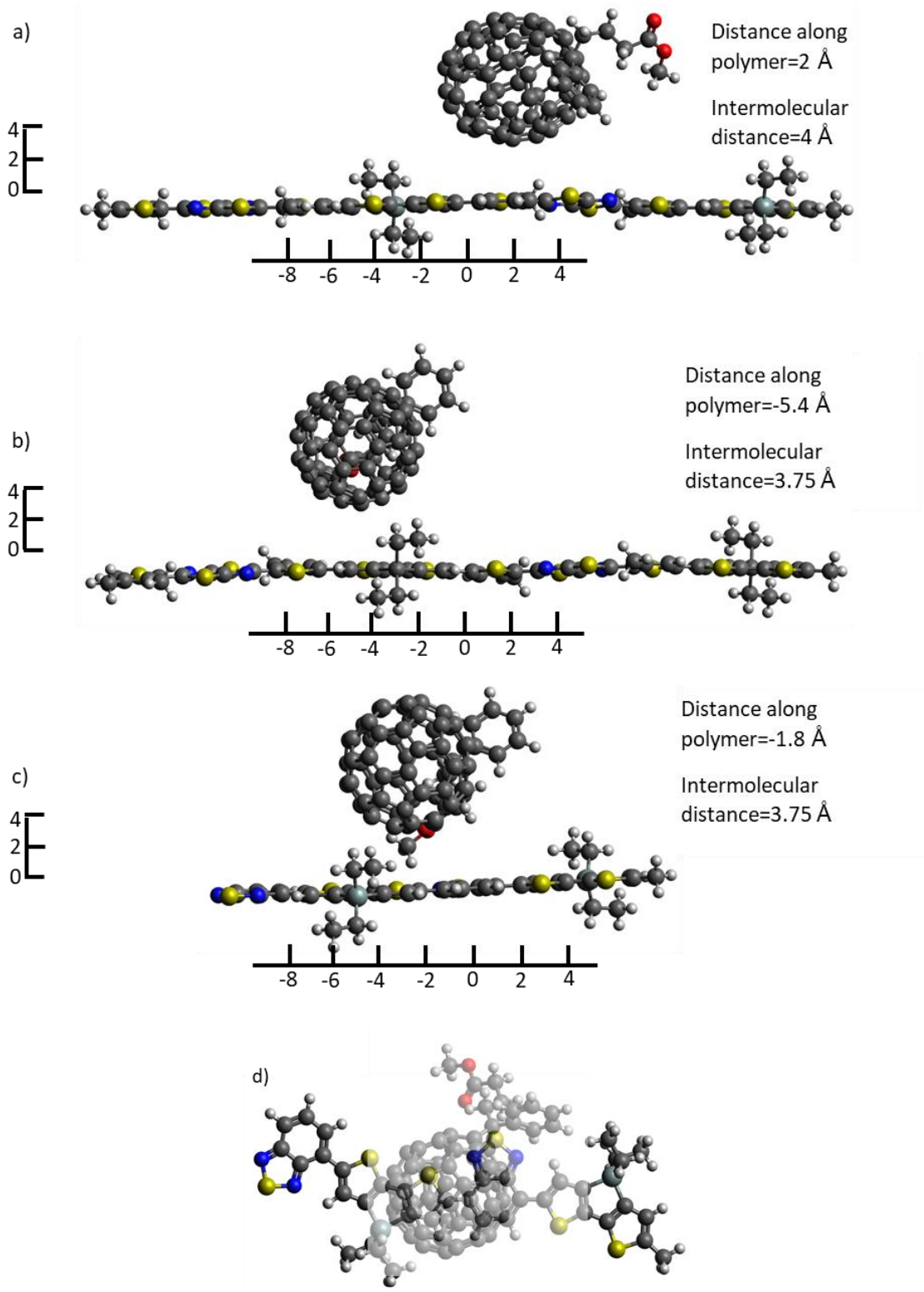

***Figure 6-10**: a) Representation of ZZ115:PC$_{70}$BM system used in calculations rendered in the Avogadro software. **b)** and **c)** show similar types of representations for PCPDTTTz:PC60BM and Si-PCPDTBT:PC60BM respectively. **d)** view from the side for the Si-PCPDTBT:PC$_{60}$BM system illustrating the placement of the PC$_{60}$BM molecule along Si-PCPDTBT*

Looking first in ***Figure 6-10a*** at ZZ115:PC$_{70}$BM, the configuration represented has a few differences with the ZZ115:PC$_{60}$BM configuration seen in ***Figure 6-9b***, with the

intermolecular distance being comparable (3.75 Å vs 4 Å) but the position of the fullerene is significantly different, appearing further from the dithienosilole unit. This highly suggests that the dithienosilole unit has lower HOMO contributions or plays a smaller role in the ZZ115:$PC_{70}BM$ system. Moving to the PCPDTTTz:$PC_{60}BM$ with ***Figure 6-10b***, even with the silicon atom replaced by a carbon atom the overall system remains similar in terms of distance along polymer and intermolecular distance suggesting a great degree of similarity in molecular interactions with $PC_{60}BM$. Finally, the Si-PCPDTBT:$PC_{60}BM$ shown in ***Figure 6-10c-d*** sees the $PC_{60}BM$ molecule on the other side of the dithienosilole unit when compared to ZZ115:$PC_{60}BM$. This structure may arise from the shortened molecule length leading to the fullerene molecule finding a more preferable configuration closer to the centre. Irregardless the fullerene finds itself close to the dithienosilole donor unit just as with ZZ115.

6.3.2 Ground state calculations: density of states

Having found the minimum energy structural configurations for all four systems of interest the molecular orbitals were analysed as summarised in ***Figure 6-11***.

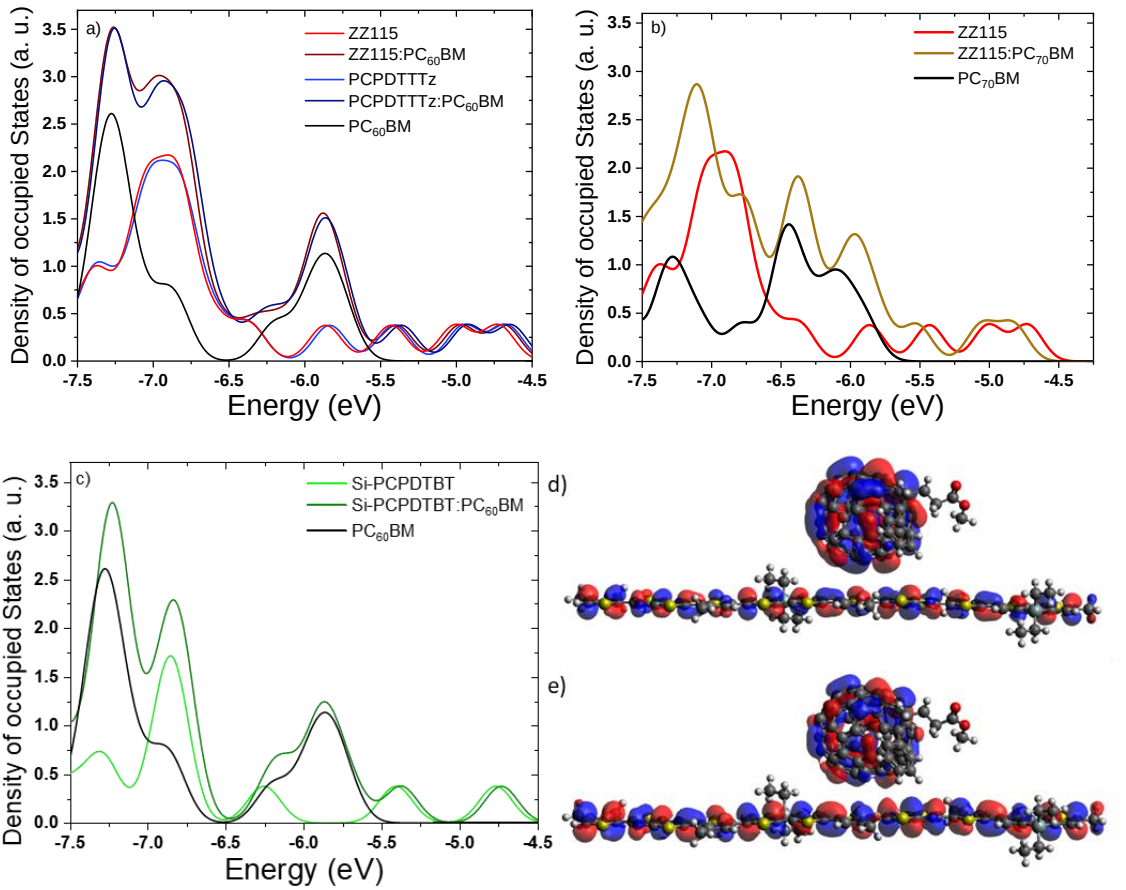

Figure 6-11: a) *Density of states of ZZ115, PC60BM, PCPDTTTz, ZZ115:PC60BM and PCPDTTTz:PC60BM.* ***b).*** *Density of states of ZZ115, PC70BM and ZZ115:PC70BM* ***c)*** *Density of states of Si-PCPDTBT, PC60BM and Si-PCPDTBT:PC60BM, 3D representation of ZZ115:PC70BM* ***d)*** *HOMO-4 and* ***e)*** *HOMO-5. With the blue and red colours indicating isosurfaces with ±0.01 for all orbitals, visualised using the Avogadro software*

The calculated orbitals show the ZZ115:PC60BM system effectively has the same orbitals as each separate molecule with little to no intermolecular interaction, with the resulting blend DOS appearing in ***Figure 6-11a*** as combination of ZZ115 DOS and PC60BM DOS. Switching the silicon atom for a carbon atom reveals very close similarities between the two blends with the only difference residing in a slight shift to higher energies for the PCPDTTTz:PC60BM DOS, consistent with HOMO calculations on the pristine PCPDTTTz. In contrast substitution of the PC60BM with PC70BM reveals a very different molecular orbital behaviour, illustrated in ***Figure 6-11b*** by the DOS of the blend not summarised as a combination of the ZZ115 and

$PC_{70}BM$ DOS. The shift in HOMO and HOMO-1 to deeper energies suggests a significant disruption of the occupied orbitals by the $PC_{70}BM$. Inspection of the orbital shapes revealed an intermolecular close to hybridised orbital in the HOMO-4 (5.92eV) and HOMO-5 (5.96eV) shown in ***Figure 6-11d-e,*** highlighting the increased intermolecular electronic interaction with addition of $PC_{70}BM$ and confirming a delocalisation of the HOMO caused by $PC_{70}BM$. Conversely, addition of $PC_{60}BM$ does not change the DOS of Si-PCPDTBT as the resulting DOS seen in ***Figure 6-11c*** appears close to the sum of both separate DOS. As with ZZ115 and PCPDTTTz, no significant electronic intermolecular interaction was found between Si-PCPDTBT and $PC_{60}BM$ on the ground state level.

6.3.3 Excited state calculation

Having characterised the ground state of the four systems of interest, TDDFT calculations were done using the same methodology as the lone dimer molecules.

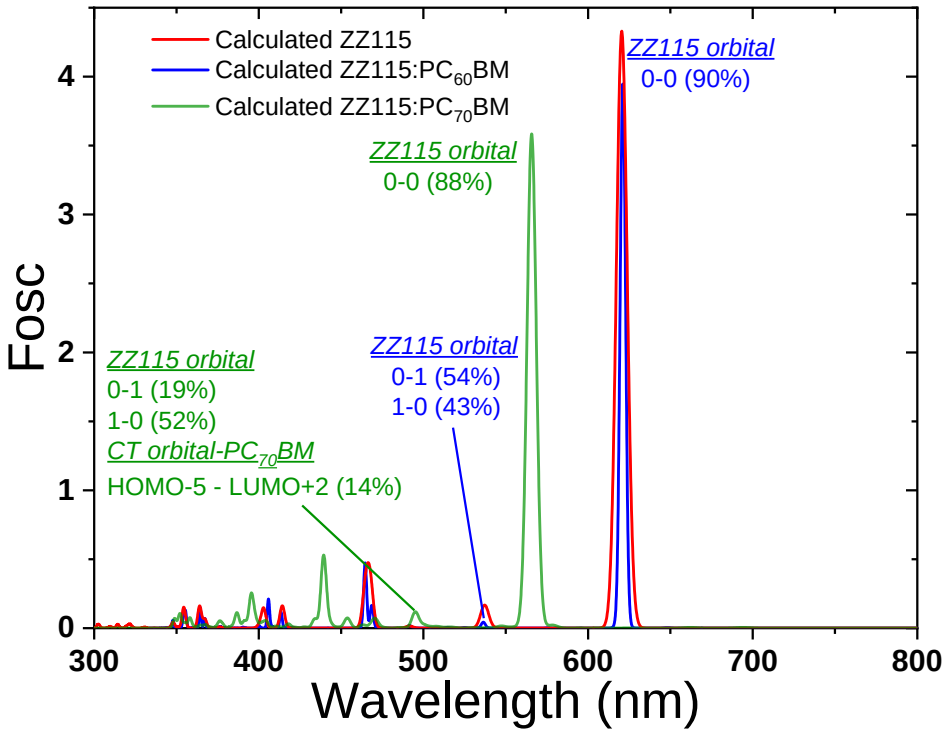

Figure 6-12: *Calculated absorption spectrum of ZZ115:$PC_{70}BM$ compared to calculated ZZ115 and ZZ115:$PC_{60}BM$ spectrum with the main electronic orbital transitions of the first two principle states. The orbital transitions are given in equivalent molecule HOMO and LUMO levels, such that the HOMO to LUMO+3 orbital transition occurring in ZZ115:$PC_{60}BM$ at 621nm reads as the equivalent of the HOMO to LUMO transition in ZZ115*

ZZ115:$PC_{60}BM$ excited states as seen in ***Figure 6-12*** show very little difference between the lone dimer and the blend system, with the most prominent peak at 621 nm and the second peak at 530 nm being identical between the ZZ115 pristine and the ZZ115:$PC_{60}BM$ blend in terms of position and orbital transitions. In contrast, the absorption spectrum reveals a predictably very different excited state behaviour for ZZ115:$PC_{70}BM$ when compared to ZZ115:$PC_{60}BM$. The ZZ115 HOMO to LUMO peak is blue shifted from 620 nm to 565 nm while decreasing in amplitude by 12%, a predictable observation given the HOMO shift found in the DOS of ZZ115:$PC_{70}BM$. The states at 530 nm and 495 nm for ZZ115:$PC_{60}BM$ and ZZ115:$PC_{70}BM$ respectively reveal the critical impact of fullerene substitution as the ZZ115:$PC_{70}BM$ 495 nm excited state has a partial CT character with a small but consequential transition from the intermolecular orbital HOMO-5 to the equivalent of the $PC_{60}BM$ LUMO+2. While the peak intensities of these secondary states may seem small in comparison to the 621 nm and 530 nm peaks, they remain relevant as an excitation wavelength of 500 nm was chosen for PL and TAS measurements of Chapters 3 and 4. Looking at the orbital shapes of the transitions associated with the 530 nm and 495 nm states in ***Figure 6-13*** reveals close to identical ZZ115 based HOMOs and LUMOs in the blends compared to the lone dimer seen in ***Figure 6-7*** regardless of the choice of fullerene. The intermolecular orbital transition of HOMO-5 to $PC_{70}BM$ LUMO+2 appears to be a combination of the ZZ115 aromatic HOMO delocalised onto the $PC_{70}BM$ aromatic HOMO, transitioning to a pure $PC_{70}BM$ quinoidal orbital shape. It would thus appear that $PC_{70}BM$ actively delocalises the ZZ115 HOMO and has a stronger electronic influence on the excited states of ZZ115 than $PC_{60}BM$.

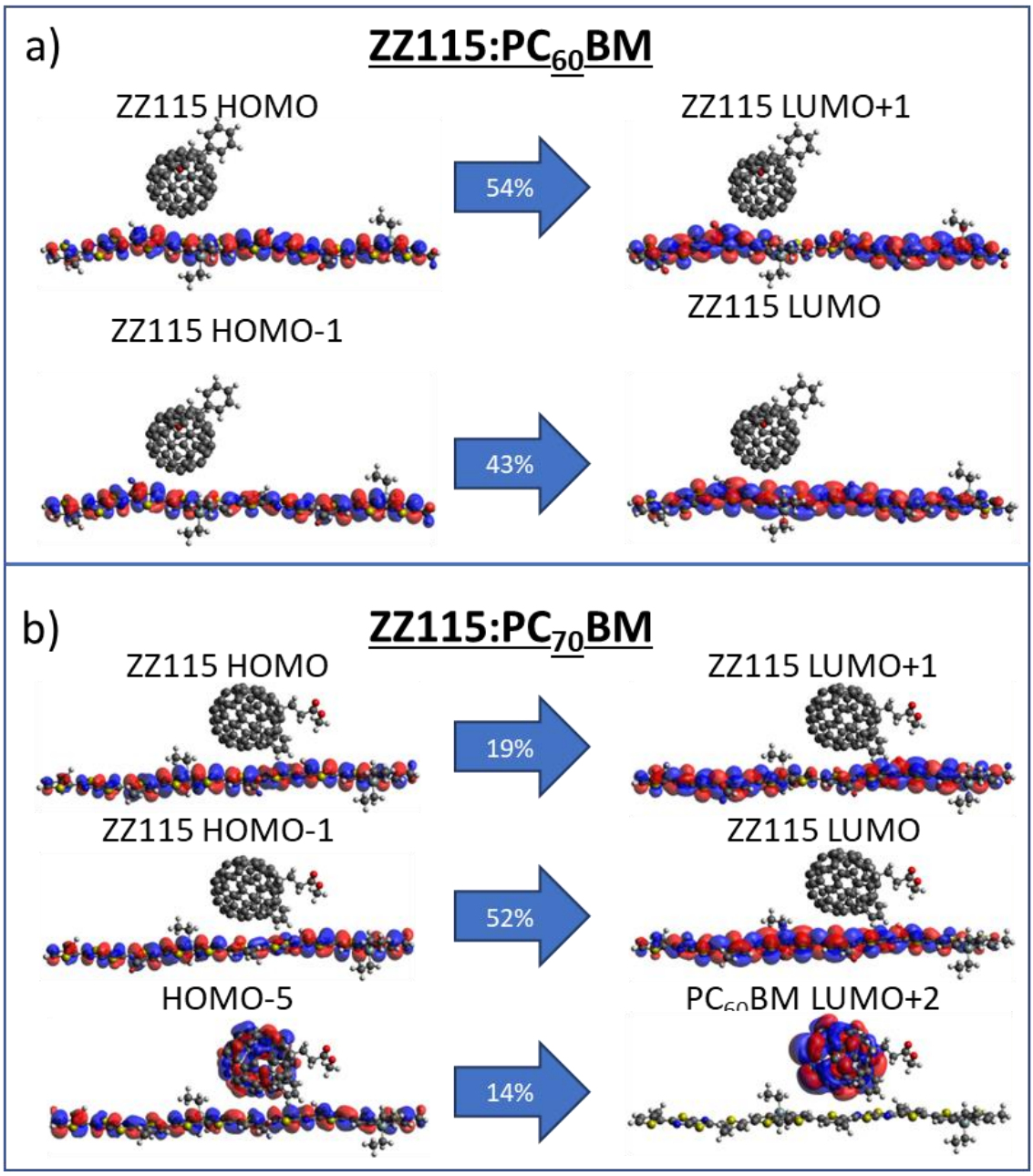

Figure 6-13: *Calculated orbitals and transition contributions associated with the* ***a)*** *530nm excited state in ZZ115:PC60BM and the* ***b)*** *495nm excited state in ZZ115:PC70BM. With the blue and red colours indicating isosurfaces with ±0.01 for all orbitals, visualised using the Avogadro software*

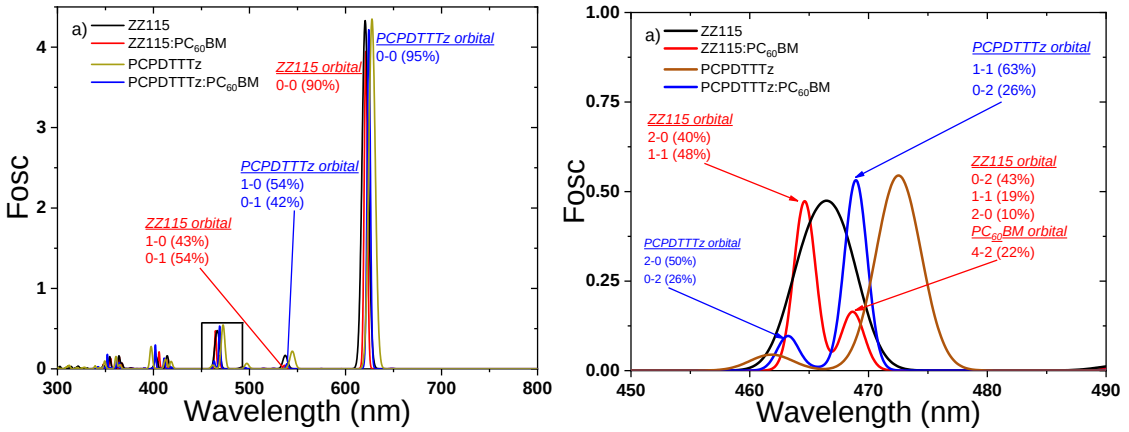

Figure 6-14: *a) Calculated absorption spectrum of ZZ115, PCPDTTTz and ZZ115:PC60BM compared to PCPDTTTz:PC60BM. b) Inset of graph a). The orbital transitions are given in equivalent molecule HOMO and LUMO levels, such that the HOMO to LUMO+3 orbital transition occurring in ZZ115:PC60BM at 621nm reads as the equivalent of the HOMO to LUMO transition in ZZ115*

Comparing the ZZ115:PC60BM and PCPDTTTz:PC60BM excited states shows a relatively similar absorption spectrum as seen in ***Figure 6-14a*** with the first two excited states predictably identical in intensity and orbital transition contribution. The excited states at the 460-470 nm range shown in ***Figure 6-14b*** show a critical difference with the ZZ115 degenerate excited states at 465 nm splitting into two states, with the 472 nm excited state now comprised of PC60BM HOMO-4 to LUMO+2 transition. The resulting orbital transition would therefore have a delocalisation from the ZZ115 onto the PC60BM. This delocalisation however appears less pronounced than in ZZ115:PC70BM due to the excited state transition having a lower intensity and wavelength. In contrast PCPDTTTz has the same equivalent transitions as the lone PCPDTTTz dimer as seen ***Figure 6-6***, with the only difference residing in a slight shift in wavelength due to a slight shift in HOMO energies. It stands thus that on the excited state level both ZZ115 and PCPDTTTz behave very similarly when blended with PC60BM, however at high energies ZZ115 has its HOMO delocalised by PC60BM when PCPDTTTz does not, suggesting an enhanced intermolecular interaction at the excited state level caused by carbon to silicon substitution.

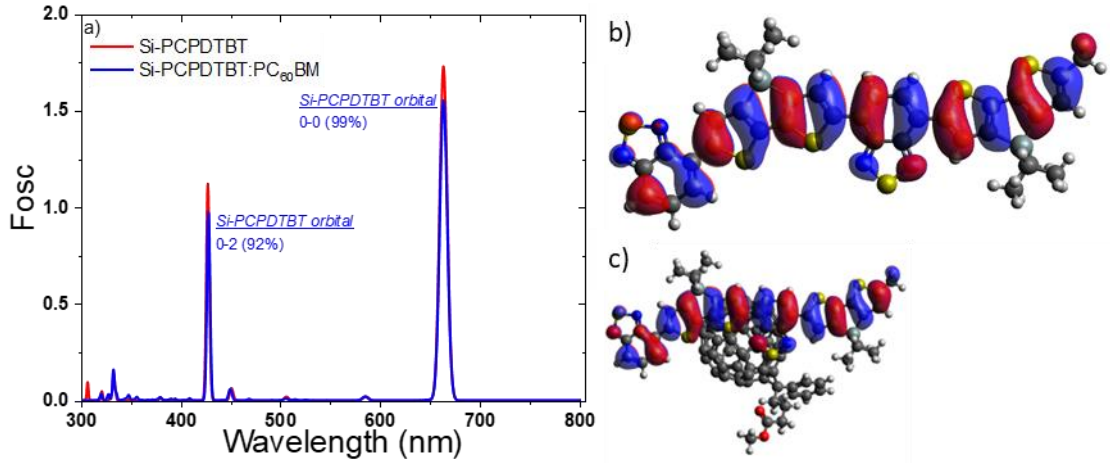

Figure 6-15: *Calculated absorption spectrum of Si-PCPDTBT:PC60BM compared to the calculated Si-PCPDTBT spectrum 3D representation of* ***b)****Si-PCPDTBT HOMO and* ***c)*** *Si-PCPDTBT:PC60BM HOMO. With the blue and red colours indicating isosurfaces with ±0.01 for all orbitals, visualised using the Avogadro software. The orbital transitions are given in equivalent molecule HOMO and LUMO levels, such that the HOMO to LUMO+3 orbital transition occurring in Si-PCPDTBT:PC60BM at 662nm reads as the equivalent of the HOMO to LUMO transition in Si-PCPDTBT*

In contrast with ZZ115 and PCPDTTTz, Si-PCPDTBT shows no interaction with $PC_{60}BM$ in excited states as seen in ***Figure 6-15a,*** as the main excited states are purely comprised of Si-PCPDTBT orbital transitions and barring a slight decrease in intensity the peaks are practically identical between Si-PCPDTBT and Si-PCPDTBT:$PC_{60}BM$. The lack of interaction is corroborated by the lack of orbital shape difference as illustrated by ***Figure 6-15b-c***. The lack of interaction measured strongly suggests that from a fundamental electronic perspective the dithienosilole donor unit is not the critical part of ZZ115 allowing electronic intermolecular interaction between ZZ115 and $PC_{60}BM$.

6.4 Discussion

The present study changed the donor molecule to gauge the effect of the silicon based dithienosilole unit on the electronic properties of the ZZ115 molecule. Studies mentioned previously [1-4] have highlighted morphological effects of the substitution of the bridging atom from carbon to silicon. Both studies by M. Morana *et al.* and M. C. Scharber *et al.* on Si-PCPDTBT and its carbon analogue have shown a suppression of charge-transfer character in the silicon analogue as compared to the carbon. T. Clarke *et al.* have in two separate studies shown a similar observation with ZZ115 and

PCPDTTTz, finding the carbon analogue to have a more pronounced CT character. The faster CT dissociation in ZZ115[2] as compared to PCPDTTTz and Si-PCPDTBT could be explained by the enhanced intermolecular electronic interaction between ZZ115 and $PC_{60}BM$ seen in ***Figure 6-14*** and ***Figure 6-15*** as the CT state would more easily dissociate due to a more favourable interaction with the singlet states. This hypothesis is reinforced by the lack of change in this fast CT state from morphological changes such as introduction of DIO, suggesting a more electronic factor.

Conversely, findings of this present study seemingly stand in contrast with our previous paper[5] comparing Si-PCPDTBT and ZZ115 when blended with $PC_{60}BM$. Therein the HOMO was hypothesised to localise onto the dithienosilole donor unit with addition of $PC_{60}BM$, a phenomenon not observed in ***Figure 6-15*** and study at large. These comparisons are however hampered by the limitations of DFT and in particular the size of the studied systems (the modelled ZZ115:$PC_{70}BM$ system has over 200 atoms, close to the limit of the ORCA software) possibly leading to misestimation of the orbital shapes energies. Even with these limitations, this study's findings could suggest the possibility of the dithienosilole donor unit having longer range effects that could possibly result in HOMO localisation such as interchain effects or π-π stacking[27] instead of a fundamental electronic interaction as seen with ZZ115:$PC_{70}BM$ in ***Figure 6-12***.

The critical finding in this chapter lies in the contrast in ZZ115 electronic interactions with $PC_{60}BM$ and $PC_{70}BM$. Chapter **3** and **4** highlighted a change in charge generation and bimolecular recombination kinetics between the two blends. A given hypothesis was the $PC_{70}BM$ acting to delocalise the ZZ115 HOMO onto the fullerene, slowing bimolecular recombination while hampering charge generation. The presence of the intermolecular HOMO-4 and HOMO-5 caused by delocalisation of the ZZ115 HOMO onto the $PC_{70}BM$ as seen in ***Figure 6-11d-e*** and presence of an excited state involving the HOMO-5 at the 500 nm as seen in ***Figure 6-12*** would therefore be in line with the given hypothesis. The lower energy excited state with CT character found at 495 nm in ZZ115:$PC_{70}BM$ as compared to the excited state with CT character found at 465 nm in ZZ115:$PC_{60}BM$ would also illustrate a possible easier CT dissociation or recombination to a singlet state in ZZ115:$PC_{70}BM$.

6.5 Conclusion

DFT and TDDFT calculations were done on four blend systems in ZZ115:$PC_{60}BM$, ZZ115:$PC_{70}BM$, PCPDTTTz:$PC_{60}BM$ and Si-PCPDTBT:$PC_{60}BM$ in an effort to understand the inherent properties of ZZ115 and to complement previous findings in Chapter **3** and **4**. Ground state calculations found the ZZ115, PCPDTBT and Si-PCPDTBT show similar behaviour when blended with $PC_{60}BM$, with a limited electronic interaction between donor and acceptor. In contrast ZZ115:$PC_{70}BM$ showed significant intermolecular electronic interaction with the presence of intermolecular orbitals, highlighting the larger impact of the $PC_{70}BM$ molecule on the electronic structure of ZZ115, in line with observations from Chapter 4. Excited state studies accentuated the impact of $PC_{70}BM$ with a CT transition observed as well as increased orbital delocalisation. The excited state studies also revealed ZZ115:$PC_{60}BM$ to have a CT character though weaker than ZZ115:$PC_{70}BM$. This was contrasted with no intermolecular interactions of the sort found for PCPTDTTTZ and Si-PCPDTBT when blended with $PC_{60}BM$.

6.6 References

1. T. M. Clarke, C. Lungenschmied, J. Peet, N. Drolet, and A.J. Mozer, *Tuning Non-Langevin Recombination in an Organic Photovoltaic Blend Using a Processing Additive.* J. Phys. Chem. C., 2015. **119**.
2. T. M. Clarke, J. Peet, C. Lungenschmied, N. Drolet, X. Lu, B. M. Ocko, . . . M.A. Loi, *The role of emissive charge transfer states in two polymer–fullerene organic photovoltaic blends: tuning charge photogeneration through the use of processing additives.* Jounal of Materials Chaemistry A, 2014(31).
3. M. Morana, H. Azimi, G. Dennler, H-J. Egelhaff, M. Scharber, K. Foberich, . . . C.J. Brabec, *Nanomorphology and Charge Generation in Bulk Heterojunctions Based on Low-Bandgap Dithiophene Polymers with Different Bridging Atoms.* Advanced Functional Materials, 2010. **20**(7).

4. M. C. Scharber, M. Koppe, J. Gao, F. Cordella, M. A. Loi, P. Denk, . . . C. J. Brabec, *Influence of the Bridging Atom on the Performance of a Low-Bandgap Bulk Heterojunction Solar Cell.* Advanced Materials, 2010. **22**(3).
5. J. Marin-Beloqui, G. Zhang, J. Guo, J. Shaikh, T. Wohrer, S. M. Hosseini, . . . T.M. Clarke, *Insight into the Origin of Trapping in Polymer/Fullerene Blends with a Systematic Alteration of the Fullerene to Higher Adducts.* The Journal of Physical Chemistry C, 2021. **126**(5): p. 2708–2719.
6. T. M. Clarke, C. Lungenschmied, J. Peet, N. Drolet, K. Sunahara, A. Furube, and A.J. Mozer, *Photodegradation in Encapsulated Silole-Based Polymer: PCBM Solar Cells Investigated using Transient Absorption Spectroscopy and Charge Extraction Measurements* Advanced Energy Materials, 2013. **3**: p. 1473-1483.
7. T. M. McCormick, C. R. Bridges, E. I. Carrera, P. M. Dicarmine, G. L. Gibson, J. Hollinger, . . . D.S. Seferos, *Conjugated Polymers: Evaluating DFT Methods for More Accurate Orbital Energy Modeling.* Macromolecules, 2013. **46**.
8. A. Wang, R. Kingsbury, M. McDermott, M. Horton, A. Jain, S. P. Ong, . . . K. A. Persson, *A framework for quantifying uncertainty in DFT energy corrections.* Scientific Reports, 2021. **11**.
9. A. Morales-Garcia, R. Valero, and F. Illas, *An Empirical, yet Practical Way To Predict the Band Gap in Solids by Using Density Functional Band Structure Calculations.* The journal of Physical Chemistry C, 2017. **121**(34).
10. J.-C. Lee, J.-D. Chai, and S.-T. Lin, *Assessment of Density Functional Methods for Exciton Binding Energies and Related Optoelectronic Properties.* 2015.
11. T. Yanai, D. P. Tew, and N. C. Handy, *A new hybrid exchange–correlation functional using the Coulomb-attenuating method (CAM-B3LYP).* Chemical Physics Letters 2004. **393**(1-3).
12. Y. Shao, Y. Mei, D. Sundholm, and V. R. I. Kaila, *Benchmarking the Performance of Time-Dependent Density Functional Theory Methods on Biochromophores.* Journal of Chemical Theory and Computation, 2020. **16**(1).

13. Y. Zhao and D. G. Truhlar, *The M06 suite of density functionals for main group thermochemistry, thermochemical kinetics, noncovalent interactions, excited states, and transition elements: two new functionals and systematic testing of four M06-class functionals and 12 other functionals.* Theoretical Chemistry Accounts, 2008. **120**.
14. J. P. Perdew, M. Ernzerhof, and K. Burke, *Rationale for mixing exact exchange with density functional approximat.* American Institute of Physics, 1996. **22**.
15. J.-D. Chai and M. Head-Gordon, *Systematic optimization of long-range corrected hybrid density functionals.* The Journal of Chemical Physics, 2008. **128**(8).
16. M. Casanova-Paez, M. B. Dardis, and L. Goerigk, *ωB2PLYP and ωB2GPPLYP: The First Two Double-Hybrid Density Functionals with Long-Range Correction Optimized for Excitation Energies.* J. Chem. Theory. Comput., 2019. **15**.
17. J. Sun, A. Ruzsinszky, and J. P. Perdew, *Strongly Constrained and Appropriately Normed Semilocal Density Functional.* Physical Review Letters, 2015. **115**.
18. J. Nelson, *Diffusion recombination in polymer-fullerene blends and its influence on photocurrent collection.* Physical Review B, 2003. **67**(15).
19. M. Hilczer and M. Tachiya, *Unified Theory of Geminate and Bulk Electron-Hole Recombination in Organic Solar Cells.* Journal of Physical Chemistry C, 2010. **114**(14).
20. T. Linderl, T. Zechel, A. Hofmann, T. Sato, S. K., H. Ishii, and W. Brutting, *Crystalline versus Amorphous Donor-Acceptor Blends: Influence of Layer Morphology on the Charge-Transfer Density of States.* Physcial Review Applied, 2020. **13**.
21. S. Krause, M. B. Casu, A. Scholl, and E. Umbach, *Determination of transport levels of organic semiconductors by UPS and IPS.* New journal of physics, 2008. **10**.

22. D. P. McMahon, D. L. Cheung, L. Goris, J. Dacuna, A. Salleo, and A. Troisi, *Relation between Microstructure and Charge Transport in Polymers of Different Regioregularity.* The Journal of Physical Chemistry C, 2011. **115**.

23. C. F. N. Marchiori and M. Koehler, *Density functional theory study of the dipole across the P3HT : PCBM complex: the role of polarization and charge transfer.* Journal of Physics D: Applied Physics, 2014. **47**.

24. I. Osaka, R. Zhang, J. Liu, D-M. Smilgies, T. Kowalewski, and R. D. McCullough, *Highly Stable Semiconducting Polymers Based on Thiazolothiazole.* Chemistry of Materials, 2010. **22**.

25. R. Misra and P. Gautam, *Tuning of the HOMO–LUMO gap of donor-substituted symmetrical and unsymmetrical benzothiadiazoles.* Organic and Biomolecular Chemistry, 2014. **29**.

26. A. W. Gotz, J. I. Rodriguez, F. L. Castillo-Alvarado, and D.E. Trujillo-Gonzalez, *Van der Waals effects on structure and optical properties in organic photovoltaics.* International Journal of Quantum Chemistry, 2019. **119**(14).

27. Z. Guom, D. Lee, R. D. Schaller, X. Zuo, B. Lee, T. Luo, . . . L. Huang, *Relationship between Interchain Interaction, Exciton Delocalization, and Charge Separation in Low-Bandgap Copolymer Blends.* Journal of the American Chemical Society, 2014. **136**.

Chapter 7:
General Conclusion

7.1 Significance of Study

From a broader perspective the results presented in this study serve as a continuation of work done on the ZZ115 polymer, which remains an intriguing species even to this day. The results found in this study provide additional insight in the inherent properties of this polymer. While ZZ115 is not a popular polymer within the broader context of the literature, its particular properties provide invaluable insight on the bimolecular process. Most notable to this study is the fullerene concentration dependence within the context of understanding the bimolecular process, as well as a kinetic characterisation of the mixed amorphous phase with a notable invariance with fullerene concentration highlighted. As such this work has provided with potential guidelines for ZZ115 based devices optimization while laying the ground for future work with the aim of better understating the interplay between bimolecular recombination and morphology arising from acceptor concentration.

7.2 Future Outlook

Looking forward research may continue along several possible paths. A first path would involve finishing calculations using the VOTCA software. VOTCA as a general methodology has shown promise and potential to provide unique insight, and its implementation for ZZ115 has been partial but achievable. This would allow a full characterisation of the different features found in the experimental section. Continuing the concentration variation study on additional fullerenes such as the ICXA series and even non-fullerene acceptors such as ITIC would provide more insight into the bimolecular recombination process and in particular how the choice of acceptor interacts with the ZZ115 polaron in crystalline region. Conversely, identifying a mixed amorphous phase when ZZ115 is combined with non-fullerene acceptors could provide additional insight on the kinetic independence with acceptor concentration. Going back to a more computational methodology, the study performed in Chapter **6** could be expanded to properly characterise the CT state of ZZ115, explaining its unusually high charge generation even in the pristine. Going beyond measurements and calcèulations based on this thesis, traditional material systems such as P3HT:$PC_{60}BM$ can still be relevant to this day and can still provide

insight into the bimolecular recombination process. OPVs remain potentially an invaluable asset for flexible energy production, with continuing research into improving its device functions.

Appendices

Table A-1: *Sample preparation conditions for ZZ115 pristine and ZZ115:$PC_{60}BM$ samples.*

Sample	ZZ115 amount	PC_xBM amount	Solvent amount	Spin coating conditions
Pristine	5.6mg	N/A	280µl	3500RPM, 30s
(1:2) $PC_{60}BM$	2.1mg	4.2mg $PC_{60}BM$	317 µl	800RPM, 30s
(1:2) $PC_{70}BM$	2.5mg	5.1mg $PC_{70}BM$	380µl	1500RPM, 40s

*Table **4.24**:*

Table A-2: *Sample preparation conditions for ZZ115 pristine, ZZ115:$PC_{60}BM$ and ZZ115:$PC_{70}BM$ samples.*

Sample	ZZ115 amount	PC_xBM amount	Solvent amount	Spin coating conditions
Pristine	5.6mg	N/A	280µl	3500RPM, 30s
(9:1) $PC_{60}BM$	9.0mg	1.0mg $PC_{60}BM$	500 µl	3000RPM, 30s
(4:1) $PC_{60}BM$	4.0mg	1.0mg $PC_{60}BM$	250 µl	2000RPM, 30s
(2:1) $PC_{60}BM$	5.4mg	2.7mg $PC_{60}BM$	407 µl	1000RPM, 30s
(1:1) $PC_{60}BM$	2.1mg	2.1mg $PC_{60}BM$	210 µl	800RPM, 30s
(1:2) $PC_{60}BM$	2.1mg	4.2mg $PC_{60}BM$	317 µl	800RPM, 30s
(1:4) $PC_{60}BM$	1.1mg	4.2mg $PC_{60}BM$	265 µl	800RPM, 30s
(9:1) $PC_{70}BM$	9.0mg	1.0mg $PC_{60}BM$	500 µl	3000RPM, 30s
(4:1) $PC_{70}BM$	4.0mg	1.0mg $PC_{60}BM$	250 µl	2000RPM, 30s
(2:1) $PC_{70}BM$	5.4mg	2.7mg $PC_{60}BM$	407 µl	1500RPM, 30s
(1:1) $PC_{70}BM$	2.1mg	2.1mg $PC_{60}BM$	210 µl	1000RPM, 30s
(1:2) $PC_{70}BM$	2.1mg	4.2mg $PC_{60}BM$	317 µl	800RPM, 30s
(1:4) $PC_{70}BM$	1.1mg	4.2mg $PC_{60}BM$	265 µl	800RPM, 30s

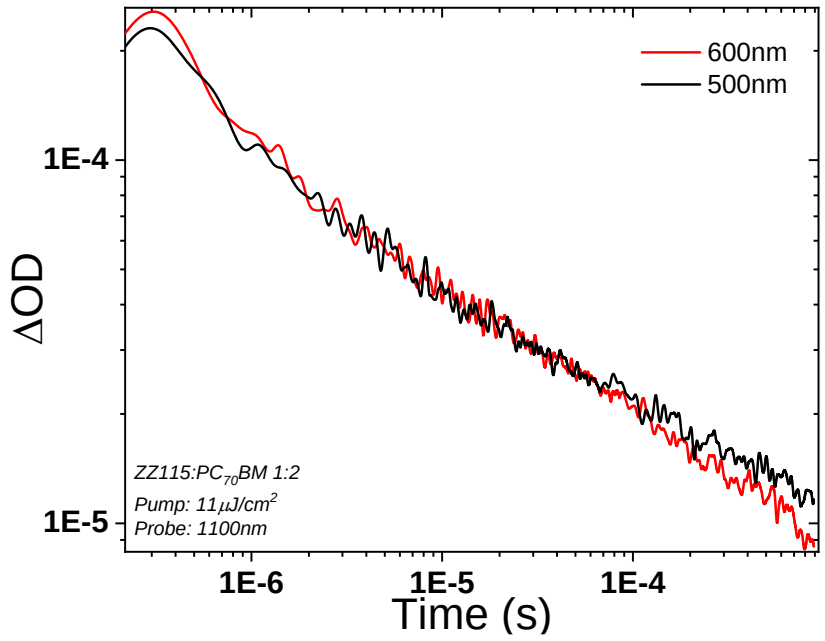

Figure A-1: *Transient absorption kinetics for ZZ115:PC$_{70}$BM at the (1:2) blend ratio at a 500nm excitation wavelength (black) and 600nm excitation wavelength (red). Kinetics were measured at 10uJ/cm^2 excitation density and at 1100nm probe wavelength.*

Potential variations caused by different excitation wavelengths were investigated via the transient kinetics at different excitation wavelengths. The typical kinetics measured at the 500 nm wavelength were compared to the extreme 600 nm wavelength, situated on the other side of the main 580 nm peak as seen in ***Figure 3-9:*** **a)** Normalised ground state absorbance spectra of ZZ115:PC70BM samples at the 1:2 blend ratio, pristine PC70BM and pristine ZZ115. The spectrum is normalised to the 580 nm peak. **b)** Photoluminescence spectrum of ZZ115:PC70BM at the 1:2 blend ratio and pristine ZZ115. The excitation wavelength used was 500 nm.. ***Figure A-1:*** *Transient absorption kinetics for ZZ115:PC70BM at the (1:2) blend ratio at a 500nm excitation wavelength (black) and 600nm excitation wavelength (red). Kinetics were measured at 10uJ/cm2 excitation density and at 1100nm probe wavelength.* shows very similar kinetics for both excitation wavelengths measured with no substantial change observed. As such results using the 500 nm excitation wavelength should be comparable to previous studies using a 532 nm excitation wavelength and more importantly ZZ115:PC$_{70}$BM measurements can be properly compared to previous measurements in this study even with a notable difference in absorbance. The 500 nm excitation wavelength was thus used for all measurements.